Model-Based Design and Development of an Offboard Actuation System for Lower-Limb Biomechatronic Devices

Anthony Anderson

A dissertation

submitted in partial fulfillment of the

requirements for the degree of

Master of Science

University of Washington

2018

Reading Committee:

Patrick Aubin, Chair

Katherine Steele

Santosh Devasia

Program Authorized to Offer Degree:

Mechanical Engineering

University of Washington

Abstract

Model-Based Design and Development of an Offboard Actuation System for Lower-Limb Biomechatronic Devices

Anthony Anderson

Chair of the Supervisory Committee:
Patrick Aubin, PhD.
Affiliate Assistant Professor
Mechanical Engineering

New robotic technologies allow for the rapid research and development of wearable assistive devices. Offboard robotic actuation systems use large, stationary actuators and versatile control systems to apply joint torques to assistive devices through flexible transmission tethers. This setup allows researchers to rapidly prototype assistive device behaviors and control laws without committing to a specific wearable device embodiment. The goal of this thesis was to develop an offboard robotic actuation system capable of actuating lower-limb wearable devices through Bowden cables. During the design process, a novel dynamic model of the biomechatronic system was developed. This model was used within an optimization framework to select optimal mechanical design parameters and servomotors. After design parameter optimization, a motor chassis and mechanical power transmission were designed and manufactured. A high-voltage

electrical circuit and electrical panel were designed and constructed to provide power to the servomotor amplifiers. A commercially available prosthetic foot was modified to be Bowden cable driven in the sagittal plane and was instrumented with sensors to detect joint rotation and Bowden cable force. A National Instruments PXI was purchased to read sensor signals, send motor commands, send data to a user interface in real-time, and log data.

TABLE OF CONTENTS

LIST OF FIGURES

LIST OF TABLES

ACKNOWLEDGEMENTS

This work was completed with support from the Veterans Affairs Center for Limb Loss and Mobility staff, resources, and funding.

Chapter 1. INTRODUCTION

1.1 BACKGROUND

1.1.1 *Transtibial Amputation and State-of-the-Art Prostheses*

People with transtibial amputations suffer from limited mobility and several secondary impairments related to gait. Examples of common comorbidities include an increased energetic cost of walking [1], higher incidences of knee osteoarthritis [2], and chronic lower back pain [3], [4]. Together, these impairments can lead to a lower quality of life. A 2008 study estimated that roughly 1.6 million amputees live in the United States, and predicted that the number will double to 3.6 million in 2050 [5].

Many of the issues experienced by transtibial amputees (TTAs) are biomechanical in nature. For example, lower limb amputees walk with an adapted gait strategy that heavily loads their intact limb [6] and are 17 times more likely to develop symptomatic knee OA in that limb than the general population [7]. TTAs also exhibit greater compressive forces in the spine and lateral bending towards their residual limb during gait [8]. Over 60% of TTAs report consistent lower back pain [3]. The fact that many of the ailments discussed here are associated with altered biomechanics suggests that higher functioning prosthetic devices could normalize gait patterns and lead to an increased quality of life.

Fortunately, prosthetic limbs have been steadily improving over the last few decades. The most basic prosthetic feet consist of a cushioned foam heel, a wooden forefoot, and cosmetic cover. These commercially available prostheses are known as solid-ankle-cushioned-heel (SACH) feet. More advanced prosthetic feet have specifically tuned material properties that allow the foot to store energy during stance and return it during push-off. These prostheses are constructed of carbon

fiber or fiberglass and are referred to as energy-storage-and-return (ESR) feet. SACH and ESR feet are the most commonly prescribed prosthetic feet today. Figure 1 shows both a SACH and ESR foot.

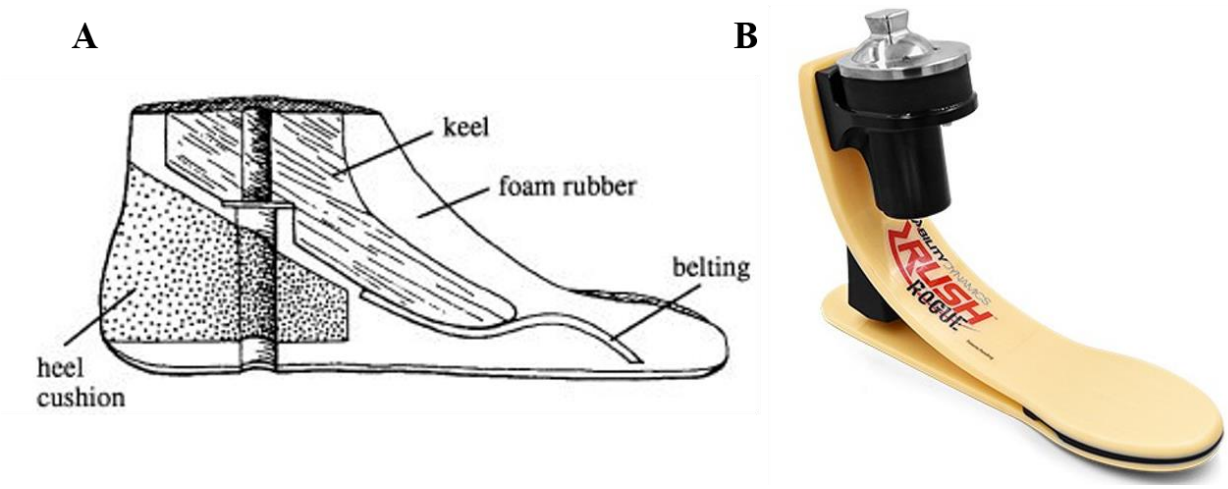

Figure 1: A) SACH foot (Digital Resource Foundation for the Orthotics & Prosthetics Community). B) ESR foot (Cascade Orthotics and Prosthetics).

Two new classes of prosthetic ankles have recently emerged in research and commercial settings due to increases in sensing, computing, and actuation technologies. Quasi-passive prostheses use microcontrollers to intelligently change their behavior (i.e. stiffness) with low-power actuators in response to sensor signals (Figure 2). These devices are considered quasi-passive because the actuators are not directly injecting energy into the gait cycle. Rather, they might engage a clutch [9], activate a hydraulic valve [10], or change a mechanical pivot position [11]. In contrast, active prostheses have actuators that replace the joint torques and power that would have been provided with the amputated musculature. While there are promising initial results [12] and one commercially available device [13], active prostheses are in their infancy.

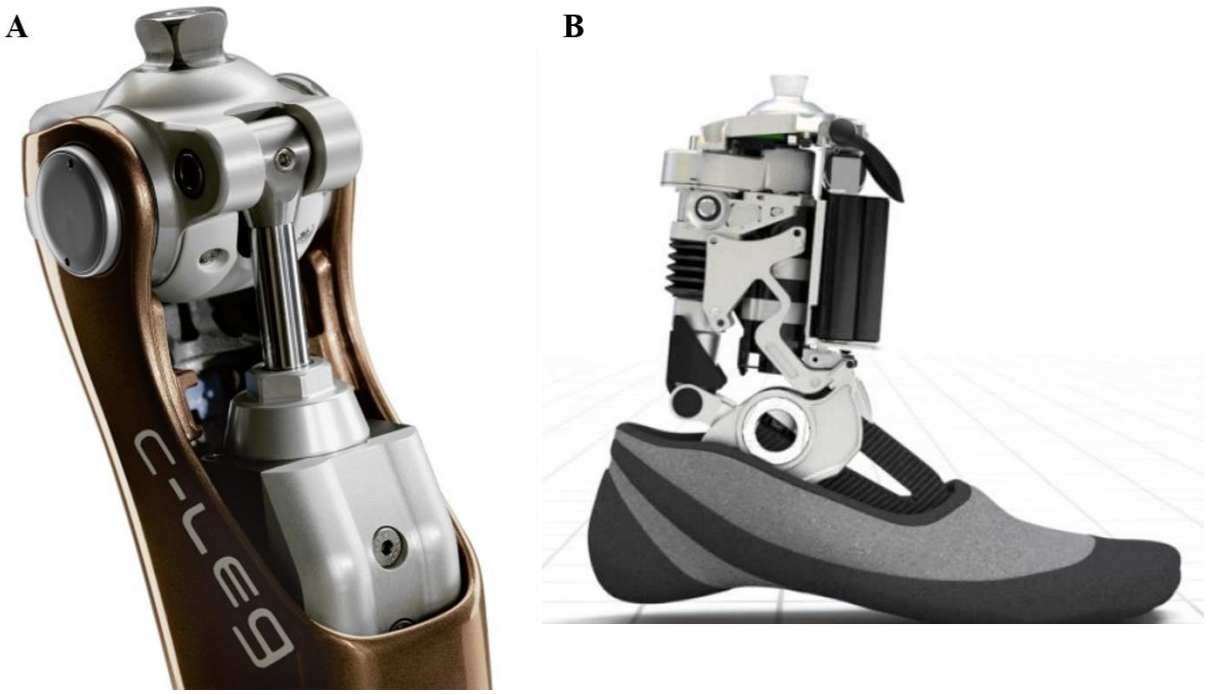

Figure 2: Two examples of modern prosthetic devices. A) The quasi-passive C-Leg from Ottobock changes the state of a hydraulic valve to change knee damping during gait. B) The Ottobock Empower is the only active prosthetic foot on the market. (Ottobock, Duderstadt, Germany)

Even with the major advances in prosthesis technology, the current state-of-care is deficient. The healthy human foot-ankle complex generates substantial power during terminal stance to accelerate the swing leg and whole-body center of mass [14]. SACH, ESR, and quasi-passive feet are passive structures that will always return less useful energy than they absorb due to hysteresis [15].

One relatively uninvestigated shortcoming of modern prostheses for below-knee amputees is the lack of knee assistance. In the healthy lower limb, the gastrocnemius muscle spans both the ankle and knee joints, contributing to knee flexion and ankle plantarflexion moments (Figure 3).

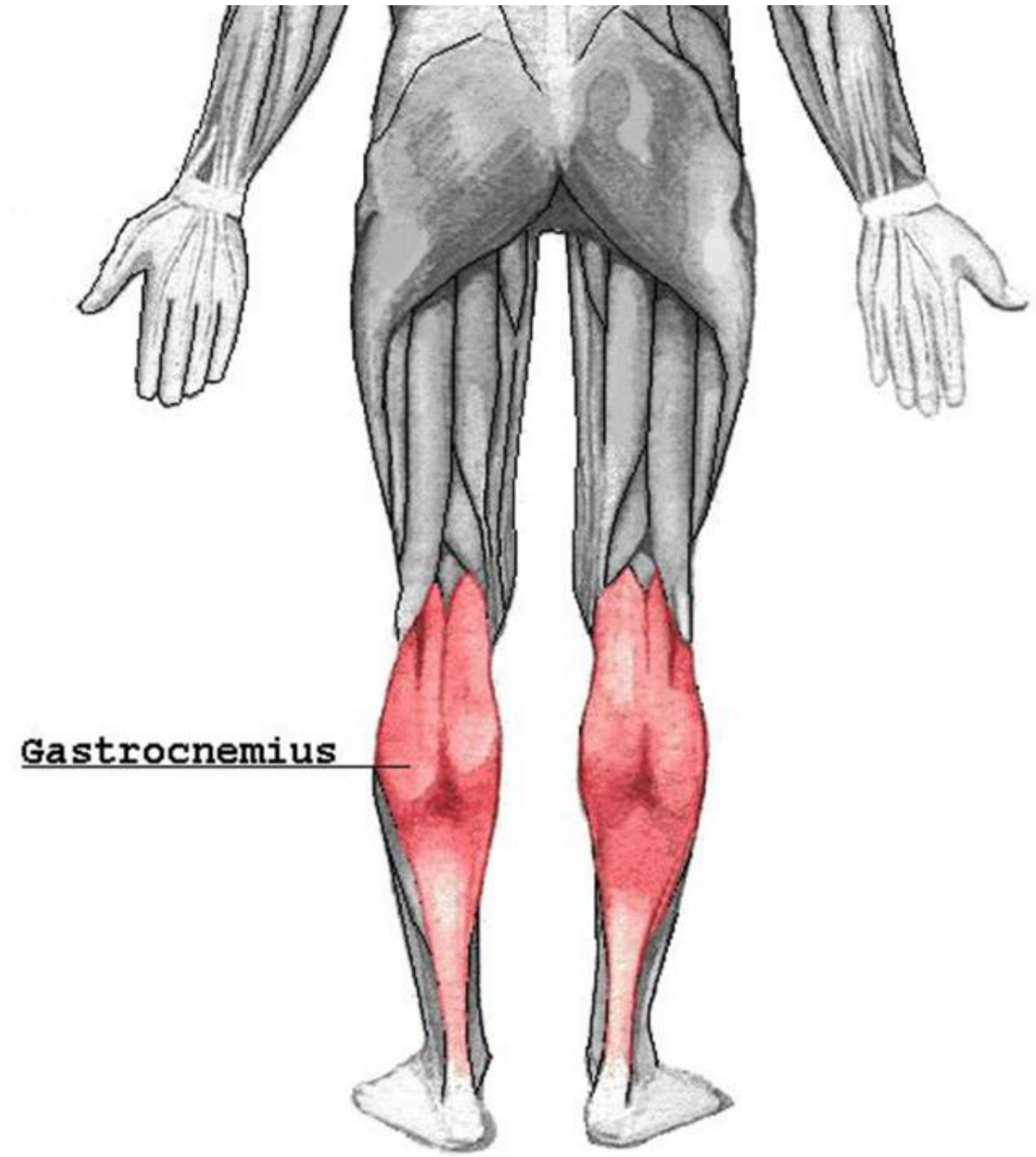

Figure 3: The biarticular gastrocnemius muscle originates above the knee and inserts below the ankle. (Gray's Anatomy, Creative Commons)

This musculotendinous pathway couples the dynamics of the two joints and is absent in TTAs. Muscles that span two joints are called 'biarticular' and are thought to contribute to the high energy efficiency of human gait [16]. Biarticular muscles allow energy transfer between proximal and

distal joints, and can result in unintuitive limb motions due to dynamic coupling [17]. One simulation study of human gait found that current ESR feet restored the trunk support provided by the monoarticular soleus muscle, but ESR feet do not restore the forward trunk and swing leg propulsion provided by the gastrocnemius [18]. Additionally, TTAs have deficient knee flexion during stance in comparison to healthy controls, even when using state-of-the-art robotic prostheses [19].

1.1.2 *Towards a Biarticular Prosthesis*

While biomechanists debate the functional role of the gastrocnemius during gait [17], [20], [21], we hypothesize that reintroducing and properly tuning this ankle-knee coupling will be beneficial to TTAs. Eilenberg et al. developed a biarticular knee-ankle prosthesis that consisted of a powered knee orthosis and robotic ankle prosthesis in 2018 [22]. While the device functioned as intended, it did not result in normative joint kinetics, kinematics, or decreases in metabolic costs when compared to the robotic ankle only. The authors attributed the lack of positive results to the human motor control system resisting the external device and the limited methods of the study. Interestingly, another group produced a biarticular knee-ankle exoskeleton for walking in healthy adults that showed greater reductions in metabolic cost with a biarticular configuration than a monoarticular configuration [23].

To address this lack of musculature in TTAs, our research group at the Center for Limb Loss and Mobility (CLIMB) developed and evaluated a prototype biarticular prosthesis (BP). The quasi-passive device consisted of a commercial ESR foot, a knee orthosis, and an electromechanical clutch-spring mechanism between the two joints (Figure 4).

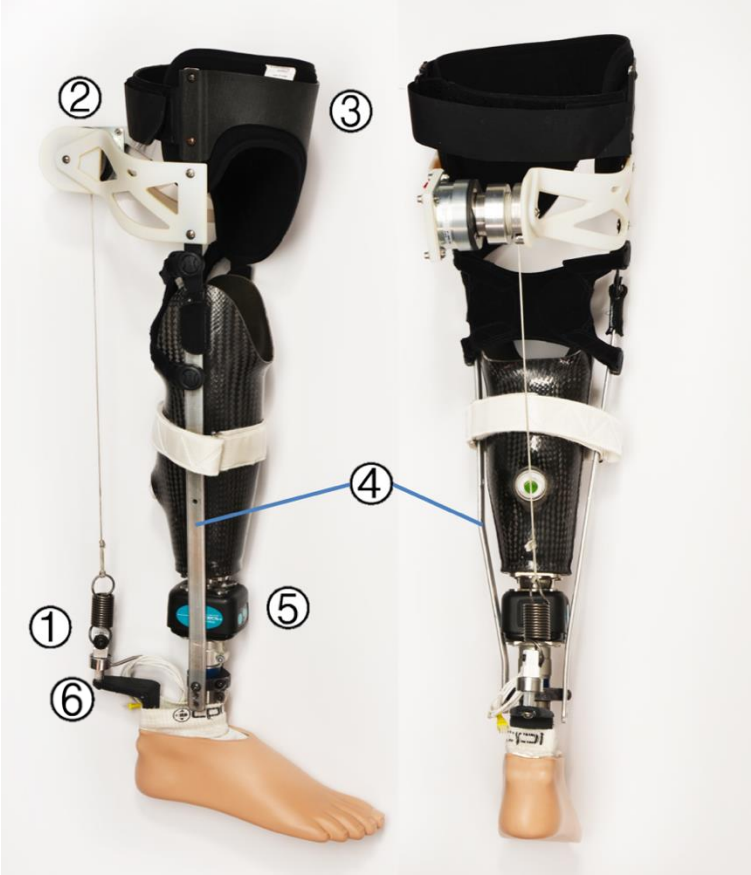

Figure 4: Version one of the CLIMB Biarticular Prosthesis. 1. Spring. 2. Clutch. 3. Thigh cuff. 4. Uprights. 5. Pylon load cell. 6 Spring load cell.

Spring force was measured with an in-line load cell, and a six degree of freedom load cell was mounted in line with the prosthetic pylon. The clutch timing was controlled by a microcontroller and inputs from the 6-DOF load cell. To vary the stiffness of the BP, three different extension springs were placed in-line with the biarticular coupling.

We conducted walking experiments with seven transtibial amputees and the BP at the CLIMB motion capture lab, recording ground reaction forces, electromyography, and motion capture. We found no significant differences between walking with our BP and walking with a standard monoarticular ESR foot for kinematic symmetry or total muscle force as computed with OpenSim

[24]. These results have been submitted for publication. One journal article has been accepted and two are under review [25]–[28].

We believe the primary failing of the BP was the device itself and its unintended effects on the users. The device was large, heavy, and uncomfortable. The subjects had to walk with a wider than normal stance, and the large moment arm at the prosthetic ankle may have affected their gait. Another failing was the limited range of behaviors the device could achieve. Only three spring stiffnesses were used in our experiments, and we do not know if our stiffness range included the optimal stiffness. Additionally, it was not possible to vary the knee-ankle moment arm ratio during data collection, another important design variable.

Even with the problems described above, the device required significant time, money, and engineering skill to develop. The prospect of spending even more effort to develop a second iteration of the device without knowing that our design changes would lead to functional improvements caused us to pause and look for an alternative design-build-test paradigm. We desired a more effective design and development strategy that would allow us to explore BP functionality without committing to a specific device embodiment.

1.1.3 *Offboard Robotic Actuation Systems*

Offboard robotic actuation systems that apply torques to human joints are becoming popular research tools for wearable devices, prostheses, human neuromuscular control, and human-machine interaction [29]–[32]. These devices generally use powerful actuators, wall power, and flexible transmission tethers to drive lightweight end-effectors worn by a user that walks on a nearby treadmill. In addition, body-worn sensors communicate with offboard real-time control hardware and experimenter friendly interfaces.

Moving actuation and computing resources offboard can accelerate the research of wearable robotic devices by providing many practical benefits. Large, powerful actuators can be used, as the subject bares only the mass of the sensors, end-effectors, and structural hardware (Figure 5).

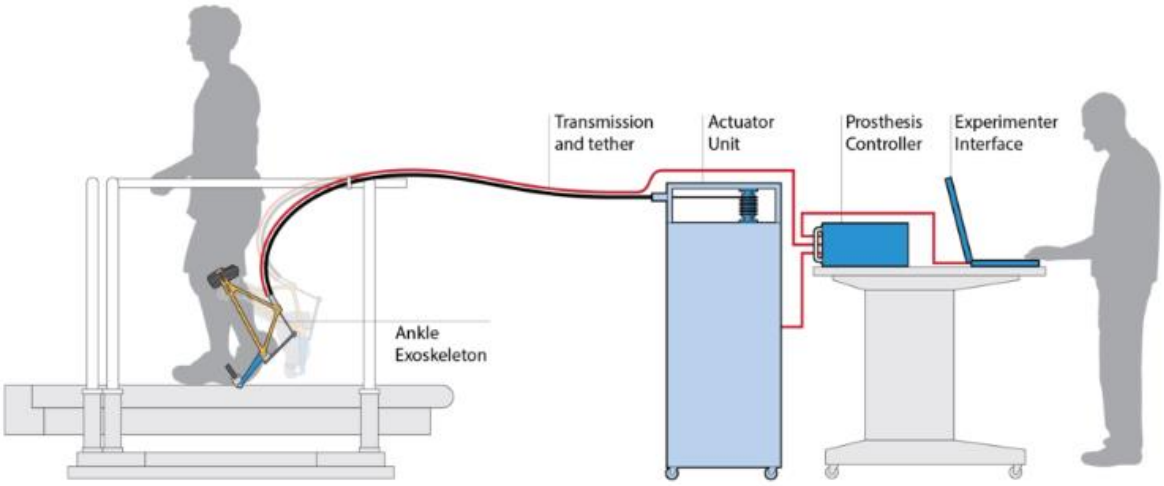

Figure 5: Schematic of offboard system architecture. (Humotech, Pittsburgh, PA, USA)

Control loop bandwidths are similarly improved with desktop real-time controllers. The presence of a flexible user interface also allows the experimenter to easily change device behavior during experiments [33]. Offboard systems also allow for faster iterations on the design, build, and evaluation process by removing the complexities associated with building a self-contained untethered wearable device. Rapid iterations that focus on how the device should behave and be controlled can occur through quick changes in software, rather than lengthy and slow hardware design changes and iterations.

The design and development of our biarticular prosthesis is the perfect use-case for an offboard robotic actuation system. With the ability to emulate many potential device behaviors, rigorous experiments could be carried out to find the optimal knee and ankle actuation that the BP should deliver to restore healthy gait patterns. A stand-alone wearable device could be developed

once optimal actuation profiles or parameters are found. The experiments would determine if the device should be passive, quasi-passive, or active, greatly reducing the unknown design parameters.

1.2 STATED AIMS

The primary goal of this thesis was to develop an offboard actuation system to be used as a research and development tool for wearable assistive devices in the CLIMB lab, including the biarticular prosthesis. As this is a nontrivial design problem, an auxiliary goal for this thesis was to first develop a model-based design and optimization paradigm with which we could use to explore the effects of various candidate actuators and mechanical design decisions for the offboard actuation system. Beyond our model-based design optimization, we needed to design and build the specific hardware to house our actuators and deliver power to a tethered wearable device. We needed to specify and obtain real-time control system hardware capable of controlling our actuators during experiments. Finally, we aimed to develop a prosthetic foot with integrated joint angle and actuator force sensors that could be Bowden cable driven in the sagittal plane. Throughout the remainder of this thesis, the offboard system to be designed and built will be referred to as the Controllable OffBoard Robotic Actuation (COBRA) system.

In summary, the aims of this thesis were:

1. Develop a modeling and optimization framework and use it to pick actuator and mechanical design parameters for COBRA.
2. Design and build the hardware necessary to deliver actuator power to a tethered wearable device.
3. Specify and purchase the necessary real-time control hardware and develop a tentative control paradigm for the offboard system.

4. Develop a prosthetic foot with integrated sensing that can be Bowden cable driven in the sagittal plane.

1.3 Design Specifications

Several technical requirements were established before the system was designed. First, it was decided that the system needed to be capable of providing the full sagittal plane knee or ankle moments during steady-state walking for a healthy 115 kg person. This body mass is slightly larger than the largest transtibial amputee that has participated in research studies within CLIMB. It is unlikely that this system will ever actually be used to provide the full joint moments during gait, as nearly all current state-of-the-art prostheses and exoskeletons rely on passive structures to provide at least some portion of the joint moment. Thus, this specification was conservative in that it set the required loading level above the expected typical use case of the system.

To study biarticular prosthesis actuation, it would be beneficial for the system to have two independent actuators. Requiring the system to have two degrees of freedom also provides additional flexibility for future studies involving bilateral AFOs, exoskeletons, etc. The largest electrical power available in the gait analysis laboratory at CLIMB is three-phase 208 VAC with a 30 Amp limit, so this was also considered as a design constraint.

In terms of sensing and control, the system was required to sense both the sagittal plane joint angles and moments applied to the end-effectors. With these measurements, the system could be operated in joint position, velocity, or torque control modes. To appropriately implement closed-loop control at a high enough bandwidth to assist human gait, dedicated real-time control hardware is a necessity. We also required the real-time system to be capable of communicating with a user interface on a desktop computer.

Finally, safety requirements were considered carefully. We required that the system have mechanical, electrical, and software safety features in the forms of physical hard stops for motion, emergency stop switches, and software limits on commanded joint and motor torques. We also required that once the system met all other design constraints, the backdrivability of the system would be optimized through mechanical design. Further discussion on backdrivability and safety can be found in Chapter 3.

1.4 THESIS ORGANIZATION

Chapter Two of this thesis details the system architecture and human-machine modeling. In Chapter Three, we use the model, a library of candidate motors, and an optimization framework to select a motor and choose mechanical design parameters. Chapter Four discusses the sensors, instrumentation, and control paradigm we developed for the system. Hardware design is discussed in detail in Chapter Five for a motor chassis, a high-voltage electrical box, and the Bowden cable driven prosthetic foot.

Chapter 2. SYSTEM ARCHITECTURE AND MODELING

2.1 SYSTEM ARCHITECTURE

With the design specifications determined, a number of actuation methods were investigated. Hydraulic, pneumatic, and servomotor actuators are all viable design choices for offboard actuation systems for gait assistance. While pneumatic muscles (e.g. McKibben Actuators) are a popular choice for tethered locomotion experiments, they have complex and nonlinear input-output behavior that depends on air pressure, length, and tension. This adds complexity to the control system and can result in torque tracking errors. Hydraulic actuators are fast and powerful but require the design of a fluid system, can leak hydraulic fluid, and have very stiff hoses when pressurized.

Ultimately, we decided on electrical servomotors for actuators, with flexible Bowden cable transmission tethers, as can be seen in Figure 5. Servomotors have high power density, simple input-output dynamics, and are relatively easy to control. Bowden cable friction is known to be nonlinear and difficult to model, but some robotic systems overcome this by treating it as a disturbance in the control scheme [34], [35].

The COBRA system requires a desktop computer for the experimental interface and data logging, a real-time control system to receive sensor signals and send motor commands, two servo drives to deliver wall power to the motor, two servomotors, wearable end effectors, and joint-side sensors (Figure 6).

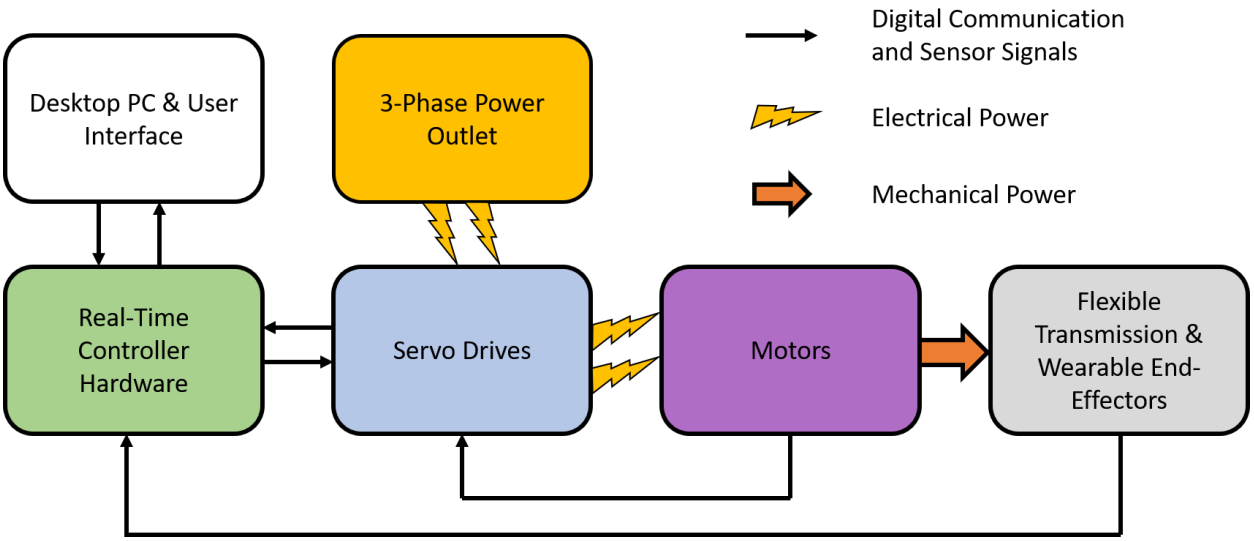

Figure 6: System architecture schematic

This high-level system design explains the overall signal and power flow, but the specifics of the electromechanical design and control paradigm are left abstract. The methodology and rationale behind motor selection, end-effector design, and other design decisions are detailed in the following chapters.

2.2 Wearable Devices

Early in the design process, we decided that rather than designing wearable devices from the ground up, we would modify commercially available devices to be Bowden cable driven. This was intended to accelerate our research developments, as custom prosthetic foot and knee orthosis designs are beyond the scope of this thesis.

2.2.1 *Ankle Joint Hardware*

For the prosthetic foot, we chose to work with the Venture Foot (Figure 7), a popular foot designed and manufactured by College Park Industries (Warren, MI, USA). One engineering benefit of this

foot is that it has a pin joint, unlike many of the commercially available feet. This allows for simple instrumentation with a joint encoder and modifications for powered plantar and dorsiflexion.

The sagittal plane torsional stiffness about the pin joint of this foot can be tuned by selecting appropriate rubber bumpers that sit in front of and behind the pin joint. These rubber bumpers allow for a nonlinear stiffness profile that mimics the human ankle quasi-stiffness. The bumpers can be removed to allow the joint to move freely. Additionally, the pin joint is supported by rubber bushings that allow for limited rotations in the frontal and transverse planes. A composite leaf spring is attached to the bottom of the foot, and also contributes to the overall stiffness between the shank and foot segments. Figure 7 shows an exploded view of the prosthetic foot.

Figure 7: Exploded view of the College Park Venture Foot. 1. Top ‘ankle bone.’ 2. Bottom ‘ankle bone.’ 3. Bumpers. 4. Axial pin. 5. Ankle Bushings. 6. Axial Pin Screw. (College Park Industries, Warren, MI, USA)

Details on the local sensing of the foot can be found in Chapter 4, and the mechanical design of the Bowden cable attachment modifications are in Chapter 5.

2.2.2 *Knee Joint Hardware*

A PreStride knee-ankle-foot-orthosis (Becker Orthopedic, Troy, Michigan, USA) was purchased for use as the wearable device for the knee joint. We purchased a knee-ankle-foot-orthosis (KAFO) rather than a knee orthosis for flexibility in future experiments, in the event that we would want to actuate the knee and ankle for a healthy person. When used with an amputee, the ankle joint will be removed from the device, and the vertical struts will be attached directly to the prosthetic pylon.

The KAFO also has a single pin joint at the knee. Polycentric knee joints that accommodate the translation of the knee center of rotation are more common in orthosis designs but are more difficult to instrument with sensors. The PreStride (Figure 8) also has multiple torsion springs across the joints, and a small pneumatic shock absorber across the knee joint, but all of these components were removed upon purchasing the device. Permanent hardware for Bowden cable actuation has not yet been developed for the orthosis.

Figure 8: The Becker PreStride KAFO. Note the lightweight vertical struts, Velcro straps, and passive torque development hardware. The torsion springs, cables, and pneumatic shock absorber were removed to make the pin joints mechanically transparent. (Becker Orthopedic, Troy, MI, USA)

2.3 HUMAN-MACHINE MODELING

The design and development of offboard human-robotic systems can benefit from modeling and simulation [36], but not much work has been published on modeling the human nor the physical human-robot interface interactions within these systems. Model-based design allows for robot optimization, improved tools, and ultimately more experimental capabilities.

Modeling human gait can be a complex and computationally expensive task if the model accounts for limb inertias and time-varying muscle and ground reaction forces. However, if it is assumed that end-effector torques will take the place of the torques produced by muscles without changing the known joint kinematics, a greatly simplified model can provide useful insights. In this framework, end-effector torque and position can be considered independently, as the load is not purely inertial. Recent publications have used this approach for optimal motor and transmission sizing in robotic applications [37], [38].

We developed a mathematical model of the system that includes sagittal plane joint dynamics, end-effector mechanical design parameters, human-device interface stiffness, transmission stiffness and friction, and electromechanical motor properties. Actuator dynamics and mechanical design parameters were modeled from first-principles, while the human-device interface stiffness, Bowden cable, and biological joint trajectories were modeled from empirical data. This model allowed us to explore various motor choices, mechanical design configurations, and other design variables.

The modeling paradigm presented here has the following inputs:

1. desired applied joint moment with respect to time [$\tau_{wearable}$, (Nm)]
2. joint angle trajectories with respect to time [$\theta_{wearable}$, (rad)]
3. joint-side end-effector pulley radius [$r_{wearable}$, (m)]
4. motor side cable sheave radius [r_{sheave}, (m)]
5. Bowden cable linear stiffness [k_{cable}, (N/m)]
6. Bowden cable friction term [γ_{cable}, (unitless)]
7. servomotor rotor inertia [I_{motor}, (kg-m^2)].

The desired joint trajectories are then propagated back through the lever arm, Bowden cable, sheave, and motor rotor inertia models to compute the model outputs:

1. motor torque [τ_{motor}, (Nm)]
2. motor angular velocity [ω_{motor}, (rad/s)]

These are the motor trajectories necessary to accomplish the desired input joint dynamics with the given input parameters. Figure 9, below, shows a simplified model that relates these terms at the prosthetic ankle joint. A similar figure for the knee would also show an additional nonlinear torsion spring in series with the knee joint, to represent the human-device interface stiffness. This model was implemented in a custom MATLAB script, which is included in Appendix A.

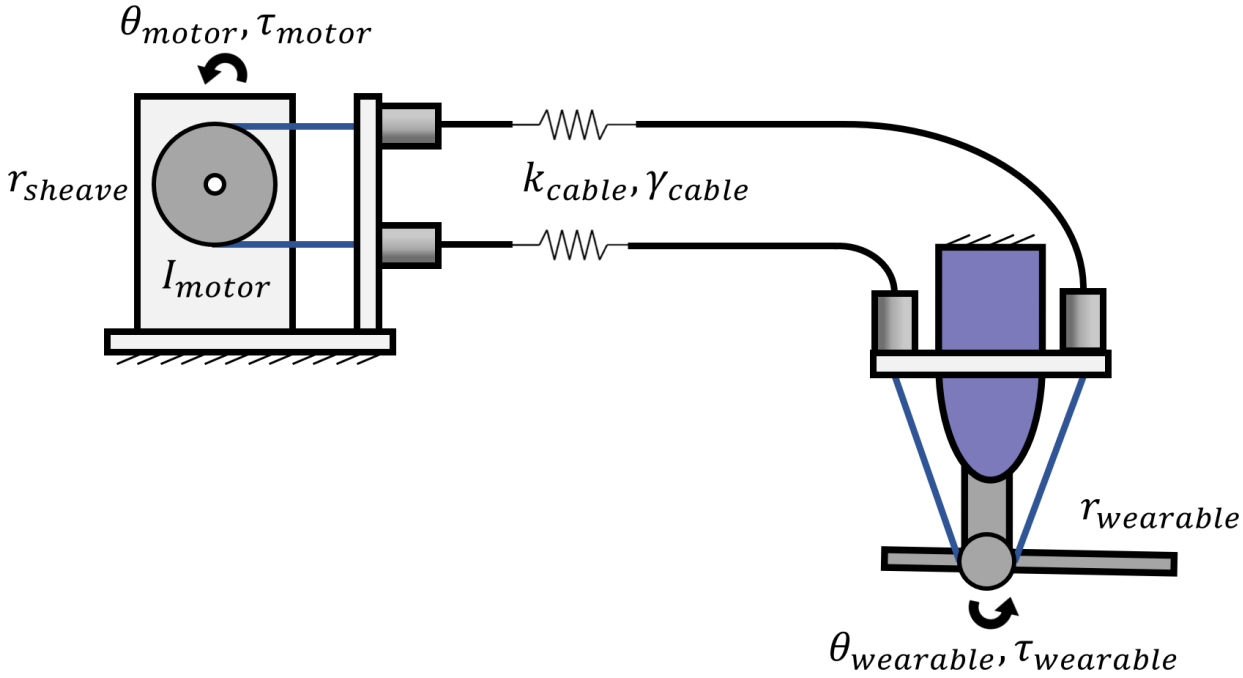

Figure 9: Simple model diagram for the prosthetic foot.

2.3.1 *Biomechanical Input Trajectories*

The desired joint trajectories for this model were mean sagittal plane ankle and knee moments and angles from 11 healthy adults (age 23.4 ± 3.9, mass 93.0 ± 10.6 kg) during one stride of steady

state walking (Figure 10). These curves were digitized from published data [19], and low-pass filtered with a 4th order zero-lag Butterworth filter with a cutoff frequency of 12 Hz to minimize any digitization errors. The joint moments were scaled to a 115 kg person, as to size the system for the largest individual expected to walk with the system. All trajectories were scaled to have a duration of 1.2 seconds, a moderate steady state walking cadence [39]. A sign convention was selected that labeled joint angles and moments as positive if they tended towards limb flexion. I.e., ankle dorsiflexion and knee flexion angles and moments were considered positive.

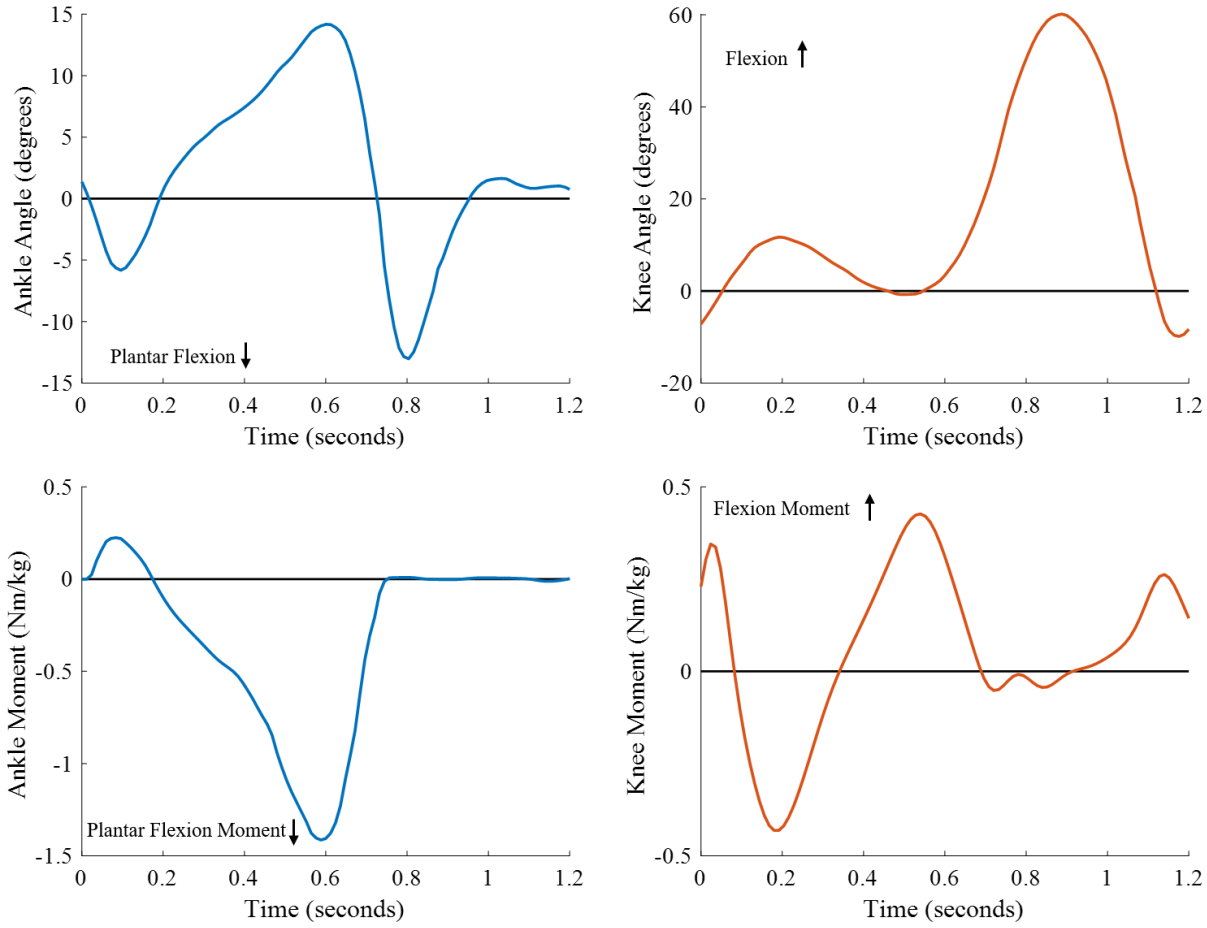

Figure 10: Joint dynamics used in all simulations. The left column shows ankle joint angles and normalized moments, and the right column shows knee joint angles and normalized moments.

It was assumed that the system would provide 100% of either the ankle or knee torque that would usually be provided by the subject's muscles in both flexion and extension. When simulating the system, only one joint is considered at a time. As the knee and ankle are considered independent in these simulations, changes in one motor trajectory will not affect the other.

2.3.2 *Human-Device Interface Stiffness Model*

Human lower limb soft tissue compresses significantly under normal load [40]. Depending on the design of the wearable components, there can also be significant compliance in the end-effector itself [41]. Recent work has shown that the human-device interface stiffness can significantly reduce the power delivered from the device to the user [42]. Compliance at the human-device interface is therefore an important aspect to model and shouldn't be neglected. As the prosthetic foot will be all mechanical componentry, we did not include a stiffness model at the ankle. The following describes how we included soft-tissue dynamics at the knee into our model-based design optimization.

Sagittal plane rotation of the knee orthosis joint can be decomposed into motion from joint rotation and motion from soft tissue compression:

$$\Delta\theta_{orthosis} = \Delta\theta_{tissue}(\tau_{orthosis}) + \Delta\theta_{knee} \quad \text{(eq. 1)}$$

In this description, $\Delta\theta_{orthosis}$ is the change in angular position of the orthosis joint, $\Delta\theta_{knee}$ is the change in angular position of the knee joint, and $\Delta\theta_{tissue}$ is the additional orthosis rotation due to compression of the soft tissue surrounding the femur and tibia while under load. $\tau_{orthosis}$ is the torque applied to the knee joint by the orthosis. In many exoskeletal and orthosis designs there is an underlying assumption that $\theta_{orthosis} = \theta_{knee}$, here we explicitly allow for the orthosis angle

to differ from the knee angle due to soft tissue compliance by introducing $\theta_{tissue}(\tau_{orthosis})$. Figure 11 shows a schematic of the knee, orthosis, and soft tissue elements.

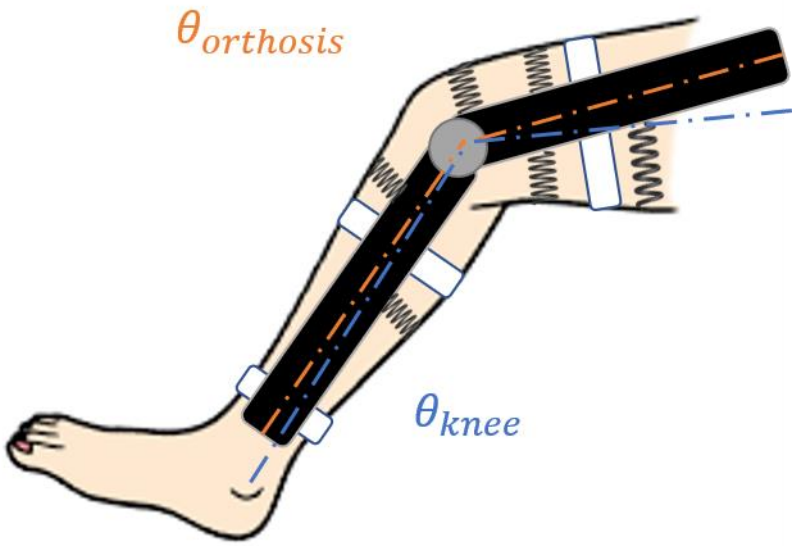

Figure 11: Definition of orthosis and knee joint angles.

This figure illustrates that changes in the orthosis angle will track changes in the knee angle, unless an external torque is applied to the orthosis, in which case the soft tissue will compress. In other words, if the knee angle was held fixed the orthosis could still rotate due to soft tissue compression.

As the notation in (eq. 1) indicates, the rotation of the orthosis joint due to soft tissue compression is a function of the torque applied to the joint by the orthosis. This tissue compliance torque-angle relationship was quantified experimentally for one subject (Male, 190.5 cm, 95 kg) in an IRB approved data collection at the Center for Limb Loss and MoBility within the VA Puget Sound Health Care System.

For this experiment, the previously mentioned Becker KAFO was modified so that the knee joint could be loaded in either flexion or extension with a Bowden cable (Figure 12). After informed consent, the KAFO was fit to the subject by a licensed prosthetist-orthotist. Reflective

markers were fixed to the subject's greater trochanter, lateral epicondyle of the femur, tibial tuberosity, and lateral malleolus. Markers were also fixed to the brace thigh and shank sections, at the brace's center of rotation for the knee joint, and at the Bowden cable termination points.

During the experiment, hanging weights were slowly applied to the actuator end of the Bowden cable while a motion capture system (Vicon, Oxford, UK) recorded the reflective marker locations. A load cell (Omega Engineering, Bridgeport, NJ, USA) in-line with the inner cable recorded the applied cable force. During loading, the subject was instructed to stand in a slight lunge, with his knee joint at approximately 40° of flexion. The subject was also instructed to resist the applied torque by not allowing the exoskeleton to move his knee. Multiple loading trials were recorded for both flexion and extension loading, with weights up to 444.8 N in extension and 400.3 N in flexion. Figure 12 shows the experimental setup. In the figure, the red arrows indicate cable force, and the blue arrow indicates the Bowden cable reaction force on the brace.

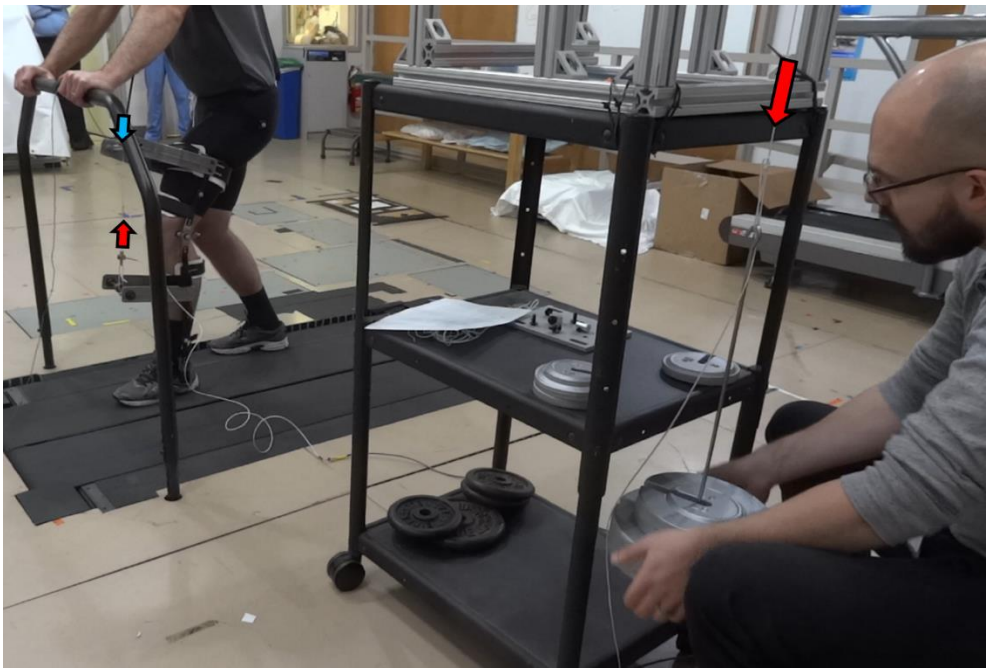

Figure 12: Experimental setup to determine soft tissue stiffness curve for knee extension.

All force and motion data were analyzed in MATLAB (MathWorks, Natick, MA, USA). A KAFO coordinate system was defined using the reflective marker locations, and the orthosis knee joint angle and subject's knee joint angle were computed in this coordinate system. While the subject was instructed not to move his joint, there was still significant sagittal plane motion during loading. As the orthosis angle is a summation of rotation due to bone motion and rotation due to soft tissue compression, the bone motion was subtracted from the exoskeleton motion.

$$\Delta\theta_{tissue} = \Delta\theta_{knee} - \Delta\theta_{orthosis} \quad \text{(eq. 2)}$$

This assumes that changes in $\theta_{orthosis}$ that are not present in θ_{knee} are due to soft tissue compression. The reflective markers fixed to the Bowden cable termination points and orthosis knee joint rotation center were used to define the orientation of the force vector and moment arm length. The applied joint torque was computed as the cross product of the moment arm and the force signal from the load cell. The Δ in (eq. 2) is intended to note that the relationship was computed from relative changes in angles, not the absolute angles themselves.

Figure 13 shows the vectors that were defined in MATLAB. The two teal vectors defined the knee joint, while the yellow vectors defined the orthosis joint. The Bowden cable line of action (red) was defined and used to calculate the moment arm to the orthosis joint center (dashed green).

Figure 13: Definitions for vectors used in stiffness calculations. Shank vector was shifted anteriorly in this image for clarity.

Data from each trial was averaged (within conditions) and the torque-angle relationship of the human-device interface was computed (Figure 14). Separate second order polynomials were fit to the flexion and extension data (flexion $R^2 = 0.9871$, extension $R^2 = 0.9832$), with the physically motivated constraint that the curves passed through the origin. To include the knee joint interface stiffness in our model, these curves were substituted into (eq. 1).

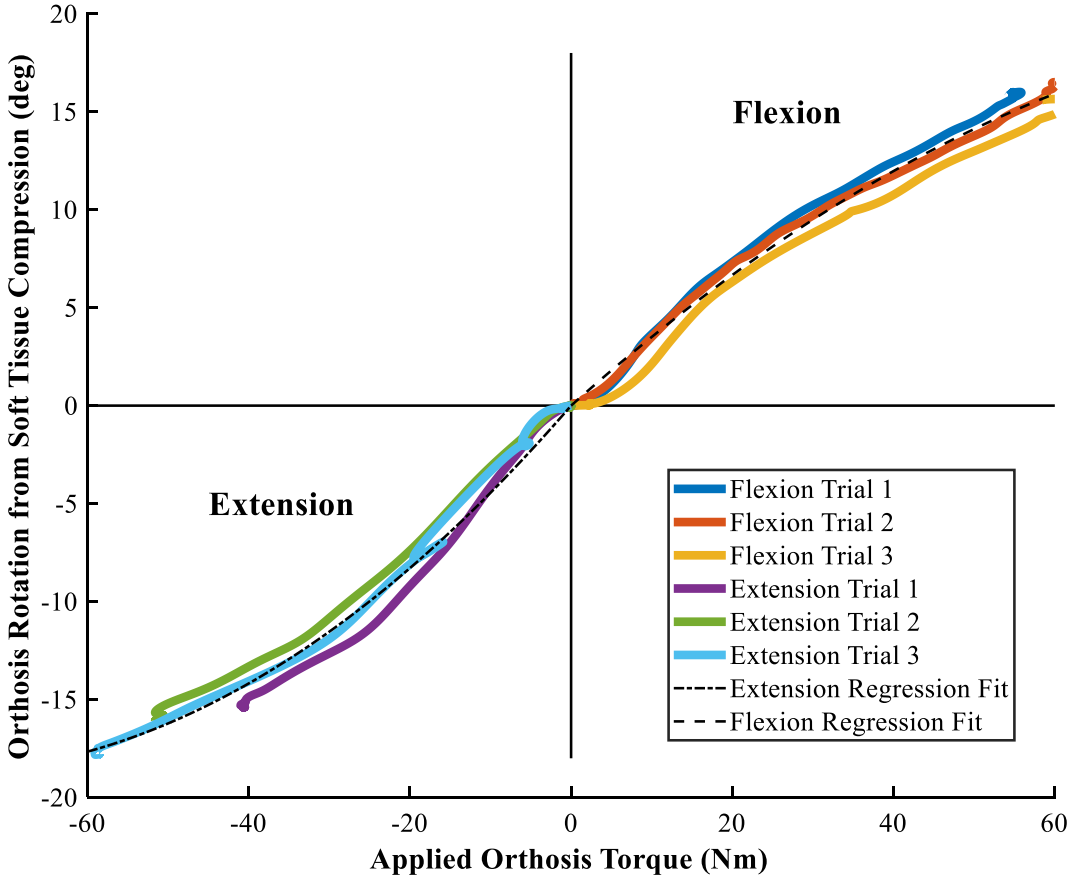

Figure 14: Results from human-device interface stiffness experiments.

2.3.3 *Bowden Cable Model*

The inner cable of the Bowden cable is modeled as Dyneema, an ultra-high strength polyethylene rope. This rope was selected due to its high strength, low friction, and low bending stiffness. The axial stiffness value for this model was 822 kN/m, as computed from the specification sheet for a 2-meter-long, 6.35 mm diameter Dyneema rope (West Marine, Watsonville, CA, USA).

Bowden cable friction is highly nonlinear and difficult to model. We modeled this friction with a simple cable tension efficiency. A recent paper showed Bowden cable tension efficiencies ranging from 0.581 to 0.906 [43], so we used a conservative efficiency of 0.5. This was

implemented in the model with a constant multiplier of 2 on the required cable force. Cable force at the actuator was computed as:

$$F_{cable} = \gamma_{cable} \frac{\tau_{wearale}}{r_{wearable}} \quad \text{(eq. 3)}$$

In eq. 3, F_{cable} is the force developed on the inner cable of the Bowden cable, γ_{cable} is the friction multiplier, and $r_{wearable}$ is the effective lever arm of the wearable device joint. This lever arm may vary with the angle of the device, but here we model it as constant throughout the range of motion, as to remain agnostic to the specific mechanical design.

The linear motion of the cable was computed, accounting for both the rotation of the joint and the stretch in the Dyneema rope.

$$x_{cable} = \theta_{wearable} r_{wearable} + \frac{F_{cable}}{k_{cable}} \quad \text{(eq. 4)}$$

2.3.4 *Motor Model*

Our motor rotation angle was modeled as:

$$\theta_{motor} = \frac{x_{cable}}{r_{sheave}} \quad \text{(eq. 5)}$$

Here, r_{sheave} is the radius of the sheave attached to the motor output. The corresponding motor angular velocity, ω_{motor}, and acceleration, α_{motor}, were computed numerically with 4th order central difference differentiation schemes.

The motor torque required to achieve the desired trajectory included both the torque required to accelerate the rotor inertia, I_{motor}, and the torque required to achieve the cable force.

$$\tau_{motor} = \alpha_{motor} I_{motor} + F_{cable} r_{sheave} \quad \text{(eq. 6)}$$

Viscous friction from the motor is not included here as it is difficult to estimate without physical hardware and is likely to be negligible in comparison to the friction in the Bowden cable.

Chapter 3. OPTIMIZATION AND MODEL-BASED DESIGN

With a dynamic model of COBRA, simulation and design optimization are possible. To optimize the design, we needed an optimization framework with which to select motors, gearing, sheave radius, and lever arms for Bowden cable termination points on the wearable devices.

3.1 COST FUNCTION

Many different cost functions can be formulated for an offboard system. Examples might include cost functions that minimize actuator power, actuator inertia, lever arm lengths, etc. We decided to optimize this system with respect to reflected impedance at the biological and prosthetic joints when the system was turned off, while also requiring that the motor selected could perform the required torque-velocity trajectory.

Low output impedance on an offboard robot is important for user comfort and safety and is a function of the stiffness, damping, and inertia from the robot reflected through the transmission. In the case of a power loss or fault, an assistive wearable device with low impedance at the biological joint would allow the user to continue to walk easily. Additionally, if the system is turned off, the device will behave as transparently as possible and will not impart large passive torques to the joints.

In our model, the friction of the offboard system is assumed constant and is not affected by motor selection or design parameter choices. Therefore, the minimization of the output impedance at the wearable device joint is reduced to minimizing the reflected inertia from the motor. Mathematically, our optimization objective was stated as:

$$\min_{r} \left(\frac{r_{wearable}}{r_{sheave}}\right)^2 I_m \qquad \text{(eq. 7)}$$

In this equation, r is a parameter vector containing $r_{wearable}$, the effective lever arm at the joint, r_{sheave}, the sheave radius, and I_m, the motor inertia. When optimizing the ankle joint, $r_{wearable}$ is set to $r_{prosthesis}$, and when optimizing the knee joint $r_{wearable}$ is set to $r_{orthosis}$.

Note that this is a mixed discrete-continuous optimization problem. The mechanical design variables are continuous, but motor inertias are discrete values defined by the construction of commercially available motors.

3.2 CONSTRAINTS

This optimization problem was also subject to several practical constraints related to the power available to the motor and drive, physical limitations on design parameters, and the torque-speed relationship of the motor. All constraints listed here are enforced over one gait cycle. If the constraints are met over one gait cycle, they will be satisfied continuously during gait, assuming a steady-state walking speed.

3.2.1 *Motor Back-EMF Constraint*

This constraint ensures that the electrical current required by the motor to carry out the desired trajectory is always less than the current available to the motor at the required speed and must be enforced along every point in the trajectory. This constraint is derived from a simple DC motor model, similar to [37], and neglects motor inductance. As an electric motor increases in speed, a back-EMF voltage is generated in opposition to the voltage bus within the drive. This limits the current the drive is able to push through the motor, increasing linearly with motor speed. Mathematically stated:

$$\frac{\tau_{motor}}{K_{motor}} \leq \frac{V - K_{motor}|\omega_{motor}|}{R} \quad \text{(eq. 8)}$$

Here, K_{motor} is the torque constant for the motor, V is the voltage supplied to the servo drive, R is the motor terminal resistance, and ω_{motor} is motor velocity. For the simulations discussed here, V was set to 264 Volts, as this is the DC rail voltage available from a standard 3-Phase 208 VAC outlet, accounting for 10% losses due to capacitor ripple.

3.2.2 *Motor Speed Constraint*

This constraint enforces the motor speed throughout the trajectory to be less than or equal to the maximum motor speed as listed by the manufacturer's specification sheet.

$$\omega_{motor} \leq \omega_{motor,max} \quad \text{(eq. 9)}$$

Maximum motor speeds are primarily limited by centrifugal forces on the rotor and bearing temperature rise.

3.2.3 *Wall Current Constraint*

The third constraint limits the electrical current available to the motor to be less than the electrical current available at the wall socket in our research laboratory at the Center for Limb Loss and Mobility in Seattle, WA. This current was determined during the construction of the laboratory space.

$$\frac{\tau_{motor}}{K_{motor}} < 30 \text{ Amps} \quad \text{(eq. 10)}$$

It is also necessary to enforce this constraint over the entire duration of the trajectory.

3.2.4 *Thermal Constraint*

This constraint states that the root-mean-square of the current trajectory must be less than the continuous operating current, i_{cont}, as specified by the motor specification sheet.

$$rms\left(\frac{\tau_{motor}}{K_{motor}}\right) \leq i_{cont} \quad \text{(eq. 11)}$$

While imposing this constraint is a common way to prevent the motor from overheating during the trajectory, meeting the constraint does not guarantee that the motor and drives will operate at safe temperatures. When the system is operating, temperatures need to be monitored carefully to prevent equipment damage. If necessary, active cooling will be implemented.

3.2.5 *Wearable Device Lever Arm Constraints*

Constraints were also imposed on the mechanical design parameters of the wearable device attachment points. Specifically, we required the effective lever arm radii of the orthosis to be between 2.3 and 15 centimeters, and the prosthesis joint to be between 7.4 and 15 centimeters.

$$0.023 \leq r_{orthosis} \leq 0.15 \text{ meters} \quad \text{(eq. 12)}$$

$$0.074 \leq r_{prosthesis} \leq 0.15 \text{ meters} \quad \text{(eq. 13)}$$

To pick the lower bounds, we first picked an inner rope for the Bowden cable (see Chapter 5) that had a breaking strength of 4,400 N. We desired a safety factor of two on the rope's breaking strength, so we then computed the smallest moment arm that would result in a 2,200 N cable force for both the peak moments for the ankle and knee joints. I.e., smaller moment arms would result in cable forces exceeding 2,200 N at the peak moment. The upper bounds were somewhat arbitrary but allowed for compact and more practical mechanical design configurations.

3.2.6 *Motor Sheave Constraint*

Lastly, the radii of the sheaves were constrained to be positive:

$$0 \text{ meters} < r_{sheaves} \quad \text{(eq. 14)}$$

An upper limit could have been specified as well, but initial experiments showed that the optimization algorithm never picked excessively large sheave radii.

3.3 Cost Function and Constraint Evaluation

To evaluate the cost function, a motor with a known inertia must be selected. Values for r_{sheave}, and $r_{wearable}$ must be chosen, and the cost function can be computed easily. However, the cost function does not ensure that the motor is able to carry out the required dynamic trajectory.

To evaluate the constraints, the system must be simulated with the motor and design parameters. The constraints from equations 8-10 must be enforced at every point along the simulated motor trajectory. If all of the constraints cannot be met under any combination of design variables for a given motor, it is an indication that the motor is not capable of carrying out the trajectory.

3.4 Optimization Algorithm

To approach the stated minimization problem, we imported a library of 157 servomotors (Kollmorgen, Radford, VA, USA) into MATLAB. This library is representative of the state-of-the-art in servomotors with peak stall torques ranging from 0.61 Nm to 1073 Nm. The library contained a list of motor names and their respective inertias, terminal resistances, torque constants, maximum speeds, continuous operating currents, etc. Both standard servomotors and cartridge servomotors are included in the library. Further discussion on the differences between standard and cartridge motors can be found in Chapter 5. In Figure 15, each point is a unique motor, showing the relationship between motor inertia, peak motor torque, and peak motor speed.

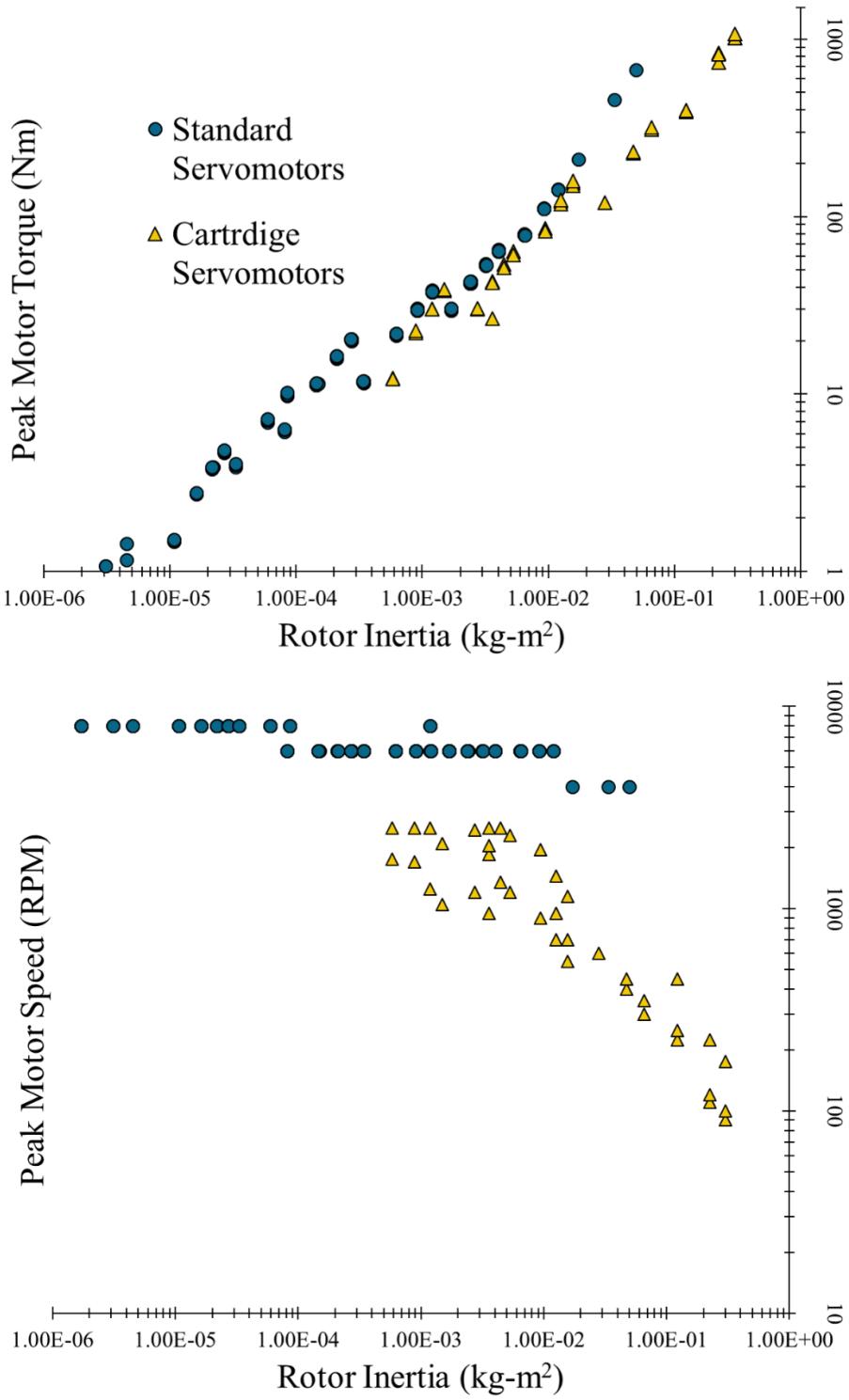

Figure 15: Candidate motor catalog plots. Top) Log-log relationship between rotor inertia and peak motor torque. Bottom) Log-log relationship between rotor inertia and peak motor speed.

An independent constrained optimization was performed over each individual motor using MATLAB's built-in constrained minimization routine with an interior-point algorithm. If a sheave radius or wearable device lever arm was selected by the optimization algorithm, an additional gearbox could be added to the motor output that would make sheave manufacturing possible and result in the same overall reflected inertia.

If a given motor could not meet the constraints, it was discarded and removed from consideration. Motors that met the constraints were added to a list of feasible design configurations along with their optimized parameters and corresponding reflected inertia values. Motors on the list were then sorted by ascending reflected inertia. The configuration with the lowest reflected inertia was deemed optimal.

3.5 Optimization Results

3.5.1 *Ankle*

120 out of 157 motors were able to satisfy the constraints for the ankle trajectories. The parameter configuration with the lowest reflected inertia had a 10.5 cm (4.1 inch) lever arm at the ankle joint, a 24.9 cm (9.76 inch) sheave radius, and used the Kollmorgen C133A – one of the largest servomotors available in the library. This moment arm gearing configuration results in an effective gear ratio of ~1:2.4, i.e. the torque at the motor is ~2.4x higher than the torque at the prosthesis joint. The smallest motor capable of completing the trajectory was the AKM24F and required a gear ratio of ~105:1. The optimal configuration is 5.5x more backdriveable than the configuration with the smallest motor that can complete the trajectories. Table 1 shows the top five outputs from the optimization algorithm, with an added column for the motor weight.

Table 1: Top five ankle motors and mechanical design parameters as selected by the optimization algorithm.

Rank	Model	Inertia ($kg\ m^2$)	$r_{prosthesis}$ (m)	r_{sheave} (m)	Reflected Inertia ($kg\ m^2$)	Motor Weight (kg)
1	C133A	0.302	0.106	0.249	0.055	132
2	C132A	0.225	0.111	0.216	0.060	101
3	C133C	0.302	0.120	0.243	0.073	132
4	C063C	0.0157	0.074	0.034	0.074	29
5	C062C	0.0126	0.074	0.027	0.097	23.6

3.5.2 *Knee*

84 out of 157 motors were able to satisfy the constraints. The optimizer chose the Kollmorgen C132A, a motor one size smaller than the optimal ankle motor. It selected an 8.0 cm (3.1 inch) lever arm at the knee joint, and a 15.2 cm (6.0 inch) sheave radius. In this configuration, the knee motor is also operating at a higher torque and lower speed than the orthosis joint. Table 2 shows the top five motor and mechanical design configurations selected by the optimization algorithm. Notice that the algorithm selected the same top five motors, but the top two motors are switched, and the knee orthosis lever arm and motor sheave are smaller than the ankle prosthesis values.

Table 2: Top five motors and mechanical design configurations for the knee joint.

Rank	Model	Inertia ($kg\ m^2$)	$r_{orthosis}$ (m)	r_{sheave} (m)	Reflected Inertia ($kg\ m^2$)	Motor Weight (kg)
1	C132A	0.225	0.080	0.152	0.062	132
2	C133B	0.302	0.071	0.150	0.067	101
3	C133C	0.302	0.023	0.046	0.071	132
4	C063C	0.0157	0.023	0.011	0.072	29
5	C062C	0.0126	0.023	0.008	0.097	23.6

For reference, 114 motors were able to satisfy the constraints when the soft tissue model was not included. This means that there were 30 motors that were no longer feasible choices due to the effects of the soft tissue. As a spring acts as a low-pass filter in a mechanical system, the motors needed to operate at higher speeds to complete the desired joint trajectories.

Initially, we were surprised to see that more motors could complete the ankle trajectory than knee trajectory. Further analysis of the ankle and knee kinematics showed that the two joints do very similar amounts of total mechanical work over the gait cycle [44]. The ankle has a higher peak power, but the knee does slightly more total work in the trajectories that we are using as model inputs.

3.5.3 *Discussion and System Selection*

In both the knee and ankle system optimizations, a configuration was selected that acted as a torque reduction between the motor and the joint. This is the opposite relationship built into many gearbox designs: usually a servomotor operates at a lower torque and higher speed than the load. The reversed gearing arrangement selected by our algorithm agrees with our intuition regarding our cost function, as this setup 'hides' some of the motor inertia from the joints by putting a large lever arm at the motor.

While 30 motors were deemed unfeasible due to soft-tissue dynamics, the number is likely higher. Our model only considered the stiffness of the human-device interface and did not consider the hysteresis or damping that would be present. A more elaborate experimental setup would be necessary to quantify these effects.

In terms of practical considerations, the motors selected by the algorithm are immensely large. For example, the C133A weighs 132 kg (292 pounds) and would require a small crane to install. Additionally, the hardware to support the motor during operation would be heavy and expensive.

Due to these concerns, we decided to re-consult the list of optimal motors and lever arm configurations for a more compact option. The 4th motor on both optimally sorted lists was the Kollmorgen C063C. The reflected inertia was 36% higher than the optimal ankle configuration and 15% higher than the optimal knee configuration, but the motor weighed only 29 kg (63 pounds), resulting in a 77% reduction in motor weight.

Due to the increased convenience in a smaller motor mass, we chose to purchase two of the C063C servomotors, and design our motor sheaves and wearable device moment arms to the values indicated in Tables 1 and 2. The specific mechanical design for the motor sheaves and prosthesis hardware can be found in Chapter 5.

Chapter 4. CONTROL, SENSING, AND INSTRUMENTATION

The electromechanical design characteristics of lower-limb assistive devices have mostly converged. Carbon fiber leaf springs, pin joints, aluminum pylons, and ball screws paired with brushless servomotors define the primary components of research grade prosthetic ankles and exoskeletons. The same cannot be said for the control of these devices. Lower-limb active and quasi-passive prosthetic device control is an active area of research, and an excellent review of the state-of-the-art can be found in [45]. This chapter details our control paradigm and the physical hardware we're using to implement it.

4.1 CONTROL HARDWARE

4.1.1 *Kollmorgen AKD P02406 Servo Drive*

A servo drive was purchased from the motor manufacturer. The AKD P02406 servo drive's primary purpose is to modulate the delivery of wall power to the servomotor in such a way that it tracks a reference command from an external controller. The drive operates on three phase power, at voltages between 85 and 265 Volts. The peak output current is 48 Amps, and continuous output power is 8000 Watts. Figure 16 shows one of the drives.

Figure 16: AKD P02406 digital servo drive. Connections on the front panel are for communication, high voltage cables, and other IO functionality. (Kollmorgen, Radford, VA, USA)

The drive has multiple onboard PID loops to track position, velocity, and current. These loops are nested, i.e. the output of the position loop is the input to the velocity loop, and the output of the velocity loop is the input to the current loop (Figure 17).

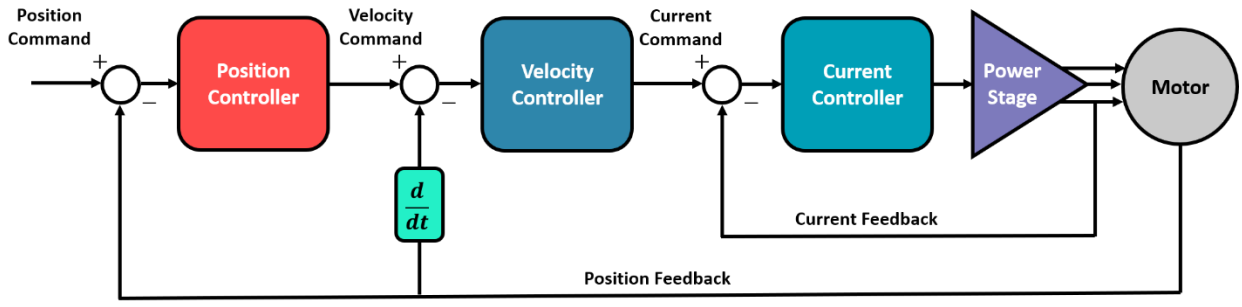

Figure 17: Cascaded PID loop structure within Kollmorgen AKD drives.

The position loop bandwidth is 1-250 Hz, the velocity loop bandwidth is 0-600 Hz, and the current bandwidth is 2-3 kHz. Reference signals can be received by the drive via analog inputs or digital communication via etherCAT, an Ethernet-based fieldbus system. The servo drive requires an electrical circuit and enclosure to operate, the design of which is detailed in Chapter 5.

4.1.2 *National Instruments PXIe-8880*

The primary controller for the offboard system is a National Instruments PXIe-8880 and NI PXIe-1085 chassis (full system referred to as PXI). The PXI is a modular electronic instrumentation platform with a 2.3 GHz eight-core controller and a LabVIEW real-time operating system (Figure 18).

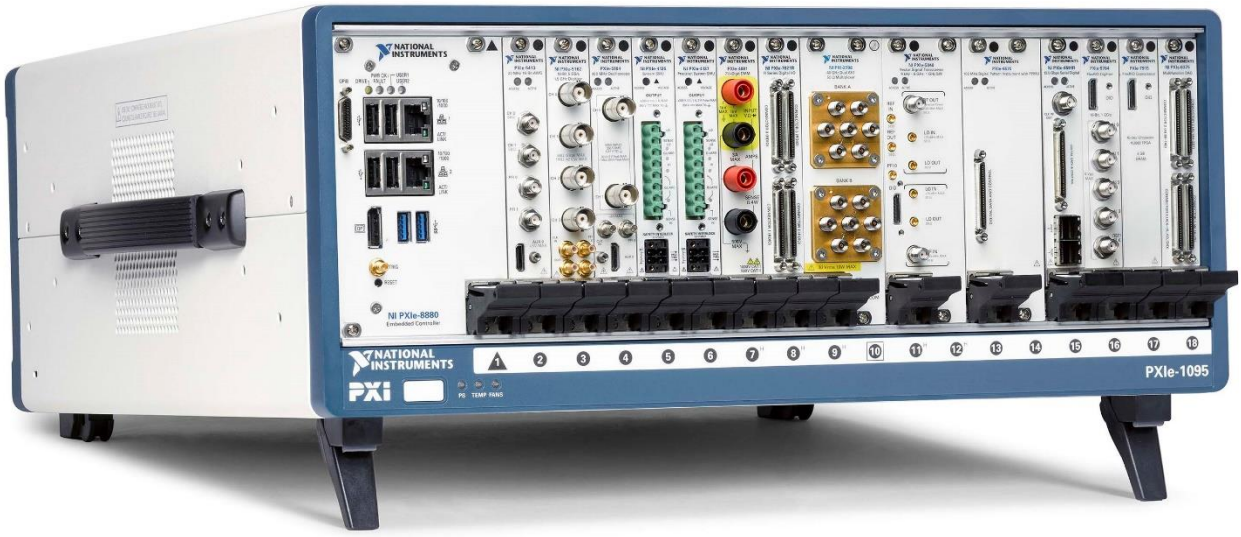

Figure 18: Example of PXIe-8880 controller, chassis, and modular electronics. (National Instruments, Austin, TX, USA)

The chassis has 16 slots for plug-and-play input or output modules. We are using several modules to read analog inputs. The PXI can communicate with any PC running LabVIEW and LabVIEW Real-Time. For COBRA, the PXI will communicate with a PC over a local area network, and with

the AKD P02406 servo drive via etherCAT. One other important function of the PXI is to send data to the desktop PC to display and log experimental data in real time.

4.2 CONTROL PARADIGM

As this device is intended to be a general research tool, we desire the offboard system to be as accommodating as possible to various control law structures. There are a variety of approaches for sagittal plane assistive device control, but two broad classes of control paradigms are:

1. control strategies that assign joint torques in response to sensor signals, and
2. controls strategies that assign joint positions/velocities in response to sensor signals.

These two strategies encompass the state-of-the-art for prosthesis control, including impedance/admittance controllers, feed-forward EMG controllers, echo controllers, etc.

Each strategy can be further sub-divided into high-level trajectory generation and low-level setpoint tracking via closed loop control. The role of the high-level trajectory generator is to determine the appropriate prosthesis behavior in response to sensor measurements, and the role of the low-level controller is to appropriately command the actuators to follow the setpoint and reject external disturbances. For Type 1 control strategies, the high-level controller will output torque commands, and for Type 2 control strategies the high-level controller will output joint motion commands. Specific trajectory generation strategies are beyond the scope of this thesis, and they will necessarily be problem and wearable device specific.

Low-level tracking will be achieved via coordination of the PXI, servo drive, and wearable sensors. In order for the system to operate in joint torque or position mode, it must be able to ‘close the loop’ around either joint torque or position. As joint torque will vary depending on device geometry, we decided to sense cable force. Cable force will be sensed at the joint rather than at the motor so that the effects of Bowden cable friction can be treated as an unknown disturbance.

Known device geometry and stiffness properties will be used to relate the cable force measurement to joint torque. Rotary encoders will be used to sense joint angle. More information on sensor selection can be found in section 4.3.

Figure 19 shows the signal flow for the proposed control system operating in joint torque mode. The project-specific trajectory generator within the PXI will command a target cable force, F_{cable}^{cmd}, which will be compared to the measured cable force, F_{cable}^{meas}, at the wearable device. A PID algorithm within the PXI operating on the cable force error will output a commanded motor velocity signal to the drive. With this configuration, if the cable force error is zero, the motor will not move.

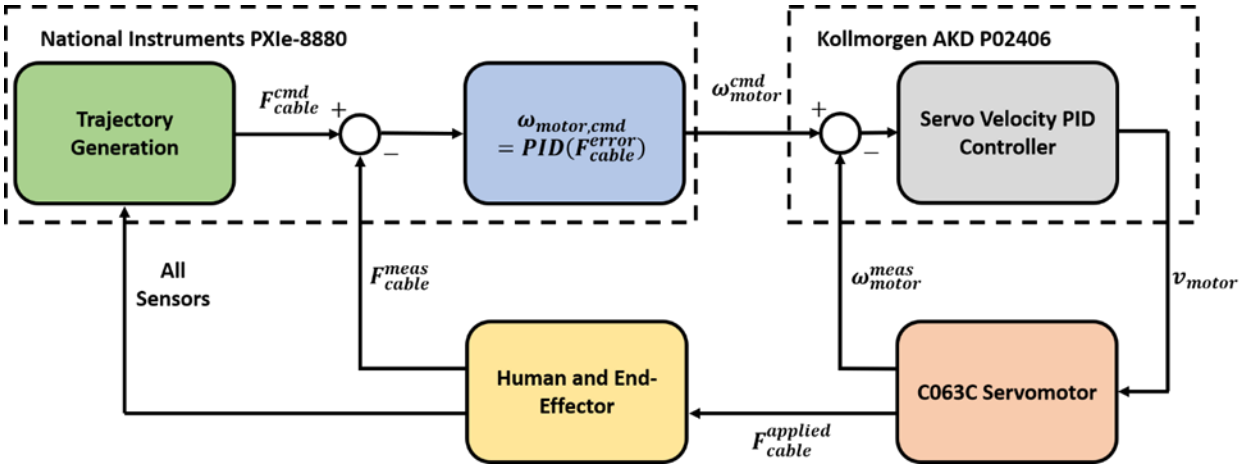

Figure 19: Signal flow diagram for the offboard system control architecture.

Given measurements from a rotary encoder in the motor, the servo drive will compare the commanded motor velocity, ω_{motor}^{cmd}, with the measured motor velocity, ω_{motor}^{meas}, and modulate the motor voltage appropriately to achieve low tracking errors. The motor rotation actuates the Bowden cables, and in turn, the wearable device. A variation of this approach has been shown to be successful in [46].

4.3 SENSING

The following sections detail the sensors selected for the wearable hardware. To see how these sensors were integrated into the prosthetic foot, see section 5.3.2.

4.3.1 *Motor Current and Rotation*

The C063C servomotors and AKDP02406 servo drives have multiple sensing capabilities. Motor current is sensed within the drive and can be used to estimate motor torque using the known motor torque constant. The C063C is equipped with a high-accuracy single-turn absolute sine encoder. This is an analog sensor, but when paired with the AD converter within the drive has the equivalent of 134,217,728 counts per motor revolution. Both of these sensors are used within the drive's cascaded PID algorithms.

4.3.2 *Cable Force*

We are sensing cable force at the interface of the prosthetic foot and Bowden cable using an LTH300 thru hole load cell (Futek, Irvine, CA, USA). This sensor allows the inner rope of the Bowden cable to pass through the center of the load cell and measures the reaction force between the Bowden cable housing and the prosthetic foot (Figure 20). This reaction force measurement is an acceptable proxy measurement for cable force.

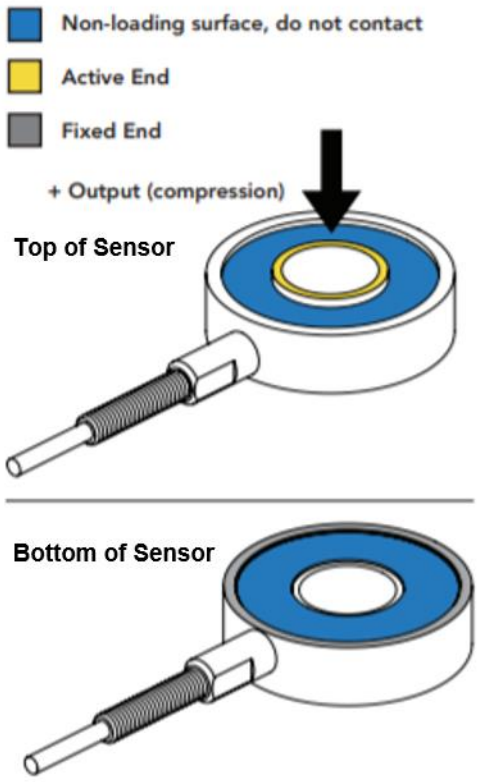

Figure 20: Futek thru hole load cell schematic. The inner rope of the Bowden cable passes through the center hole, and the outer cable rests on the surface shown in yellow. (Futek, Irvine, CA, USA)

We are using two sensors at the foot, one to sense cable force associated with plantarflexion, and one to sense cable force associated with dorsiflexion. Two sensors will also be required for the knee.

These compact sensors are rated for up to 2224 N (500 pounds) and weigh approximately 57 grams (0.13 pounds) each. Sensor excitation is 10V, and the output is measured via a strain bridge module in the PXI. Each sensor was calibrated with hanging weights over the operational range. Additional sensor information can be found in Appendix B.

4.3.3 *Joint Rotation and Foot-Ground Contact*

The sagittal plane rotation of the prosthesis is measured with an RM08 miniature non-contact magnetic encoder (Renishaw, New Mills, Gloucestershire, UK). These lightweight sensors are specifically built for space-constrained applications, are less than 1 cm in diameter, and weighs under 2 grams (0.004 pounds). The sensors are analog sine encoders with an accuracy of ±0.3˚. Each sensor has a sealed microchip component, and a magnetic 'actuator' component. The chip portion of the sensor measures the relative rotation of the magnetic actuator (Figure 21).

Figure 21: Renishaw encoder image. The magnetic 'actuator' is shown hovering over the enclosed chip portion of the sensor (Renishaw, New Mills, Gloucestershire, UK).

Foot-ground contact will be sensed with a standard foot switch. The foot switch is simply several force sensitive resistors embedded within a thin rubber sheath (Figure 22). The foot switch is inserted between the prosthesis and the shoe and can be used as an on-off switch indicating whether or not the foot is in contact with the ground.

Figure 22. Example of a standard biomechanical foot switch. (Noraxon U.S.A., Inc., Scottsdale, AZ, USA)

Chapter 5. HARDWARE DESIGN AND MANUFACTURING

This chapter details the component selection, mechanical design, and manufacturing of all hardware for the offboard system. All solid models and drawings were created with OnShape (Cambridge, MA, USA), a cloud-based CAD modeling software. Custom metal components were manufactured by Sound Machine Products (Kent, WA, USA) and FATHOM (Seattle, WA, USA).

5.1 Motor Chassis and Power Train

5.1.1 *Discussion of Cartridge Motors*

Standard servomotors have a rotor that is supported by two bearings mounted to the front and back of the stator (Figure 23). These motors are mounted to a frame, and their shafts are connected to the load with a coupling mechanism. The C063C motor that our optimization algorithm selected is a cartridge direct-drive motor. Cartridge motors do not have bearings inside of the motor, and there is no mechanical contact between the rotor and stator. Instead of using a flexible shaft coupling, the shaft and bearings are part of the load, and the rotor mounts onto the shaft with a compression coupling. The stator mounts to the frame, and the bearings in the load maintain the air-gap between the rotor and stator.

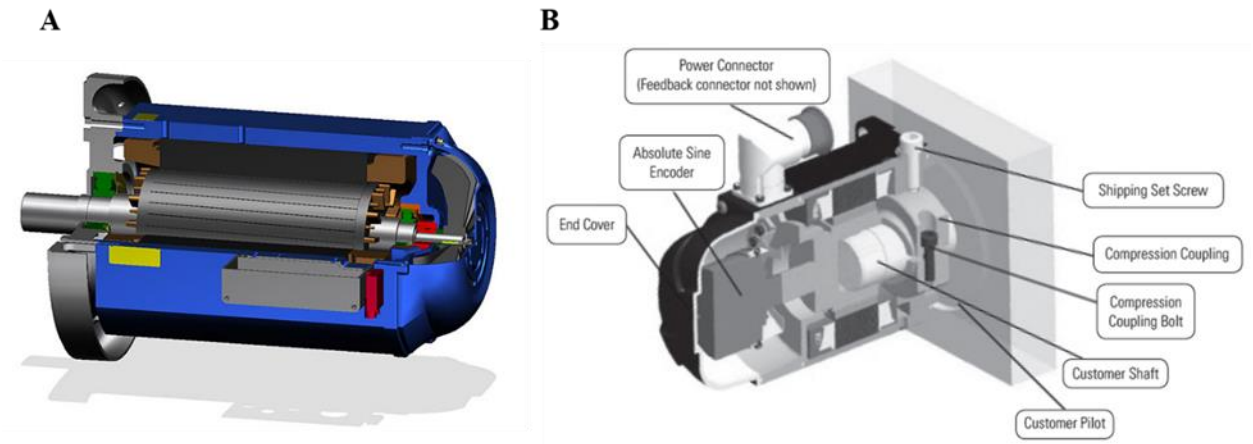

Figure 23: A) Cross section of a standard servomotor. The stator is blue, the rotor is grey, and the bearings are green. (Servax Drives, Zurich, Switzerland) B) Cartridge motor. The stator is black, and the rotor is light grey. The stator attaches to the 'customer shaft' via a compression coupling within the motor. The bearings for this setup are embedded within the mounting plate. (Kollmorgen, Radford, VA, USA)

Cartridge motors have advantages and disadvantages. The motors can achieve a higher power to inertia ratio than standard servomotors, and additional shaft coupling hardware is not required. In terms of disadvantages, the mechanical design and bearing selection are critical, as the assembly must be rigid enough to maintain the air gap between the rotor and stator in the presence of high load.

Our high-level design for the power train consisted of a motor mount plate with bearings and drive shafts. One side of the plate would be the motor mount interface, and the other side of the plate would support the sheaves. This required the design of a mounting plate for the motor, a bearing-supported drive shaft for each motor, custom sheaves for the inner cable of the Bowden cable to wrap around, and a Bowden cable termination plate.

5.1.2 *Drive Shaft and Mounting Plate Design*

Both motors were mounted to a single horizontal plate, with the motors mounting to the bottom, the shaft running through the plate, and extending through the top of the plate for sheave mounting. The motor manufacturer supplies critical dimensions for the portion of the shaft that slides into the motor, a pilot hole for the motor on the mounting surface, and the configuration for the mounting holes (Figure 24). This figure, and all other pertinent drawings and schematics can be found in Appendix B.

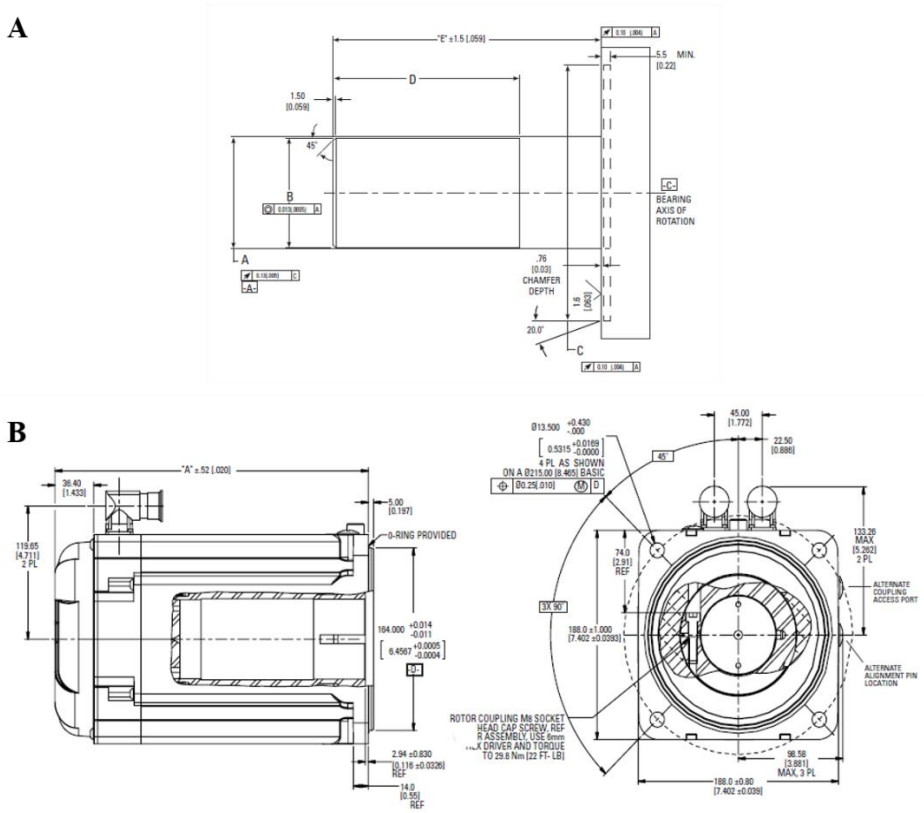

Figure 24: A) Mounting specifications for the shaft and mounting plate provided by Kollmorgen for the C063C. The right side of the plate is not shown, as it is application specific. B) Motor dimensions used for designing motor mount plate and chassis.

With these dimensions, we first designed a stepped shaft (Figure 25). The largest two diameters were set by the motor interface requirements. The middle portion of the shaft was sized

by consulting a bearing catalog to find a standard size bearing close to the first diameter. At first, we selected a standard rotary ball bearing, but initial tests showed that the bearings were too compliant in the radial direction to maintain the required air gap between the motor's rotor and stator. To remedy this, we selected a tapered roller bearing (Timken, North Canton, OH, USA) with the same inner and outer diameter as the initial bearing. Tapered roller bearings are much stiffer and are well suited to resist moment loads on the shaft. A final step in the shaft was made to provide a mounting surface to which our pulleys could be attached. The top of the shaft was threaded in order to provide preload to the tapered roller bearings. Two shafts were made from Aluminum 6061.

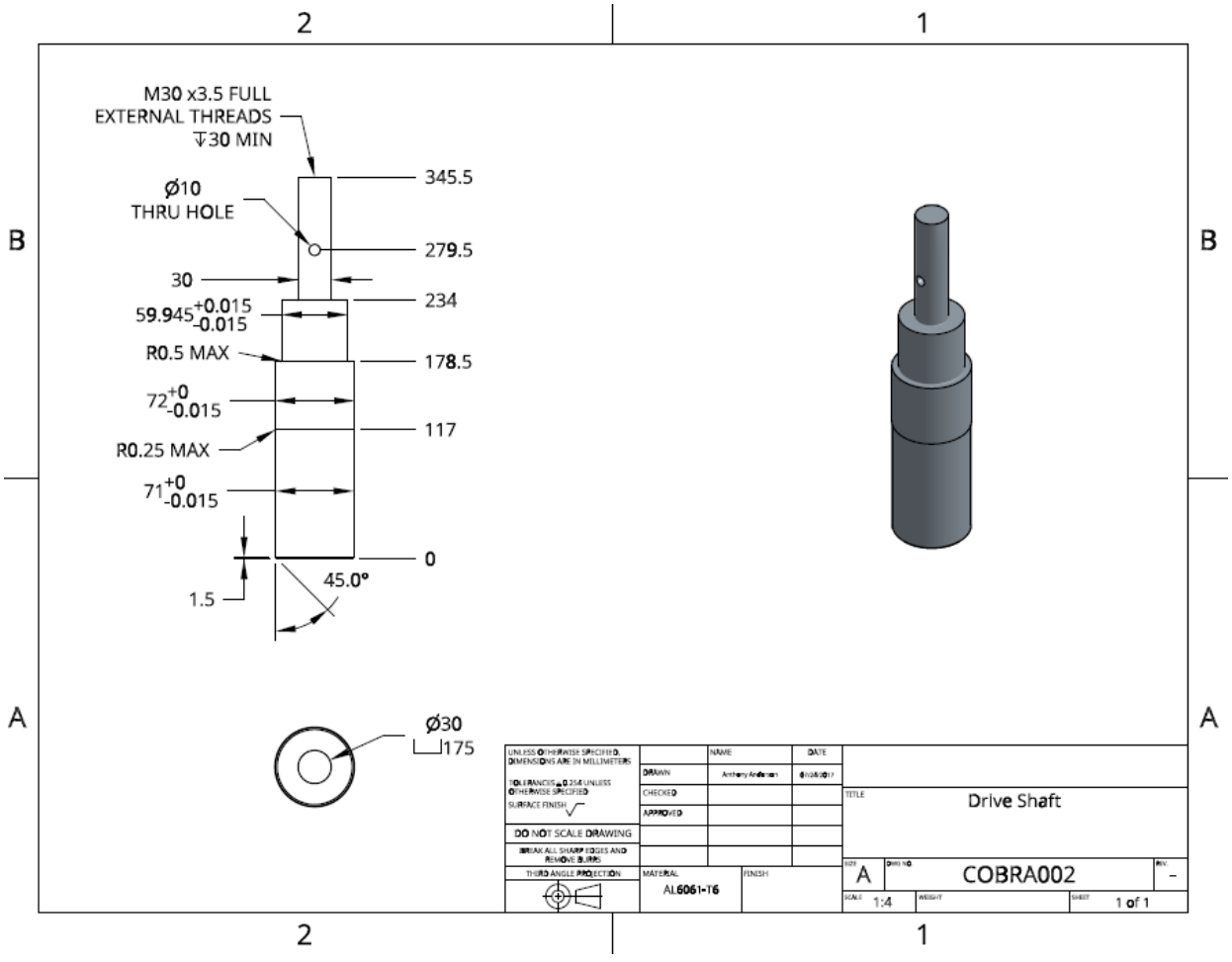

Figure 25: Manufacturing drawing of drive shaft. See Appendix B for all part drawings.

With the shaft designed and bearings selected, the mounting plate design was relatively straightforward. One large plate of aluminum was machined with pilot holes for the motors, shoulders for the bearings, mounting holes for the motors, and additional mounting holes for a support structure (Figure 26).

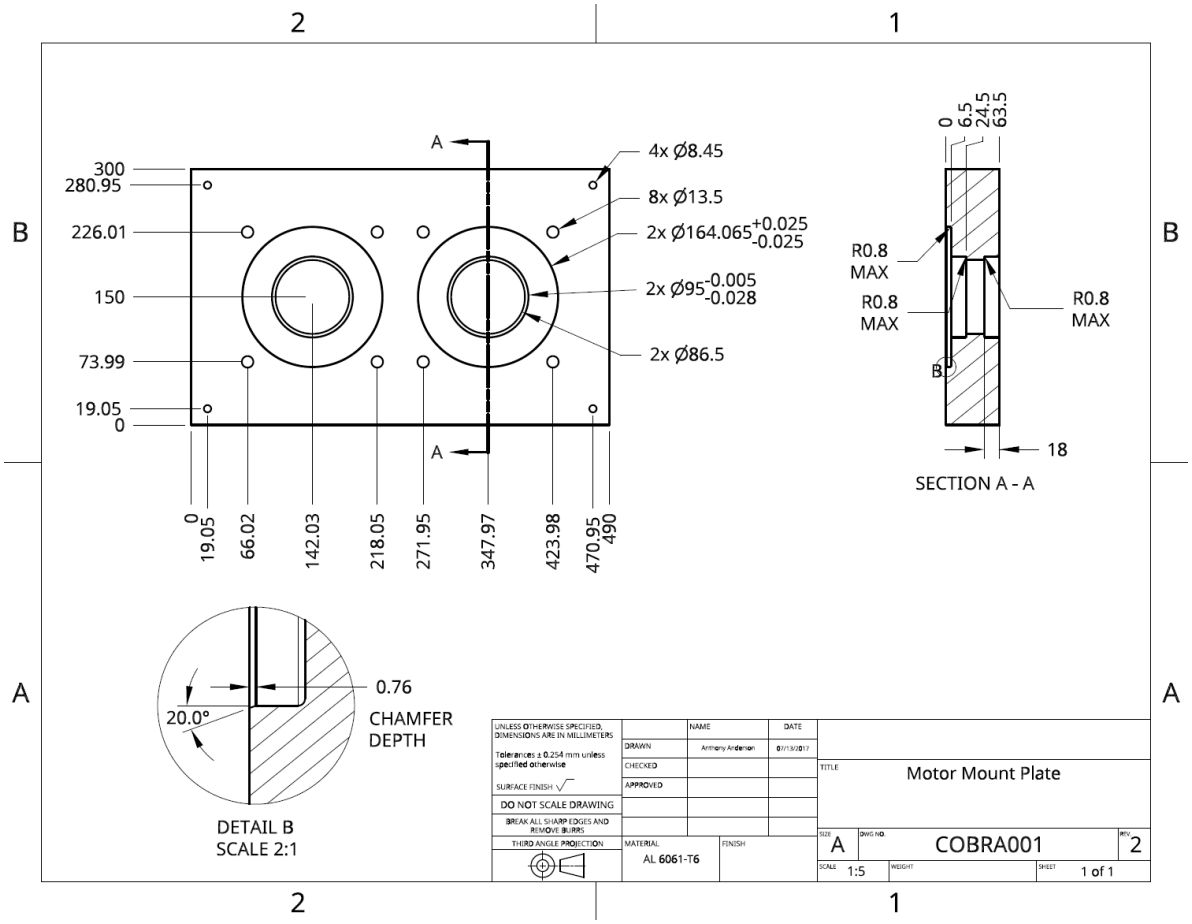

Figure 26: Motor mounting plate manufacturing drawing.

See the next section for an assembly view of the plate, shaft, and bearings.

5.1.3 *Sheave Design*

Our optimization algorithm (Chapter 3) selected sheave radii of 3.4 cm and 1.1 cm for the ankle and knee, respectively. When we designed and manufactured our sheaves, we were using an earlier

iteration of the optimization algorithm that used a less rigorous stiffness model at both the ankle and knee, which chose an ankle sheave radius of 2 centimeters and a knee sheave radius of 5 centimeters. These will be corrected in a future version of the offboard system.

We designed two split-clamp style sheaves to mate with our shafts (Figure 27). Each sheave has a hole through the center for 1) fixing it to the drive shaft and 2) maintaining bearing preload in the event that the nut above the sheave loosens during operation.

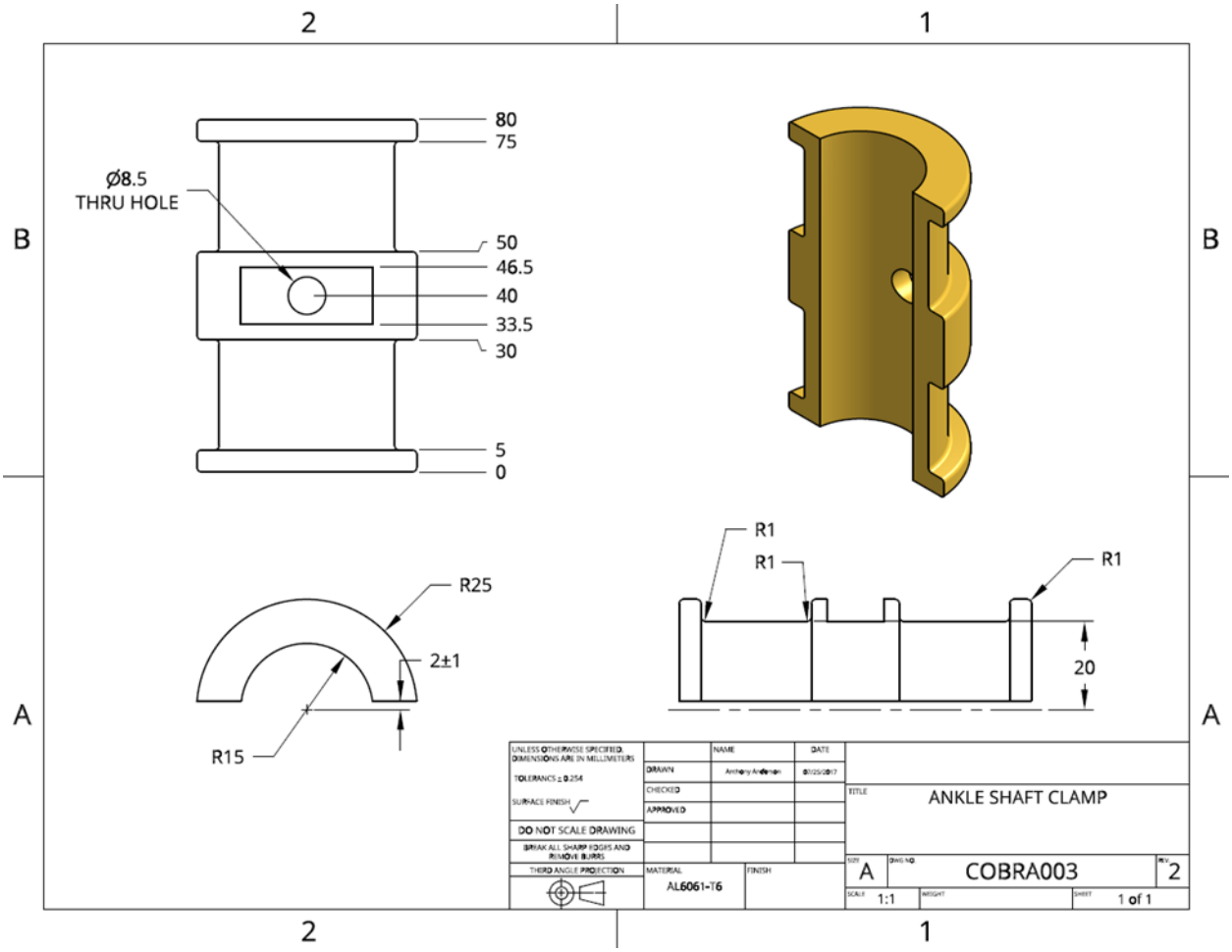

Figure 27: One half of the ankle sheave. Two of the part shown here are required to form a full sheave.

As the tapered roller bearings mentioned in the previous section are made of two separate parts, maintaining a proper amount of preload is important to remove the internal clearances in the

bearing, which prevents excessive shaft movement in the radial direction. The design presented here uses a large nut at the top of each threaded shaft to simultaneously preload the top and bottom bearings (Figure 28).

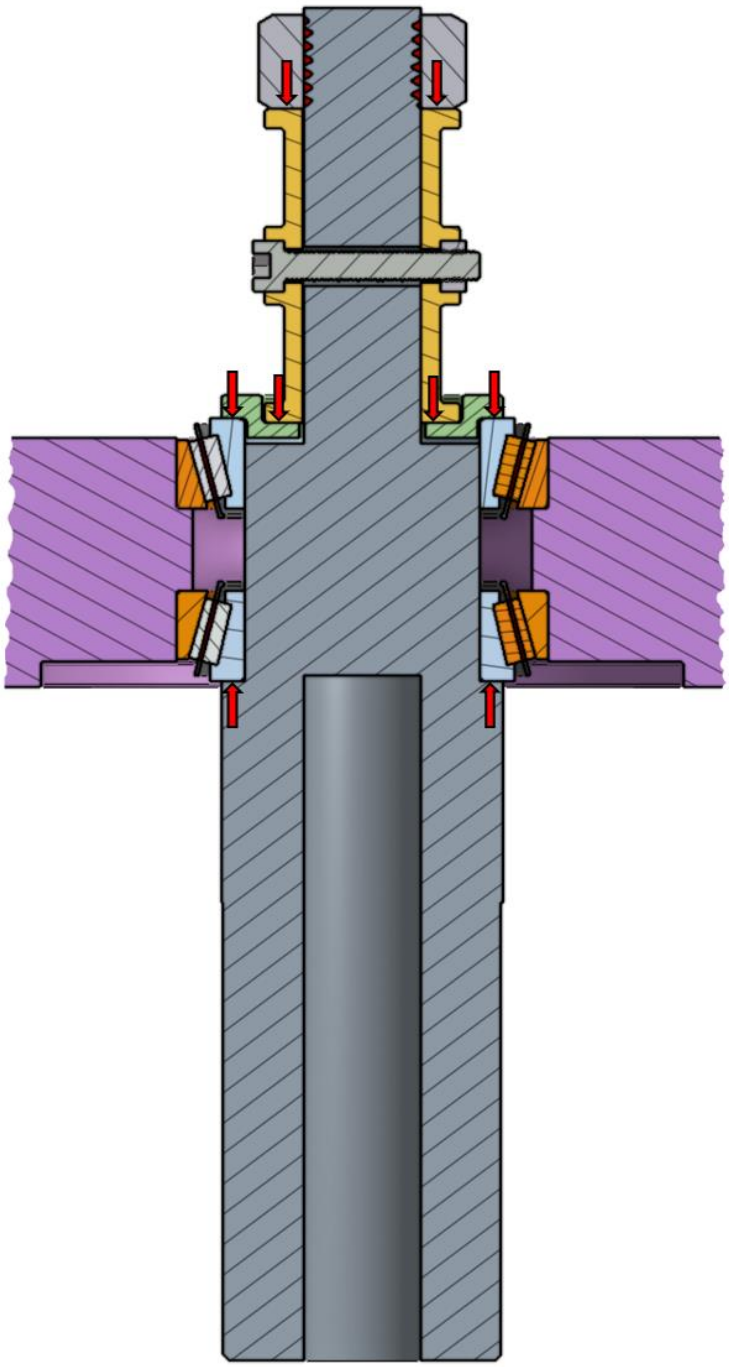

Figure 28: Cross section view of mount plate (purple), shaft (grey), and ankle sheave (yellow) assembly. Bearing preload forces are shown with red arrows. The orange portion of the bearing is press fit into the plate, and the blue portion of the bearing rotates with the shaft. The green spacer was added when we switched from rotary ball bearings to tapered roller bearings.

During initial tests, we found that small differentials in the sheave clamp heights were causing an asymmetric preload on the bearings and causing the shaft to lose perpendicularity with the plate. We redesigned the ankle sheave as a solid shaft sleeve to fix the problem. A once piece sheave with a tight clearance to the shaft ensures preload forces are distributed evenly around the bearing, even if the nut faces or threads are not perfectly perpendicular.

5.1.4 *Bowden Cable Selection and Grounding Plate Design*

As our design required wrapping the inner cable for the Bowden cable around a small sheave, a synthetic rope was selected as the inner cable instead of the more standard wire rope. The synthetic rope (West Marine, Watsonville, CA, USA) has virtually no lateral bending stiffness, but has high strength, low stretch, and low friction. The synthetic rope (Endura) has a 1000-pound breaking strength.

The outer sheath portion of the Bowden cable was selected from a large catalog of Bowden cable components (Lexco Cable, Norridge, IL, USA). The outer sheath is composed of an inner friction reducing liner, a wound metal wire, and a black plastic covering. Threaded end-pieces were also selected to seat the Bowden cables and accept the reaction forces during loading. These end pieces can be adjusted to remove slack from the cable if necessary.

An aluminum plate was designed to ground the Bowden cables to the motor frame. The plate interfaced with the threaded end-pieces and allowed the inner cable to pass through and wrap around the motor sheave. These holes were located so that the rope would pass through the hole and wrap around the sheaves in straight lines to prevent friction.

5.1.5 *Chassis and Power Train Assembly*

The entire assembly is shown in Figure 29. This includes an aluminum frame, the motors, plates, shafts, sheaves, and support hardware.

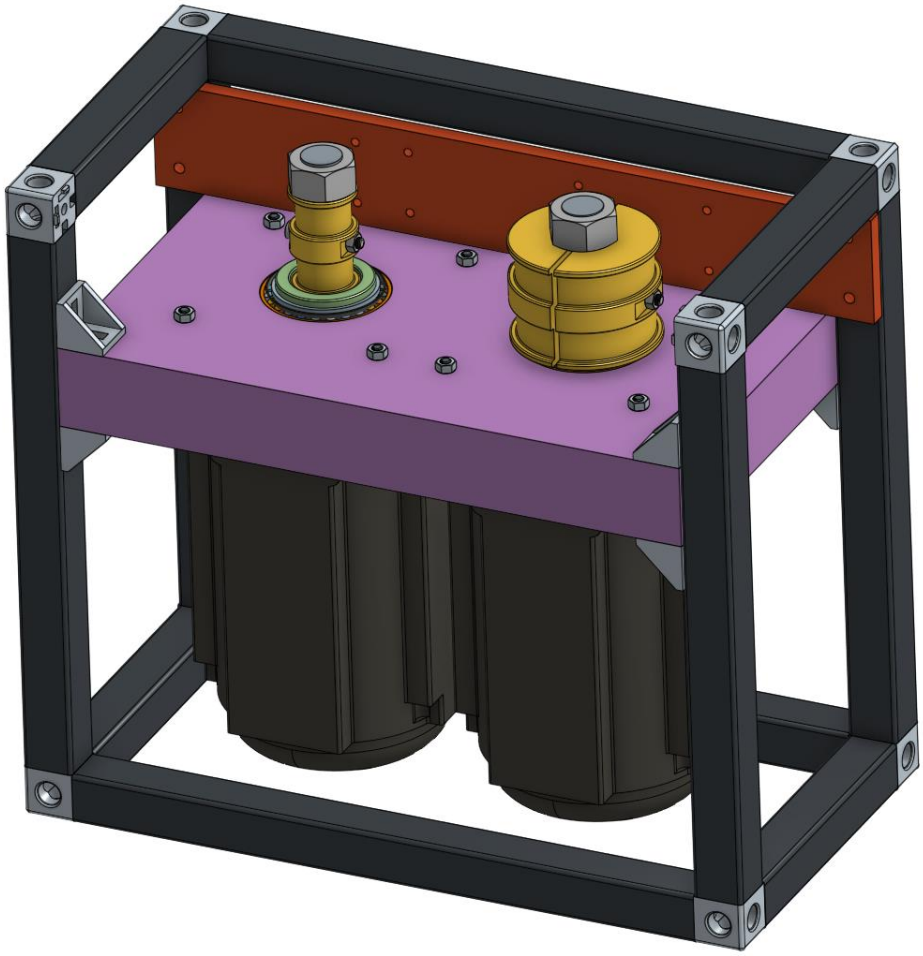

Figure 29: Isometric view of the offboard system mechanical assembly. One aluminum cross-bar has been hidden to show the sheaves more clearly.

A cross section view is shown in Figure 30 to highlight how the motor interfaces with the shaft and bearings.

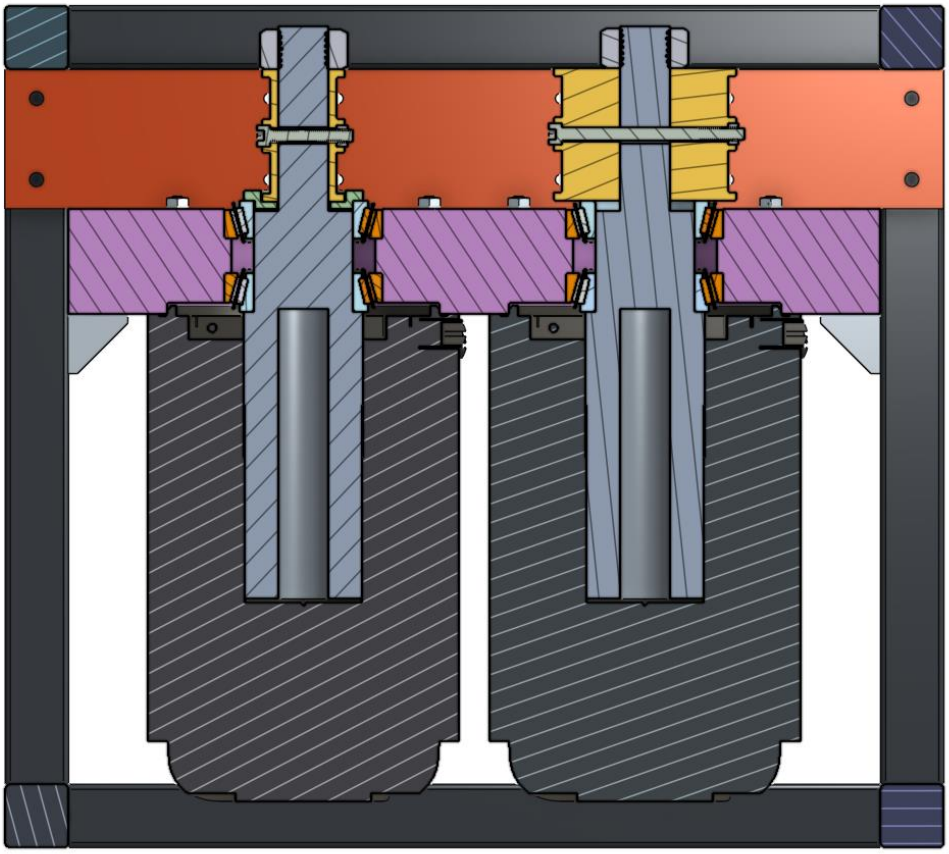

Figure 30: Cross section view of the assembly. Note that the shafts were made hollow in the center to reduce inertia. The motor 3D models provided by the manufacturer do not show the internal rotor-stator or feedback assemblies.

Figure 31 shows the setup after the plates and shafts were manufactured, and motors were installed. This setup pictured was assembled with the rotary ball bearings.

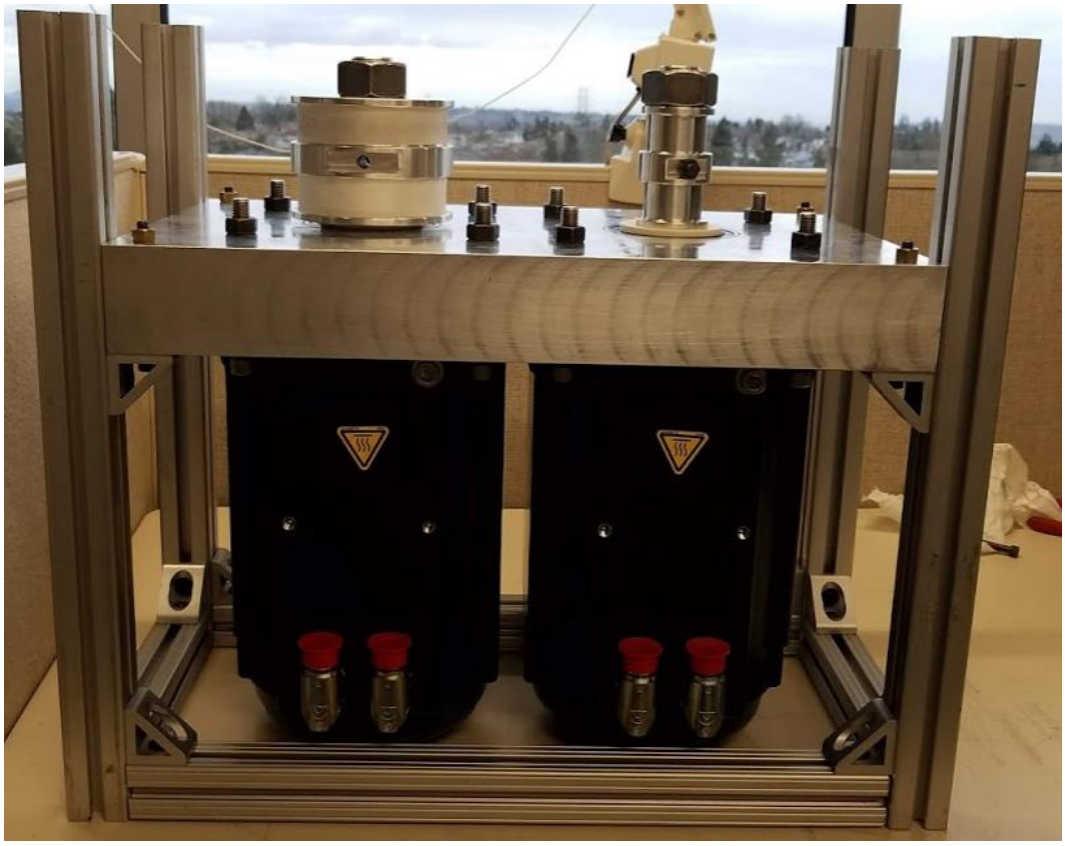

Figure 31: Initial assembly of the mechanical portion of the offboard system.

5.2 Electrical Box Design and Manufacturing

The AKD P02406 servo drives require an auxiliary electrical circuit to deliver the 208 VAC wall power to the drives, deliver 24 V to the drive's internal computer, and implement emergency-stop functionality. We designed and fabricated a high-voltage electrical panel to implement the circuit and house the two servo drives.

Kollmorgen provides a sample wiring diagram to show the primary electrical components necessary to operate the drive. Using this as a starting point, we selected the necessary electrical components from a number of online automation supply distributors. The primary components of the electrical circuit include fuses, a low-pass filter for the power supply lines, power distribution blocks, a 24 V power supply, a motor contactor, and an emergency stop. The 24 V power supply

powers the drive's internal logic circuits and delivers power to the motor contactor and in-line emergency stop. If the emergency button stop is pressed, it 1) cuts a low voltage input 'enable' line to the drive and 2) cuts power to the motor contactor, which cuts the high-voltage inputs to the drive. Figure 32 shows an electrical schematic that was created before fabricating the panel. This schematic is available in Appendix B.

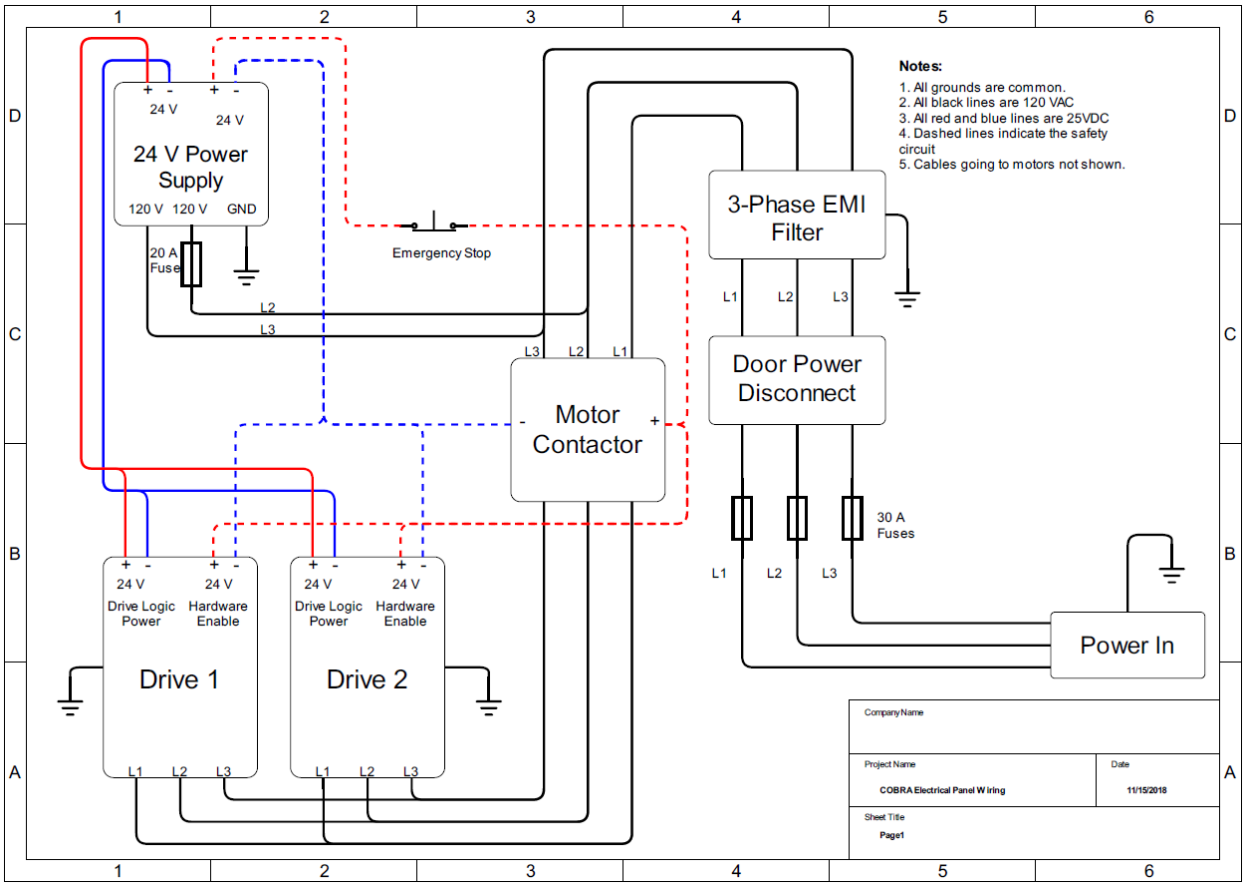

Figure 32: Wiring schematic for electrical panel

An additional safety feature was a power switch connected to the door of the electrical box. In order to open the door to the electrical box, an external switch must be turned that cuts power to most of the components, reducing shock risks. Figure 33, below, shows an image of the completed electrical panel. This custom electrical panel and box was fabricated at the CLIMB

machine shop. Currently, only a single drive is completely wired, as we only have wearable hardware for the ankle.

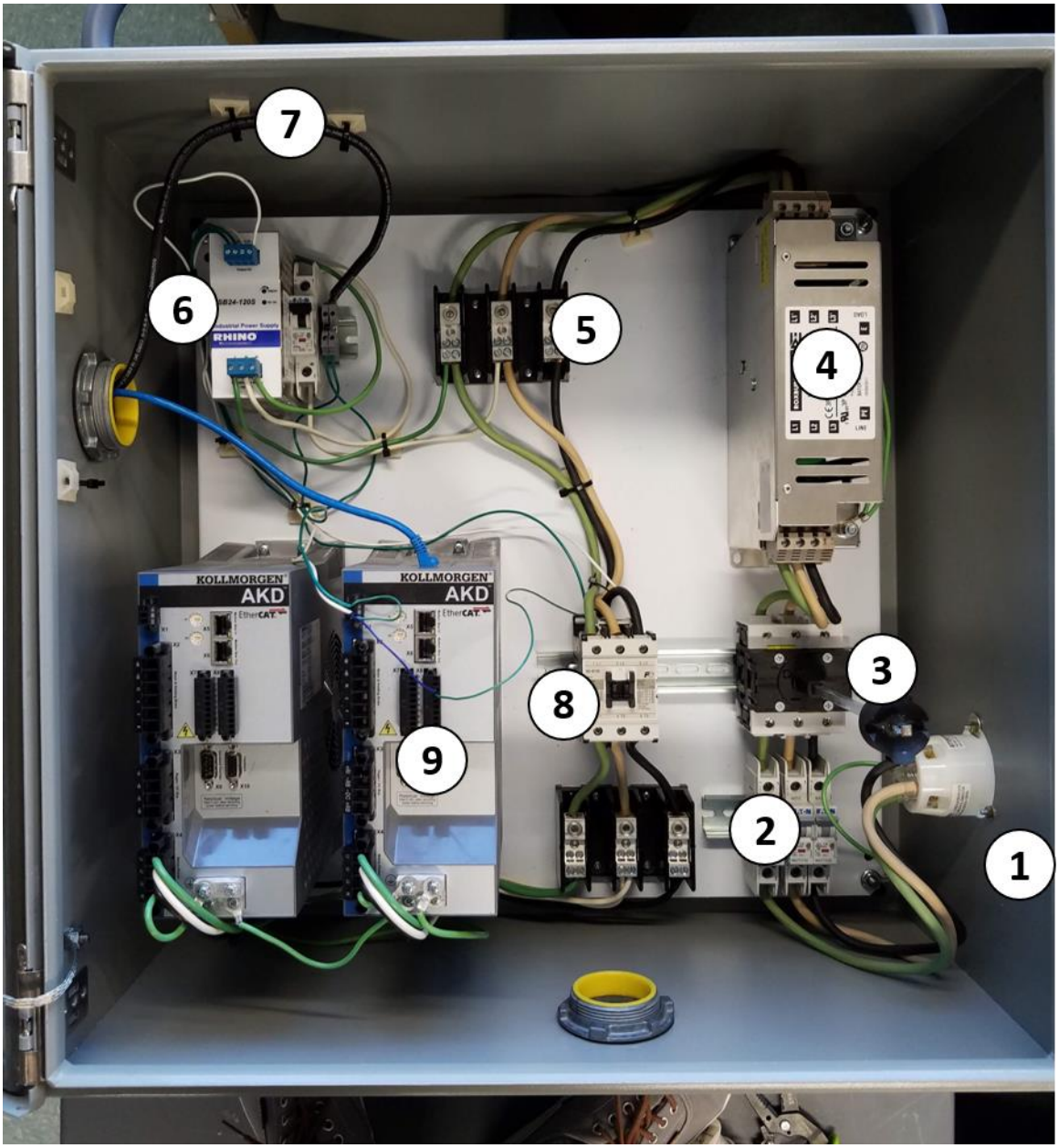

Figure 33: Completed electrical panel. 1. Power inlet 2. Fuses 3. Door power disconnect 4. Low-pass electrical filter 5. Power distribution block 6. 24 Volt power supply 7. Emergency stop cable 8. Motor contactor 9. Servo drive

5.3 PROSTHETIC FOOT DESIGN

5.3.1 *Hardware Design*

In order to retrofit the College Park Venture Foot to be Bowden cable driven, several custom CNC machined parts were necessary. We needed:

1. A plate to mount lever arms to on the distal side of the ankle joint.
2. Lever arms and a small shaft for the cable to pull on.
3. A grounding plate for the Bowden cables on the proximal side of the ankle joint.

The interface between the bottom metal ankle bone and the composite keel in the Venture Foot is curved to allow for the center of rotation to shift forward during stance (Figure 34).

Figure 34: Venture Foot by College Park. The left frame shows the foot in an unloaded state. Note the gap between the carbon fiber keel and metal ankle bone. The right frame shows the foot loaded in dorsiflexion, and the gap has closed. (College Park Industries, Warren, MI)

Our lever arm mounting plate fits between the keel and the bottom ankle bone. When designing the lever arm mount plate, we attempted to match the existing curvature as closely as possible by

measuring the foot in several locations to estimate the radius of curvature. Small wings were added to give a mounting point for lever arms (Figure 35).

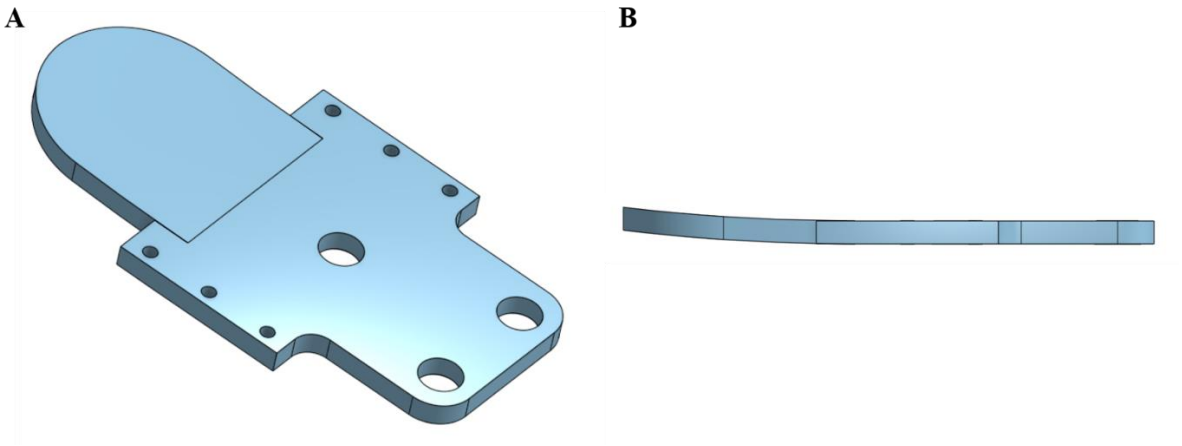

Figure 35: Solid models of the lever arm mounting plate. A) An isometric view showing large holes to mount to the foot and smaller holes for lever arm mounting.

As with the motor sheaves, an earlier version of the optimization algorithm was used to size the moment arms. The nominal moment arm length selected by the earlier algorithm was 8 cm. In order to prevent collisions with the ground or opposite swing leg, the lever arms were made more compact by rotating them upwards from horizontal. Two sets of aluminum lever arms were manufactured, one for each side of the foot, and were connected via a small steel drive shaft. The inner Bowden cables are tied directly to the drive shafts, which are located with external retainer rings (Figure 36).

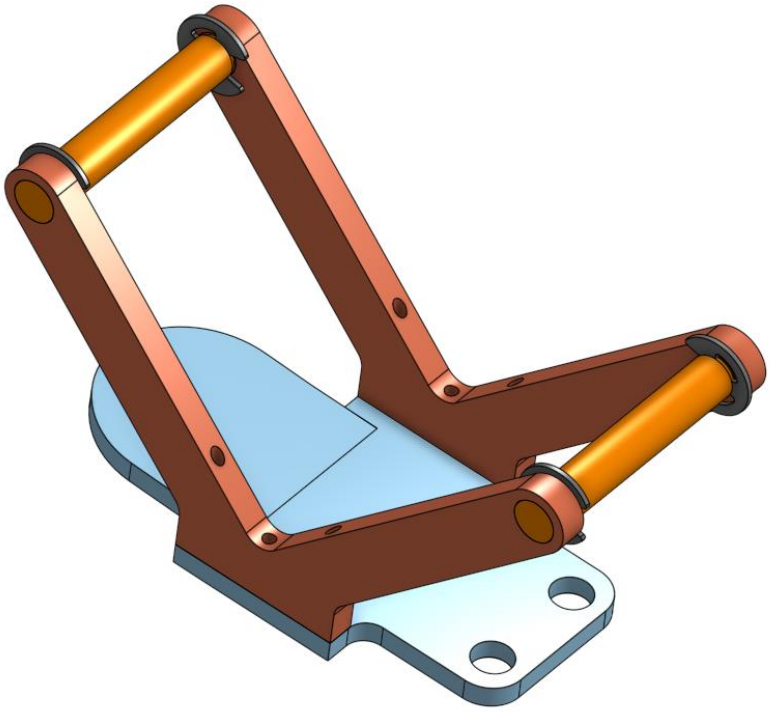

Figure 36: Lever arms (red) and drive shafts (orange). Lever arms are fixed to mounting plate with small screws.

A grounding plate for the Bowden cable was designed that interfaced with the prosthetic pylon. As the lever arms were rotated, a small pulley-bearing (Misumi, Schaumburg, IL, USA) was integrated with the grounding plate to minimize friction during cable routing. Additionally, the pulley allows for the tethers to exit at an angle that clears the residual limb, instead of the angle dictated by the lever arm line of action. The grounding plate attaches to the prosthetic pylon with a standard shaft collar with mounting holes (McMaster-Carr, Elmhurst, IL, USA). Figure 37 shows a rendered image of the Bowden cable grounding plate.

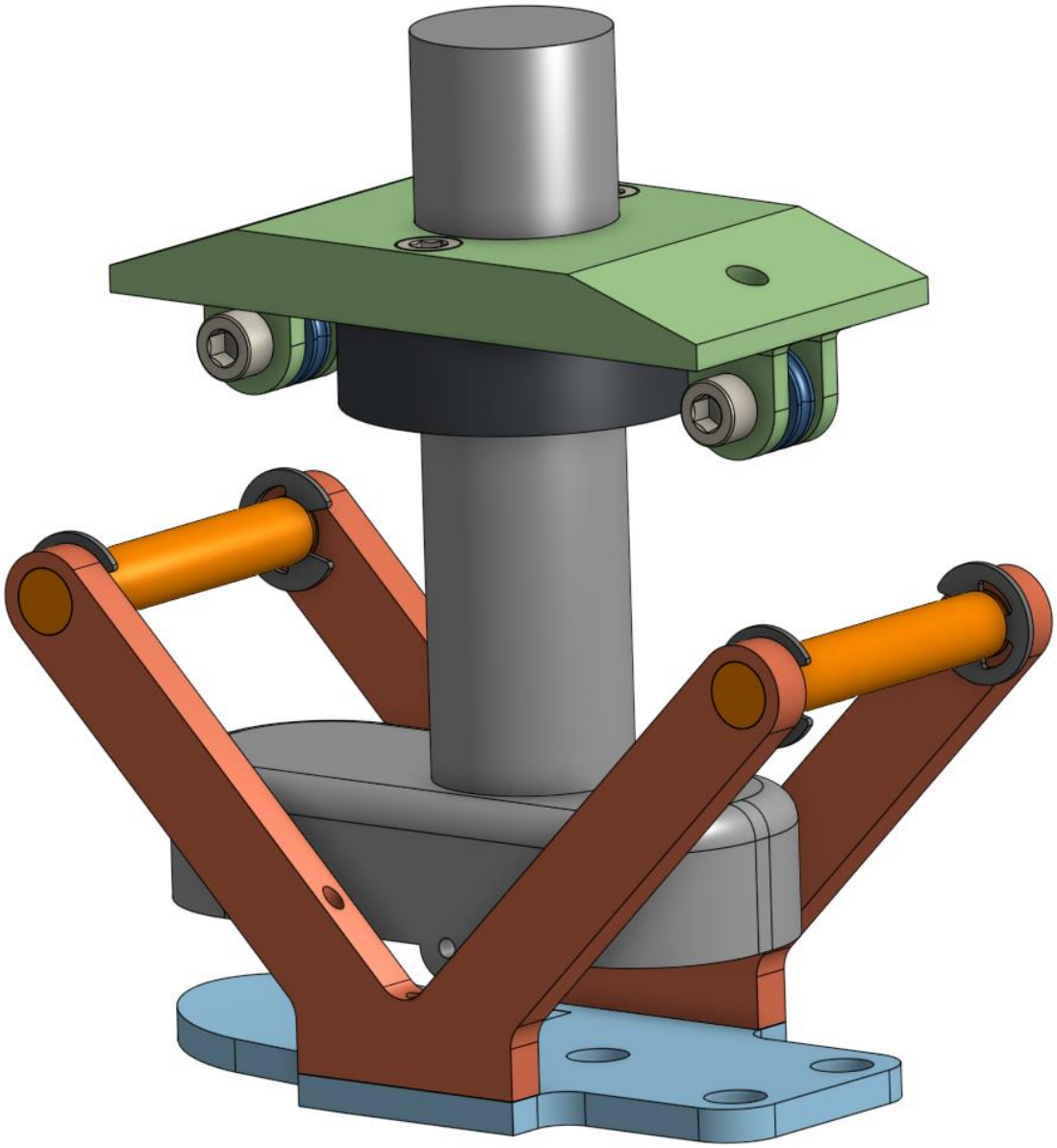

Figure 37: Bowden cable grounding plate (green), pulley bearings (blue), shaft collar (black), and a stand-in piece for the pylon and top ankle bone (grey).

The geometric relationships between all of these components were initially determined in a master sketch to set the nominal moment arm length and to make sure that components would not collide over the ankle joint's range of motion (Figure 38).

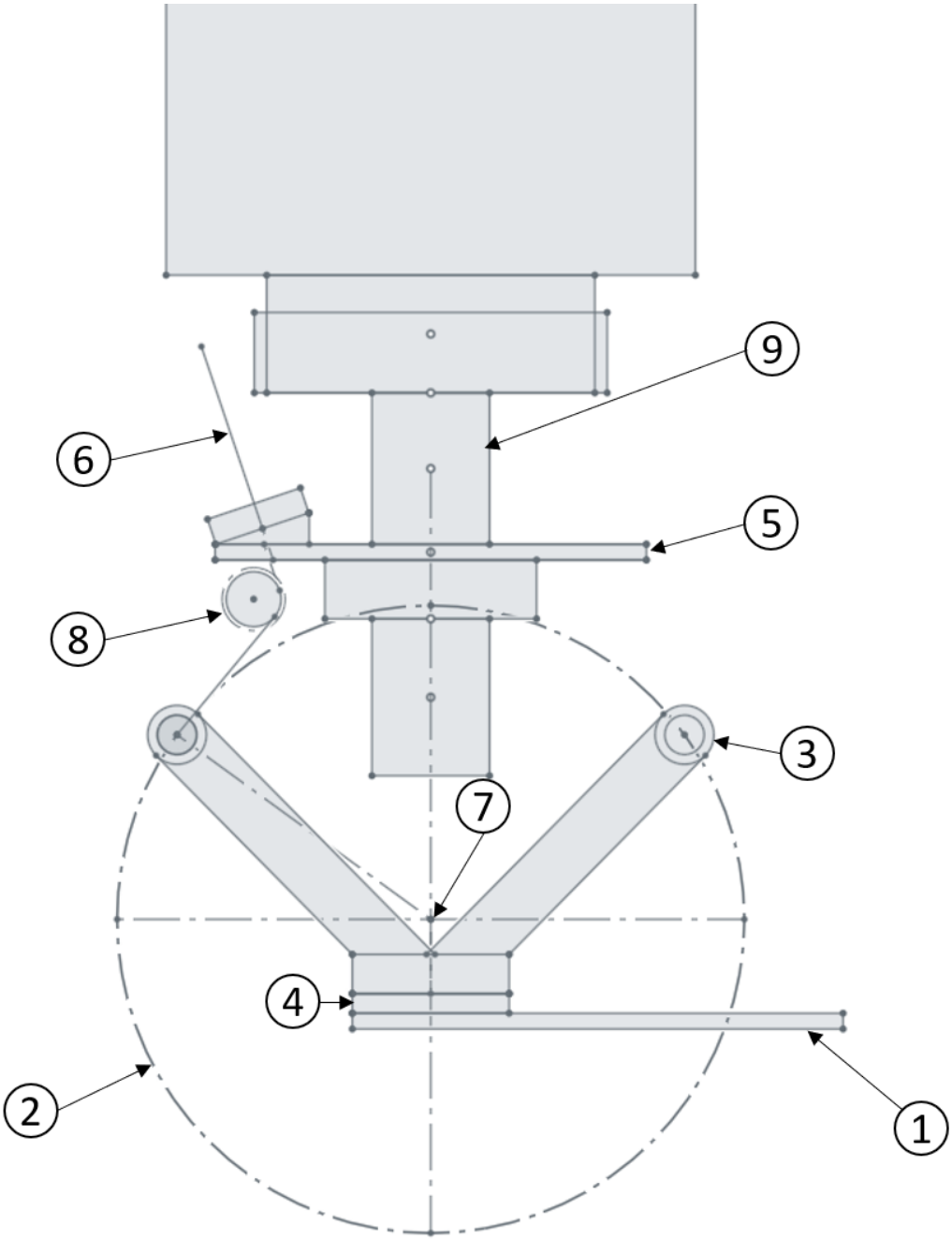

Figure 38: Master sketch of prosthesis lever arm and grounding plate geometry. The pulley-bearing and rope were removed from anterior side of prosthetic foot in this image for clarity. 1) composite keel 2) nominal lever arm length 3) lever arm 4) lever arm mounting plate 5) Bowden cable grounding plate 6) inner Bowden cable line of action 7) ankle rotation center 8) pulley bearing 9) prosthetic pylon.

From the image above, it is clear that the inner Bowden cable will always be tangent to the pulley bearing. The moment arm is 8 cm exactly only when the rope is tangent to the large dashed circle, which only occurs at a single ankle angle. At all other ankle angles, the rope is not perpendicular to the lever arm, and some of the cable force is not transmitted to a moment about the joint. Figure 39 shows this effect. The blue arrow shows the cable line of action, and the orange arrow shows the theoretical line that is tangent to the circle at the origin of the force vector. To compute the cable force that is contributing to torque about the ankle joint, the measured cable force must be multiplied by cosine of the angle between the blue and orange arrows in Figure 39.

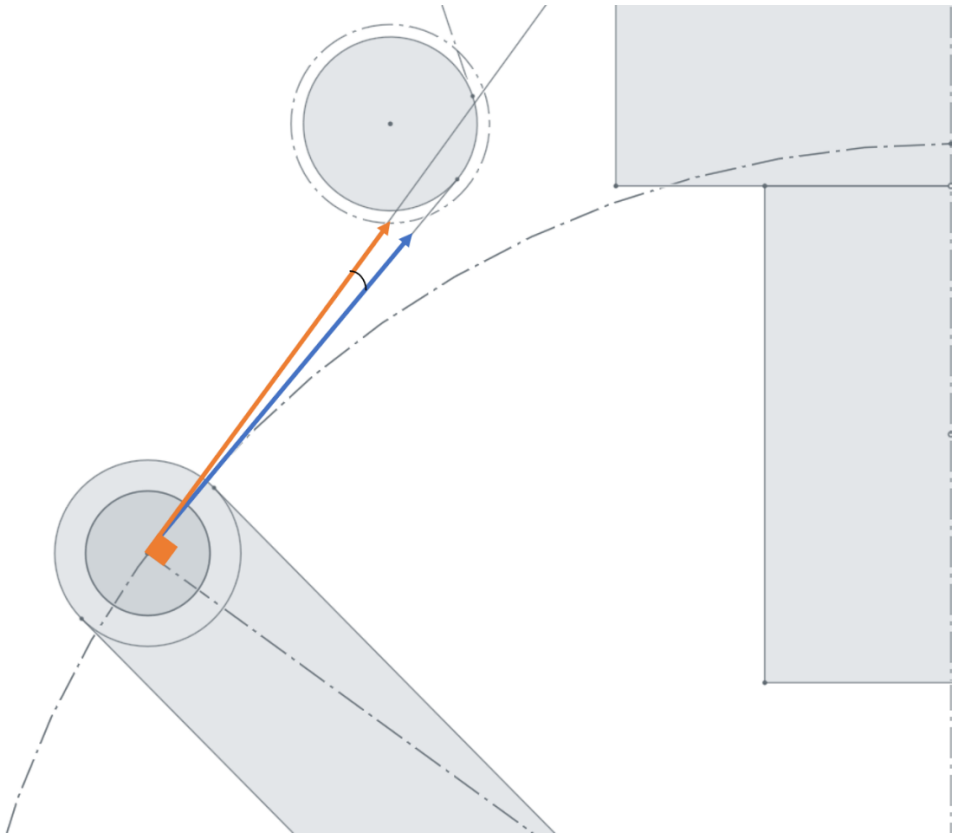

Figure 39: Illustration of variable force vector over prosthesis motion. Orange arrow is tangent to prosthesis center of rotation, blue arrow shows where rope will actually lie.

Hence, the angle between the two vectors in Figure 39 was measured over the prosthesis range of motion. Measurements were made in the CAD sketch as the ankle was rotated from 13 degrees

of dorsiflexion to 25 degrees of plantarflexion in one degree increments. Figure 40 shows this relationship for the plantar flexor and dorsiflexor cables. The cosine of this angle can be considered the ‘force multiplier’ that computes the projection of the force vector onto the tangent line of the circle at the origin of the force vector.

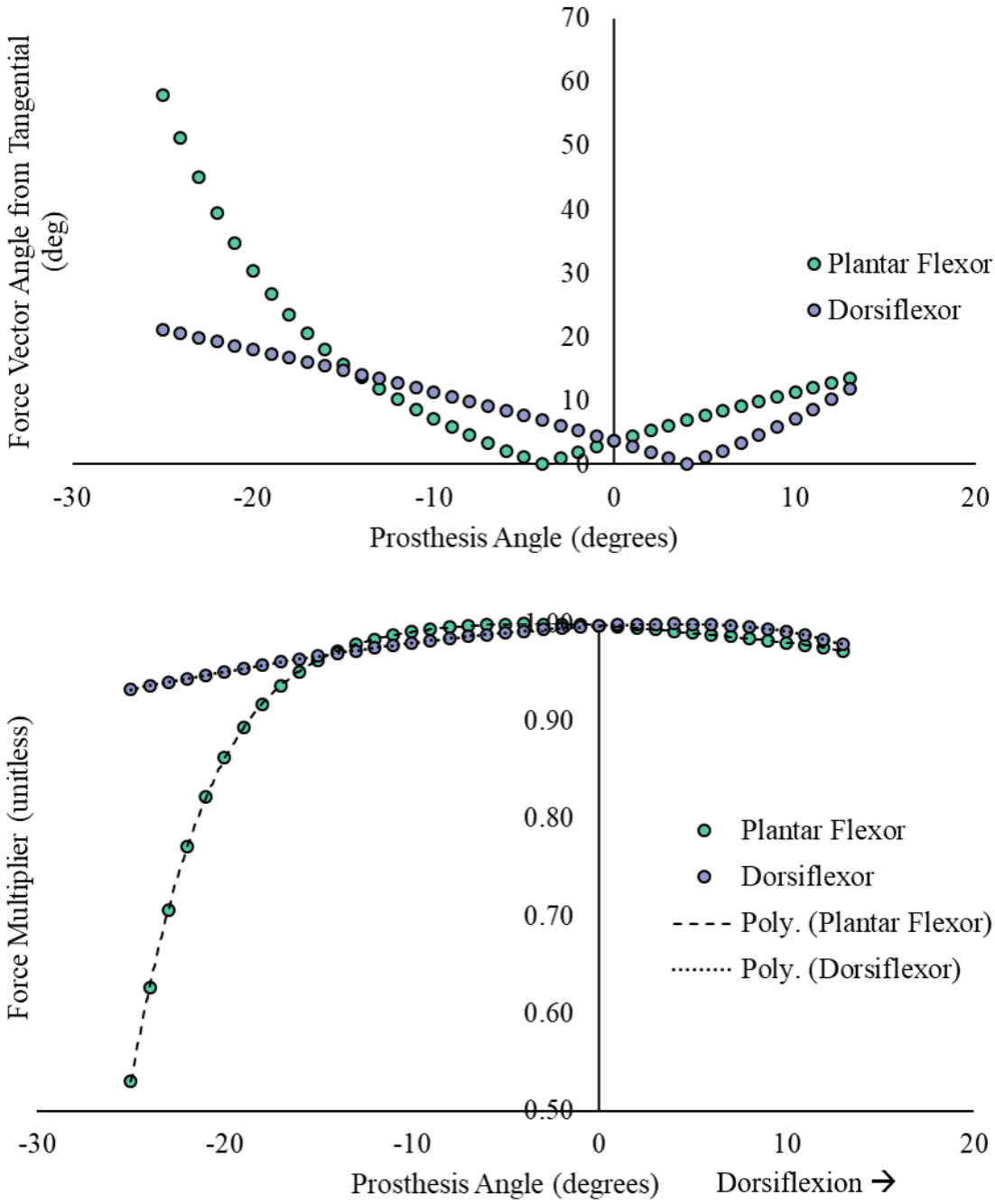

Figure 40: Top) Quantification of force vector angles from previous figure over the prosthesis range of motion. Bottom) Cosine of the angle between the force vectors. This determines the useful fraction of cable force at a given ankle angle.

For both the plantar flexor and dorsiflexor cable, a sixth order polynomial was fit to relate the force multiplier to the ankle angle using MATLAB. Within the control software, this relationship

and the cable force measurement can be quickly computed to determine the applied moment to the ankle joint. If ankle angle is denoted as θ, the force multiplier β can be computed as:

$$\beta_{plantar} = p_1\theta^6 + p_2\theta^5 + p_3\theta^4 + p_4\theta^3 + p_5\theta^2 + p_6\theta + p_7 \quad \text{(eq. 15)}$$

$$\beta_{dorsi} = p_8\theta^6 + p_9\theta^5 + p_{10}\theta^4 + p_{11}\theta^3 + p_{12}\theta^2 + p_{13}\theta + p_{14} \quad \text{(eq. 16)}$$

Parameters $p_1 - p_{14}$ can be found in Table 3. With this information, the applied moment about the ankle can be computed in real-time with the following three equations:

$$\tau_{applied,plantar} = F_{measured,plantar}\beta_{plantar}r \quad \text{(eq. 17)}$$

$$\tau_{applied,dorsi} = F_{measured,dorsi}\beta_{dorsi}r \quad \text{(eq. 18)}$$

$$\tau_{applied,total} = \tau_{applied,dorsi} - \tau_{applied,plantar} \quad \text{(eq. 19)}$$

Where $F_{measured,plantar}$ is the cable force measured on the posterior side of the foot, $F_{measured,dorsi}$ is the cable force measured on the anterior side of the foot, r is the 8 cm moment arm, and $\beta_{plantar}$ and β_{dorsi} are the force multipliers that accounts for the rope-moment arm angle. As Equation 19 indicates, the total moment applied to the joint must account for the fact that the plantar and dorsi flexor cables act antagonistically.

Table 3: Regression parameters for force multiplier calculation

Parameter	**P1**	**P2**	**P3**	**P4**	**P5**	**P6**	**P7**
Plantar	-2.00E-09	-1.00E-08	4.00E-07	7.00E-06	-0.0001	-0.0011	9.98E-01
Parameter	**P8**	**P9**	**P10**	**P11**	**P12**	**P13**	**P14**
Dorsi	-1.00E-10	-7.00E-09	-2.00E-07	-3.00E-06	-1.00E-04	0.001	0.998

5.3.2 *Sensor Integration and Full Assembly*

The through hole load cells for cable force were placed directly on the surface of the Bowden cable grounding plate on the prosthetic foot side of the cable. Two custom parts were 3D printed to hold the rotary encoder and magnetic actuator. The part of the mount that holds the encoder was retrofit

to press into an existing space on the top ankle bone of the prosthesis, and the part that holds the magnetic actuator grips the outside of the lever arms. Additionally, shaft sleeves were printed to locate the ropes on the drive shafts. Figures 41 and 42 show multiple views of the completed prosthetic foot.

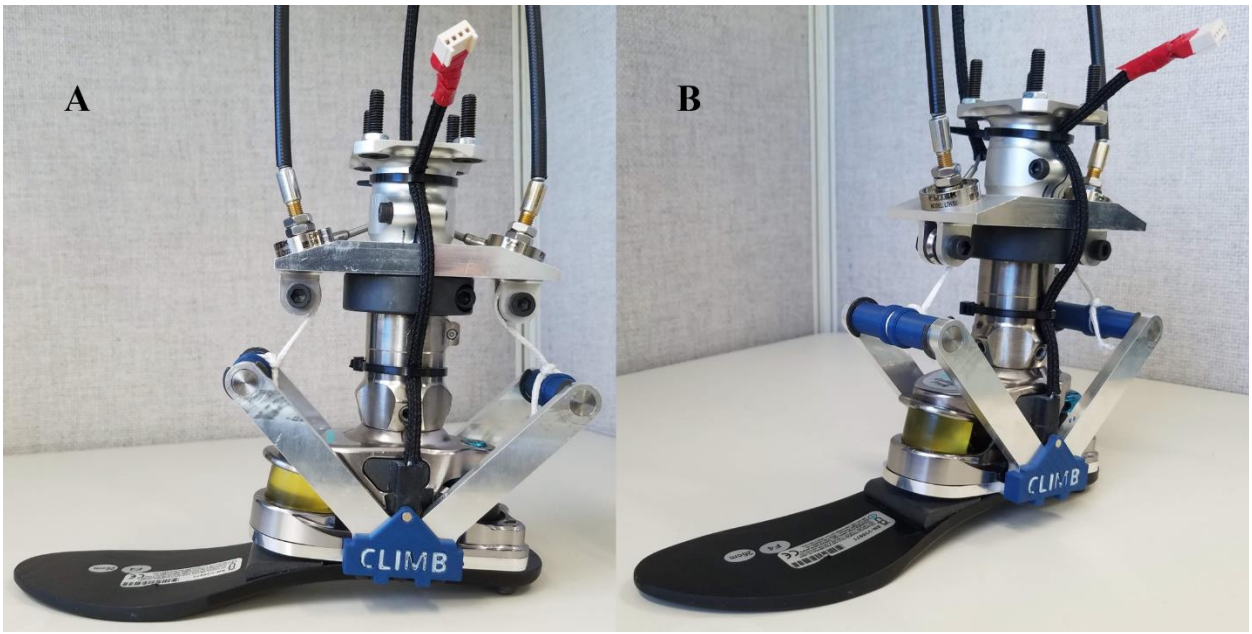

Figure 41: Completed foot hardware. A) Lateral view of the foot B) Anterior-Lateral view of the foot

In Figure 41, the blue 3D-printed piece on the lateral portion of the foot holds the magnetic actuator part of the joint encoder. The sensing portion is housed within a grey 3D-printed piece that was press-fit into the side of the foot and then taped in place.

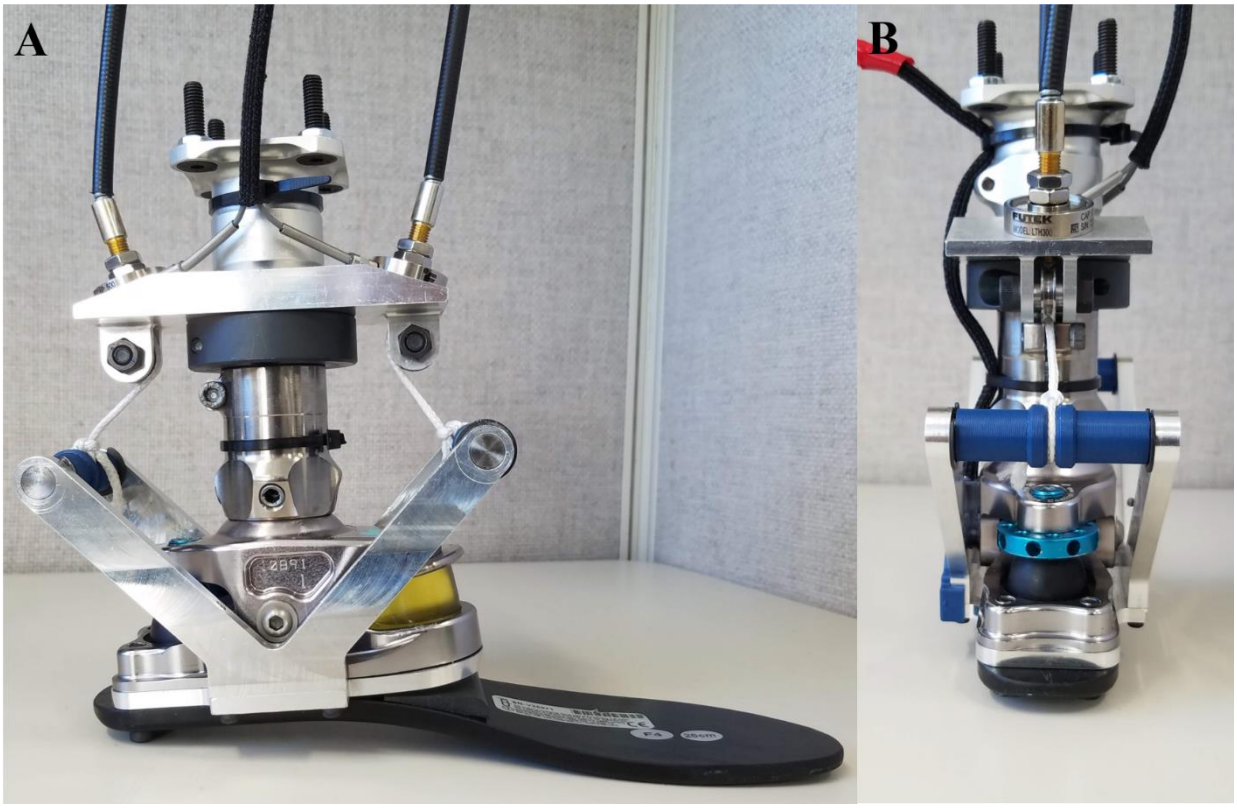

Figure 42: Alternate views of completed foot hardware. A) Medial view B) Posterior view

BIBLIOGRAPHY

[1] R. S. Gailey *et al.*, "Energy expenditure of trans-tibial amputees during ambulation at self-selected pace," *Prosthet. Orthot. Int.*, vol. 18, no. 2, pp. 84–91, Aug. 1994.

[2] T. P. Stitik and P. M. Foye, "The Prevalence of Knee Pain and Symptomatic Knee Osteoarthritis Among Veteran Traumatic Amputees and Nonamputees," *Arch. Phys. Med. Rehabil.*, vol. 86, no. 6, p. 1273, Jun. 2005.

[3] P. L. Ephraim, S. T. Wegener, E. J. MacKenzie, T. R. Dillingham, and L. E. Pezzin, "Phantom Pain, Residual Limb Pain, and Back Pain in Amputees: Results of a National Survey," *Arch. Phys. Med. Rehabil.*, vol. 86, no. 10, pp. 1910–1919, Oct. 2005.

[4] J. Kulkarni, W. J. Gaine, J. G. Buckley, J. J. Rankine, and J. Adams, "Chronic low back pain in traumatic lower limb amputees," *Clin. Rehabil.*, vol. 19, no. 1, pp. 81–86, Feb. 2005.

[5] K. Ziegler-Graham, E. J. MacKenzie, P. L. Ephraim, T. G. Travison, and R. Brookmeyer, "Estimating the Prevalence of Limb Loss in the United States: 2005 to 2050," *Arch. Phys. Med. Rehabil.*, vol. 89, no. 3, pp. 422–429, Feb. 2008.

[6] R. Gailey, "Review of secondary physical conditions associated with lower-limb amputation and long-term prosthesis use," *J. Rehabil. Res. Dev.*, vol. 45, no. 1, pp. 15–30, Dec. 2008.

[7] Pieter Struyf, C. van Heugten, M. Hitters, and R. Smeets, "The Prevalence of Osteoarthritis of the Intact Hip and Knee Among Traumatic Leg Amputees," *Arch. Phys. Med. Rehabil.*, vol. 90, no. 3, pp. 440–446, 2009.

[8] A. J. Yoder, A. J. Petrella, and A. K. Silverman, “Trunk–pelvis motion, joint loads, and muscle forces during walking with a transtibial amputation,” *Gait Posture*, vol. 41, no. 3, pp. 757–762, Mar. 2015.

[9] S. H. Collins and A. D. Kuo, “Recycling Energy to Restore Impaired Ankle Function during Human Walking,” *PLOS ONE*, vol. 5, no. 2, p. e9307, Feb. 2010.

[10] “Endolite Elan Foot,” *Prosthetic Solutions*. [Online]. Available: http://www.prostheticsolutionsinc.com/cust-product/endolite-elan-foot/. [Accessed: 18-Oct-2018].

[11] M. K. Shepherd and E. J. Rouse, “The VSPA Foot: A Quasi-Passive Ankle-Foot Prosthesis with Continuously Variable Stiffness,” *IEEE Trans. Neural Syst. Rehabil. Eng.*, vol. PP, no. 99, pp. 1–1, 2017.

[12] H. M. Herr and A. M. Grabowski, “Bionic ankle-foot prosthesis normalizes walking gait for persons with leg amputation,” *Proc. Biol. Sci.*, vol. 279, no. 1728, pp. 457–464, 2012.

[13] “Ottobock Empower,” *Empower*. [Online]. Available: https://www.ottobockus.com/prosthetics/lower-limb-prosthetics/solution-overview/empower-ankle/. [Accessed: 18-Oct-2018].

[14] K. E. Zelik and P. G. Adamczyk, “A unified perspective on ankle push-off in human walking,” *J. Exp. Biol.*, vol. 219, no. 23, pp. 3676–3683, Dec. 2016.

[15] M. D. Geil, M. Parnianpour, P. Quesada, N. Berme, and S. Simon, “Comparison of methods for the calculation of energy storage and return in a dynamic elastic response prosthesis,” *J. Biomech.*, vol. 33, no. 12, pp. 1745–1750, Dec. 2000.

[16] K. Junius, M. Moltedo, P. Cherelle, C. Rodriguez-Guerrero, B. Vanderborght, and D. Lefeber, “Biarticular elements as a contributor to energy efficiency: biomechanical review

and application in bio-inspired robotics," *Bioinspir. Biomim.*, vol. 12, no. 6, p. 061001, 2017.

[17] R. L. Lenhart, C. A. Francis, A. L. Lenz, and D. G. Thelen, "Empirical evaluation of gastrocnemius and soleus function during walking - ClinicalKey," *J. Biomech.*, vol. 47, no. 12, pp. 2969–2974, 2014.

[18] R. J. Zmitrewicz, R. R. Neptune, and K. Sasaki, "Mechanical energetic contributions from individual muscles and elastic prosthetic feet during symmetric unilateral transtibial amputee walking: A theoretical study," *J. Biomech.*, vol. 40, no. 8, pp. 1824–1831, 2007.

[19] A. E. Ferris, J. M. Aldridge, C. A. Rábago, and J. M. Wilken, "Evaluation of a Powered Ankle-Foot Prosthetic System During Walking," *Arch. Phys. Med. Rehabil.*, vol. 93, no. 11, pp. 1911–1918, Nov. 2012.

[20] R. R. Neptune, S. A. Kautz, and F. E. Zajac, "Contributions of the individual ankle plantar flexors to support, forward progression and swing initiation during walking," *J. Biomech.*, vol. 34, no. 11, pp. 1387–1398, Nov. 2001.

[21] D. J. Cleather, D. F. L. Southgate, and A. M. J. Bull, "The role of the biarticular hamstrings and gastrocnemius muscles in closed chain lower limb extension," *J. Theor. Biol.*, vol. 365, pp. 217–225, Jan. 2015.

[22] M. F. Eilenberg, J.-Y. Kuan, and H. Herr, "Development and Evaluation of a Powered Artificial Gastrocnemius for Transtibial Amputee Gait," *Journal of Robotics*, 2018. [Online]. Available: https://www.hindawi.com/journals/jr/2018/5951965/. [Accessed: 14-Sep-2018].

[23] P. Malcolm, S. Galle, W. Derave, and D. De Clercq, “Bi-articular Knee-Ankle-Foot Exoskeleton Produces Higher Metabolic Cost Reduction than Weight-Matched Mono-articular Exoskeleton,” *Front. Neurosci.*, vol. 12, 2018.

[24] S. L. Delp *et al.*, “OpenSim: Open-Source Software to Create and Analyze Dynamic Simulations of Movement,” *IEEE Trans. Biomed. Eng.*, vol. 54, no. 11, pp. 1940–1950, Nov. 2007.

[25] A. Willson, “A Quasi-Passive Biarticular Prosthesis and Novel Musculoskeletal Model for Transtibial Amputees,” University of Washington, 2017.

[26] A. Willson, C. Richburg, J. Czerniecki, K. Steele, and P. M. Aubin, “Design and Development of a Quasi-Passive Transtibial Biarticular Prosthesis to Replicate Gastrocnemius Function in Walking,” *ASME J. Med. Devices*, Accepted 2018.

[27] A. Willson, C. Richburg, A. Anderson, J. Czerniecki, K. Steele, and P. M. Aubin, “Full Body Musculoskeletal Model Simulations of Gait in Persons with Transtibial Amputation,” *ASME J. Biomech. Eng.*, Submitted 2018.

[28] A. Willson, C. Richburg, A. Anderson, J. Czerniecki, K. Steele, and P. M. Aubin, “Evaluation of a Quasi-Passive Transtibial Biarticular Prosthesis to Replicate Gastrocnemius Function in Walking,” *J. Biomech.*, Submitted 2018.

[29] J. M. Caputo and S. H. Collins, “An experimental robotic testbed for accelerated development of ankle prostheses,” in *IEEE International Conference on Robotics and Automation*, 2013, pp. 2645–2650.

[30] K. E. Gordon and D. P. Ferris, “Learning to walk with a robotic ankle exoskeleton,” *J. Biomech.*, vol. 40, pp. 2636–2644, 2007.

[31] J. R. Koller, D. H. Gates, D. P. Ferris, and C. D. Remy, “Confidence in the curve: Establishing instantaneous cost mapping techniques using bilateral ankle exoskeletons,” *J. Appl. Physiol.*, vol. 122, no. 2, pp. 242–252, Feb. 2017.

[32] K. B. Heer, “Design and Control of a Lower-Limb Exoskeleton Emulator for Accelerated Development of Gait Exoskeletons,” M.S., Colorado School of Mines, United States -- Colorado, 2017.

[33] L. Grazi, S. Crea, A. Parri, R. Molino Lova, S. Micera, and N. Vitiello, “Gastrocnemius Myoelectric Control of a Robotic Hip Exoskeleton Can Reduce the User’s Lower-Limb Muscle Activities at Push Off,” *Front. Neurosci.*, vol. 12, 2018.

[34] H. Vallery, J. Veneman, E. van Asseldonk, R. Ekkelenkamp, M. Buss, and H. van D. Kooij, “Compliant actuation of rehabilitation robots,” *IEEE Robot. Autom. Mag.*, vol. 15, no. 3, pp. 60–69, Sep. 2008.

[35] A. Schiele, P. Letier, R. V. D. Linde, and F. V. D. Helm, “Bowden Cable Actuator for Force-Feedback Exoskeletons,” in *2006 IEEE/RSJ International Conference on Intelligent Robots and Systems*, 2006, pp. 3599–3604.

[36] J. F. Veneman, R. Ekkelenkamp, R. Kruidhof, F. C. T. van der Helm, and H. van der Kooij, “A Series Elastic- and Bowden-Cable-Based Actuation System for Use as Torque Actuator in Exoskeleton-Type Robots,” *Int. J. Robot. Res.*, vol. 25, no. 3, pp. 261–281, Mar. 2006.

[37] H. L. Bartlett, B. E. Lawson, and M. Goldfarb, “Optimal Transmission Ratio Selection for Electric Motor Driven Actuators With Known Output Torque and Motion Trajectories,” *J. Dyn. Syst. Meas. Control*, vol. 139, no. 10, p. 101013, 2017.

[38] S. Rezazadeh and J. W. Hurst, “On the optimal selection of motors and transmissions for electromechanical and robotic systems,” in *2014 IEEE/RSJ International Conference on Intelligent Robots and Systems*, 2014, pp. 4605–4611.

[39] R. L. Waters, B. R. Lunsford, J. Perry, and R. Byrd, “Energy-speed relationship of walking: standard tables,” *J. Orthop. Res. Off. Publ. Orthop. Res. Soc.*, vol. 6, no. 2, pp. 215–222, 1988.

[40] J. Hartung, C. Mergl, C. Henneke, R. Madrid-Dusik, and H. Bubb, “Measuring Soft Tissue Compliance of the Human Thigh,” SAE International, Warrendale, PA, SAE Technical Paper 2004-01–2158, Jun. 2004.

[41] Y. Ding *et al.*, “Biomechanical and Physiological Evaluation of Multi-Joint Assistance With Soft Exosuits,” *IEEE Trans. Neural Syst. Rehabil. Eng.*, vol. 25, no. 2, pp. 119–130, Feb. 2017.

[42] M. B. Yandell, B. T. Quinlivan, D. Popov, C. Walsh, and K. E. Zelik, “Physical interface dynamics alter how robotic exosuits augment human movement: implications for optimizing wearable assistive devices,” *J. NeuroEngineering Rehabil.*, vol. 14, no. 1, Dec. 2017.

[43] A. D. Dongyang Chen, A. D. Youngmok Yun, and A. D. Deshpande, “Experimental characterization of Bowden cable friction,” in *Robotics and Automation (ICRA), 2014 IEEE International Conference on*, 2014, pp. 5927–5933.

[44] J. J. Eng and D. A. Winter, “Kinetic analysis of the lower limbs during walking: What information can be gained from a three-dimensional model?,” *J. Biomech.*, vol. 28, no. 6, pp. 753–758, Jun. 1995.

[45] M. R. Tucker *et al.*, “Control strategies for active lower extremity prosthetics and orthotics: a review,” *J. NeuroEngineering Rehabil.*, vol. 12, no. 1, 2015.

[46] J. M. Caputo and S. H. Collins, “A Universal Ankle-Foot Prosthesis Emulator for Human Locomotion Experiments,” *J. Biomech. Eng.*, vol. 136, no. 3, Dec. 2013.

APPENDIX A

This appendix contains the custom Matlab scripts necessary to simulate the COBRA system. The included scripts are listed with brief descriptions of their functionality.

- *motorSimulationCobra.m* – This script is the primary simulation script. Given system parameters and joint trajectories, the script returns the motor velocity and torque necessary to achieve the desired motion.
- *stiffnessModelCobra.m* – This script is called by motorSimulationCobra.m when simulating the knee joint. Given an orthosis torque, the script returns the additional rotation due to soft tissue compression.
- *finiteDifferenceApprox.m* – This script is derivative approximator. Given a single time series signal, the script will return a signal that is a 4^{th} order accurate estimate of its derivative.
- *myButterFilter.m* – Given a time vector, a noisy signal, and some filtering parameters, this function implements Matlab's Butterworth filter in a single convenient function call.

```
function [motorVelocity,motorTorque,xCable,cableForce]...
          = motorSimulationCobra(time, jointTorquePerBm, jointAngle, Bm, Im,...
                        kb, rj, rm, soft)
% motorSystem.m: Pass in healthy joint kinetics and kinematics and system
% parameters, and return time varying force and motion vectors for system.
%
%   Pass in arguments in the following order:
%       1. time -- vector of time in seconds
%       2. jointTorquePerBM -- time vector of normalized healthy joint
%          torque in N-m-kg^-1
%       3. jointAngle -- time vector of joint angle in radians (be sure
%          that flexion has same sign for torque and angle).
%       4. Bm -- Body mass of person in
%       5. Im -- Motor Inertia in kg-m^2
%       6. kb -- Stiffness of bowden cable in N-m^-1
%       7. rj -- Joint moment arm in m
%       8. rm -- Motor pulley moment arm
%       9. soft -- set to 1 to include tissue compliance at the knee
%
%   The function outputs will be:
%       1. motorVelocity
%       2. motorTorque
%       3. xCable
%       4. cableForce

% Scale joint torque to body mass
jointTorque = jointTorquePerBm*Bm;

% Add orthosis-angle to joint angle
wearableMotion = stiffnessModelICRA(jointTorque)';
wearableAngle = jointAngle + soft*wearableMotion;

% Compute cable force
cableForce = 2*jointTorque./rj;

xCable = rj.*wearableAngle + cableForce./kb;

% Compute motor angle
motorAngle = (xCable./rm);

% Compute motor velocity and acceleration
motorVelocity = finiteDifferenceApprox(time, motorAngle);
motorAcceleration = finiteDifferenceApprox(time, motorVelocity);

% Noise is introduced to the motor velocity and acceleration due to the
% finite difference derivatives. Filter the velocity and acceleration using
% an 8th order zero lag low pass butterworth filter at 10 Hz.
motorVelocity = myButterFilter(time, motorVelocity, 10, 4);
motorAcceleration = myButterFilter(time, motorAcceleration, 10, 4);

% delete this ASAP
xCable = motorAcceleration;

% Compute motor torque
motorTorque = Im*motorAcceleration + (rm*cableForce);

end
```

```
function [rad] = stiffnessModelCobra(torque)
% stiffnessModelCobra determine orthosis rotation due to soft tissue
compression
%   This function uses our experimentally determined relationship between
%   applied torque and orthosis rotation to soft tissue compression.
%   Input a torque vector where positive is knee flexion, and get out a
%   rotation in radians that also has positive flexion.

% Preallocate
rad = zeros(1, length(torque));

% Apply separate polynomials to flexion and extension. (This should be
% fixed later. I should have fit a 3rd order instead of two 2nd order
% polynomials.)
rad(torque>=0) =  -2.564e-05*torque(torque>=0).^2 +
0.006227*torque(torque>=0) - 3.945e-18;
rad(torque<0) = 4.273e-05*torque(torque<0).^2 + 0.007858*torque(torque<0) -
1.97e-17;
end
```

```
function [ firstDerivative ] = finiteDifferenceApprox( time, func )
% finiteDifferenceApprox: Compute a derivative
%   Pass in a time vector and signal to compute the derivative of.

n = length(time);
firstDerivative = zeros(size(time));

%% Calculate First Derivative
% Use a forward difference scheme for the first two data points.
firstDerivative(1) = (-func(3) + 4*func(2) - 3*func(1))/(time(3)-time(1));
firstDerivative(2) = (-func(4) + 4*func(3) - 3*func(2))/(time(4)-time(2));

% Use a central difference scheme for the middle data points.
for i = 3:n-2
    dt = time(i+1)-time(i);
    firstDerivative(i) = (-func(i+2) + 8*func(i+1) - 8*func(i-1) + func(i-
2))/(12*dt);
end

%Use a backward difference scheme for the last two data point.
firstDerivative(n-1) = (3*func(n-1) - 4*func(n-2) + func(n-3))/(2*dt);
firstDerivative(n) = (3*func(n) - 4*func(n-1) + func(n-2))/(2*dt);

end
```

```
function [ filteredSignal ] = myButterFilter(time, noisySignal,
cutOffFrequency, filterOrder)
%UNTITLED2 Low pass filters a signal with a butterworth filter
%   Pass in a time vector, a noisy signal, a cutoff frequency, and the
%   order of the butterworth filter. 4th order is what I typically use, but
%   the filtfilt() command effectively makes it an 8th order filter, as it
%   rus the signal through forward and backwards.


% Determine sampling frequency in Hz
sf = 1/mean(diff(time));

% Set normalized cutoff frequency to cutoff frequency
Wn = cutOffFrequency/(sf/2);

% User butter function to determine filter coefficients
[B,A] = butter(filterOrder,Wn);

filteredSignal = filtfilt(B,A,noisySignal);

end
```

APPENDIX B

This appendix contains the wiring schematic for the electrical panel, all manufacturing drawings for the custom metal componentry, and the specification sheets for the wearable sensors.

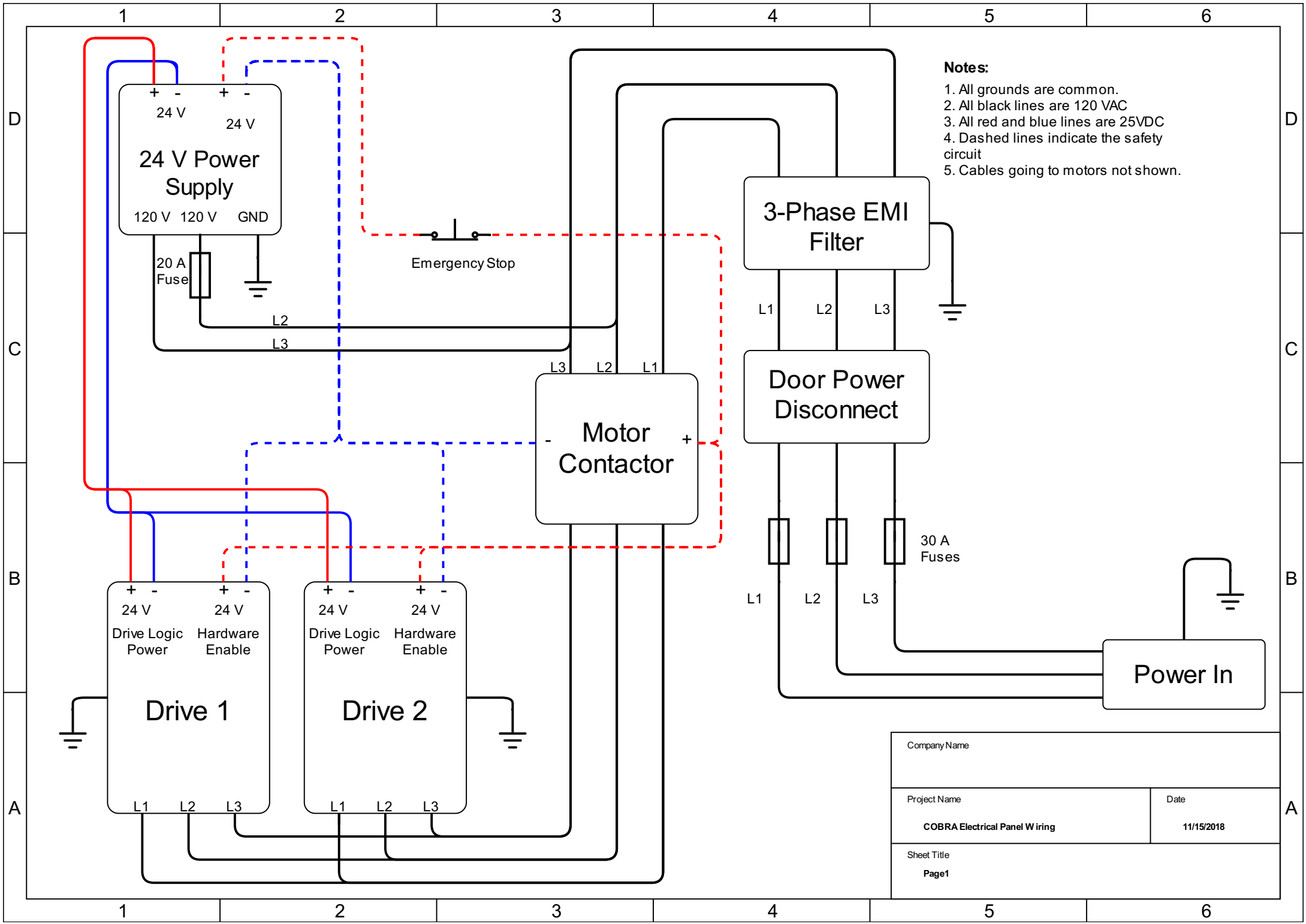
24 V Power Supply
24 V
24 V
120 V 120 V GND
20 A Fuse
Emergency Stop
L2
L3
L3 L2 L1
Motor Contactor
3-Phase EMI Filter
L1 L2 L3
Door Power Disconnect
30 A Fuses
L1 L2 L3
Power In
Drive 1
24 V Drive Logic Power
24 V Hardware Enable
L1 L2 L3
Drive 2
24 V Drive Logic Power
24 V Hardware Enable
L1 L2 L3
Notes:
1. All grounds are common.
2. All black lines are 120 VAC
3. All red and blue lines are 25VDC
4. Dashed lines indicate the safety circuit
5. Cables going to motors not shown.
Company Name
Project Name
COBRA Electrical Panel Wiring
Date
11/15/2018
Sheet Title
Page1

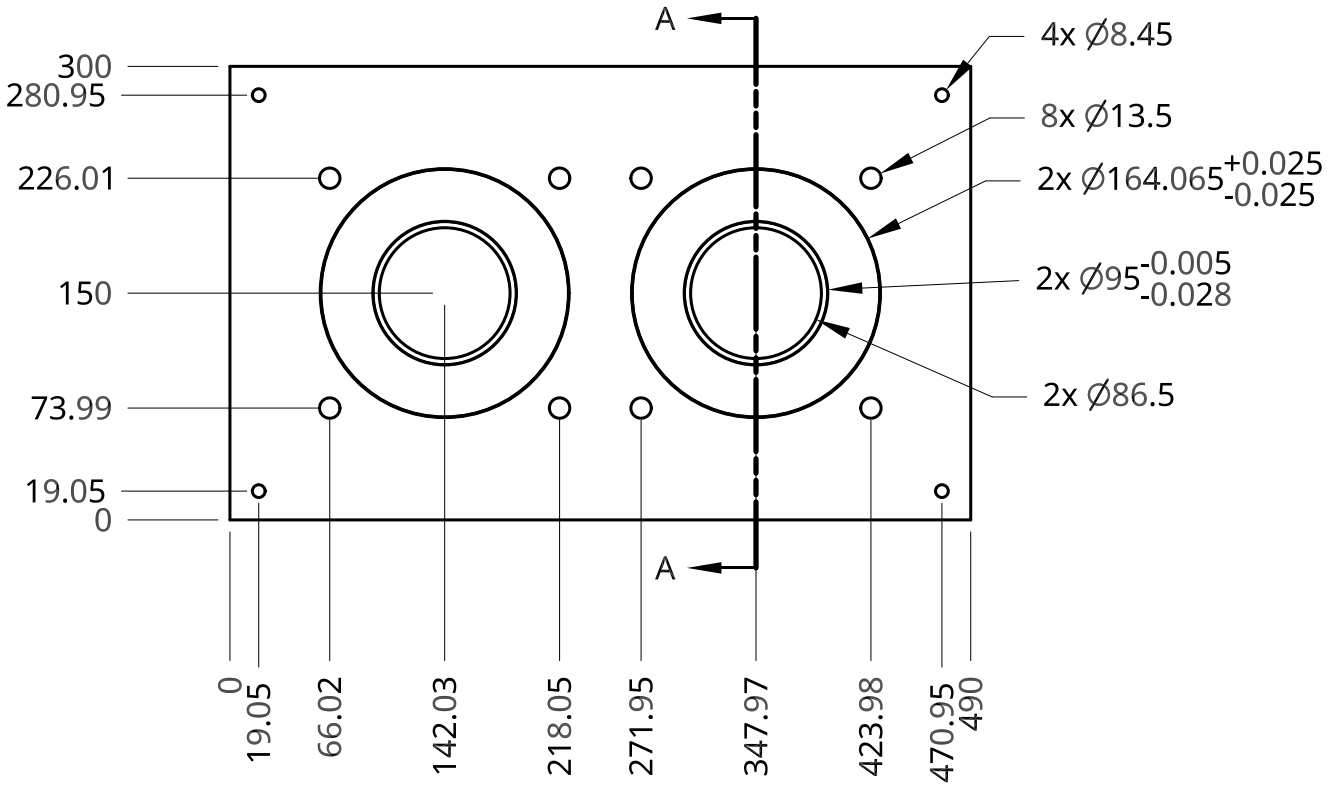

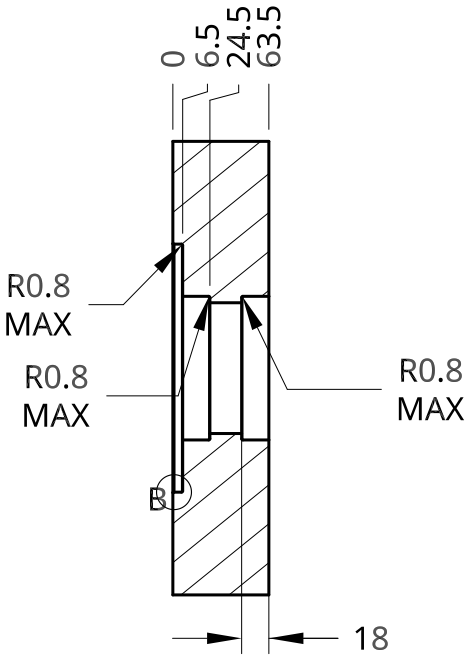

SECTION A - A

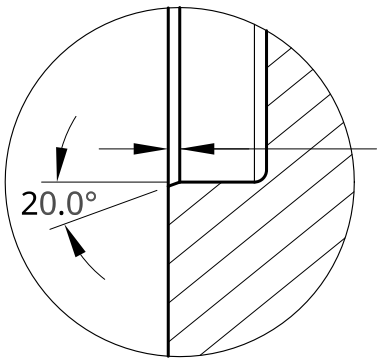

DETAIL B
SCALE 2:1

UNLESS OTHERWISE SPECIFIED, DIMENSIONS ARE IN MILLIMETERS		NAME	DATE
Tolerances ± 0.254 mm unless specified otherwise	DRAWN	Anthony Anderson	07/13/2017
SURFACE FINISH √	CHECKED		
	APPROVED		
DO NOT SCALE DRAWING			
BREAK ALL SHARP EDGES AND REMOVE BURRS			
THIRD ANGLE PROJECTION	MATERIAL	FINISH	
	AL 6061-T6		

TITLE	Motor Mount Plate	
SIZE A	DWG NO. COBRA001	REV. 2
SCALE 1:5	WEIGHT	SHEET 1 of 1

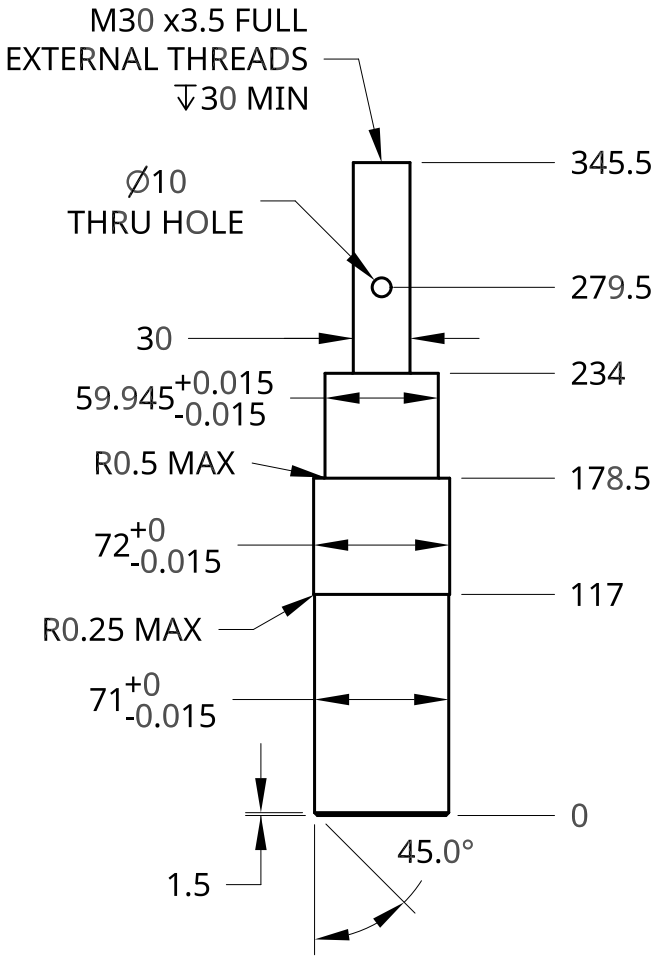

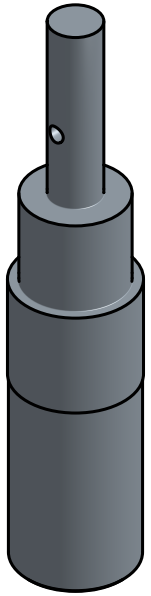

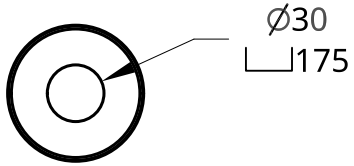

UNLESS OTHERWISE SPECIFIED, DIMENSIONS ARE IN MILLIMETERS		NAME	DATE
TOLERANCES ± 0.254 UNLESS OTHERWISE SPECIFIED	DRAWN	Anthony Anderson	07/24/2017
SURFACE FINISH	CHECKED		
	APPROVED		
DO NOT SCALE DRAWING			
BREAK ALL SHARP EDGES AND REMOVE BURRS			
THIRD ANGLE PROJECTION	MATERIAL	FINISH	
	AL6061-T6		

TITLE	Drive Shaft	
SIZE A	DWG NO. COBRA002	REV. -
SCALE 1:4	WEIGHT	SHEET 1 of 1

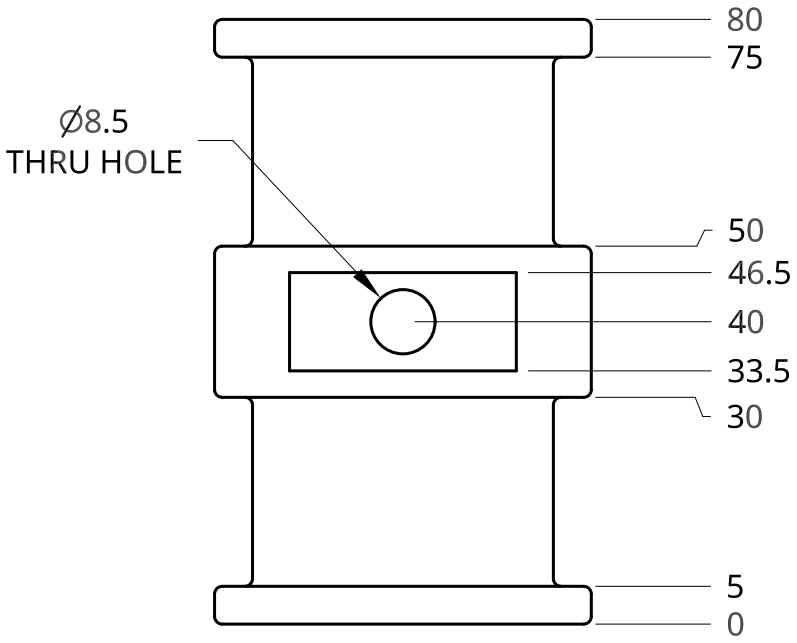

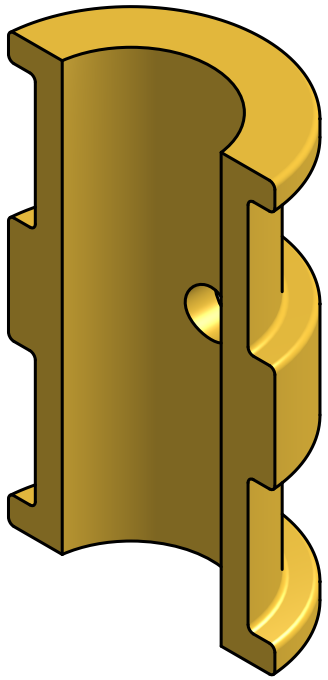

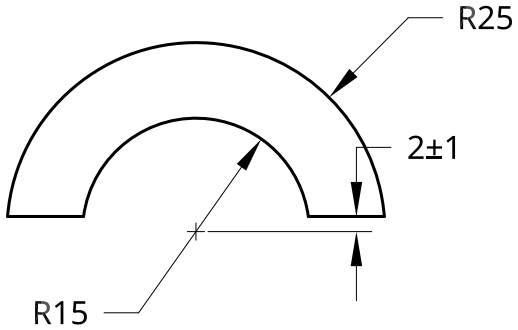

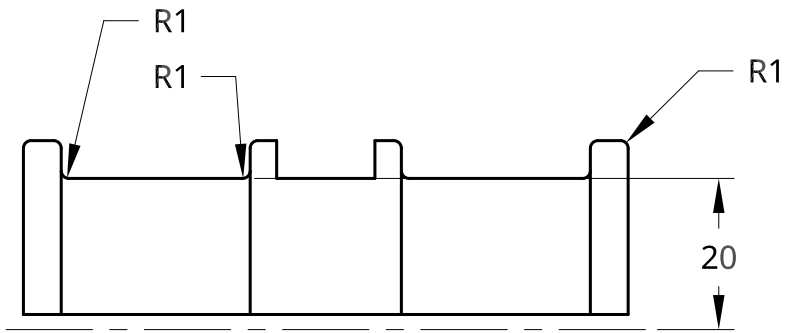

UNLESS OTHERWISE SPECIFIED, DIMENSIONS ARE IN MILLIMETERS		NAME	DATE
TOLERANCS ± 0.254	DRAWN	Anthony Anderson	07/25/2017
SURFACE FINISH	CHECKED		
	APPROVED		
DO NOT SCALE DRAWING			
BREAK ALL SHARP EDGES AND REMOVE BURRS			
THIRD ANGLE PROJECTION	MATERIAL	AL6061-T6	FINISH

TITLE: ANKLE SHAFT CLAMP

SIZE	DWG NO.	REV.
A	COBRA003	2

SCALE	WEIGHT	SHEET
1:1		1 of 1

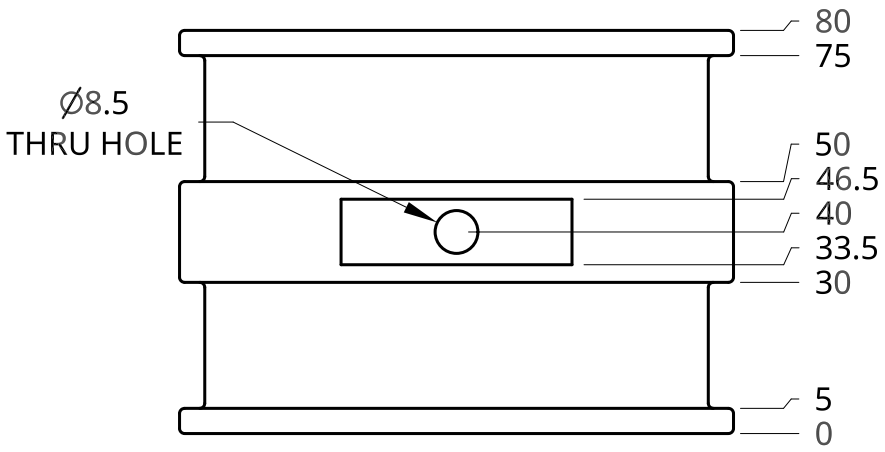

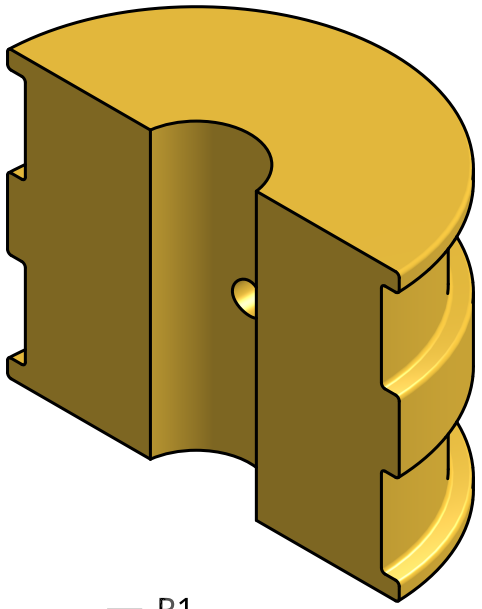

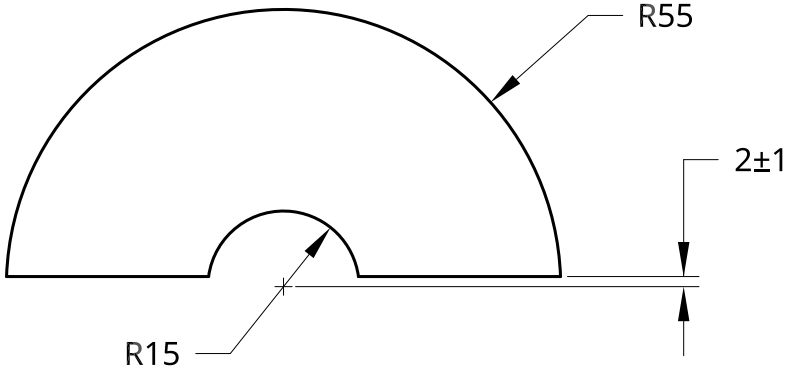

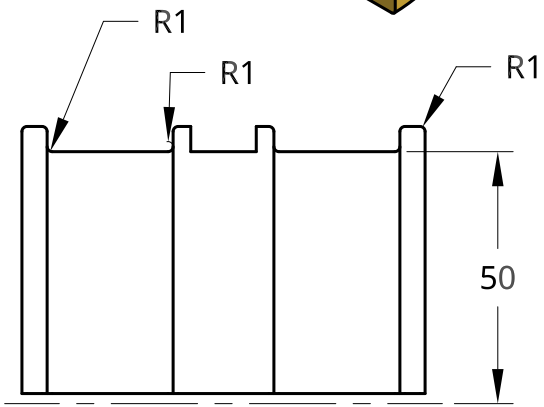

UNLESS OTHERWISE SPECIFIED, DIMENSIONS ARE IN MILLIMETERS		NAME	DATE
TOLERANCES ± 0.254	DRAWN	Anthony Anderson	07/25/2017
SURFACE FINISH	CHECKED		
	APPROVED		
DO NOT SCALE DRAWING			
BREAK ALL SHARP EDGES AND REMOVE BURRS			
THIRD ANGLE PROJECTION	MATERIAL	FINISH	
	AL6061-T6		

TITLE	KNEE SHAFT CLAMP	
SIZE A	DWG NO. COBRA004	REV. 2
SCALE 0.6667:1	WEIGHT	SHEET 1 of 1

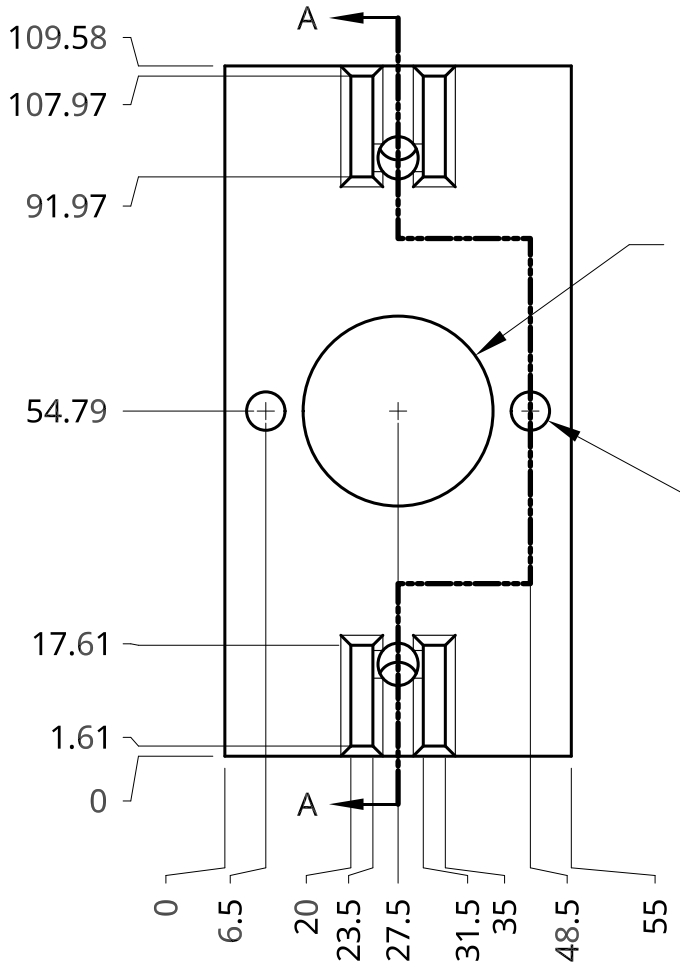

BOTTOM VIEW

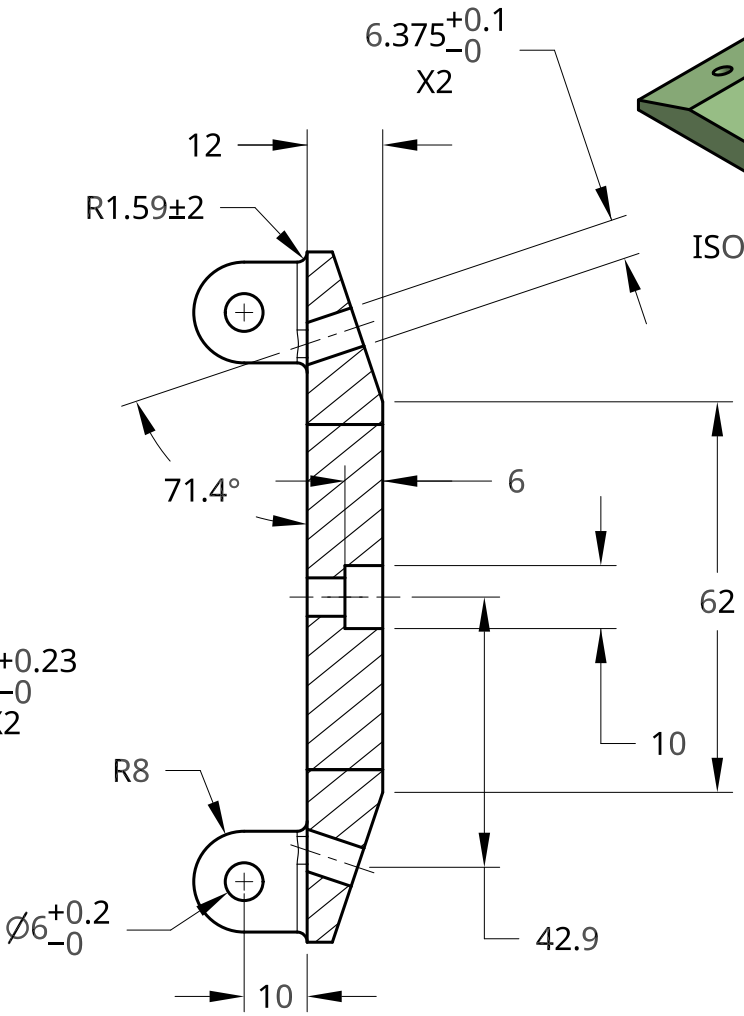

SECTION A - A

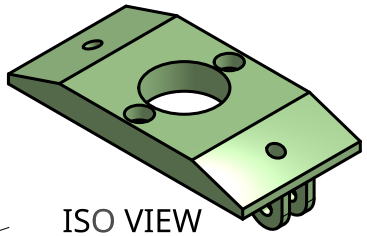

ISO VIEW
SCALE 2:5

UNLESS OTHERWISE SPECIFIED, DIMENSIONS ARE IN MILLIMETERS		NAME	DATE
TOLERANCES ±0.1 UNLESS SPECIFIED	DRAWN	ANTHONY ANDERSON	08/16/2018
	CHECKED	CHRIS RICHBURG	8/16/18
	APPROVED	--	--
DO NOT SCALE DRAWING			
BREAK ALL SHARP EDGES AND REMOVE BURRS			
THIRD ANGLE PROJECTION	MATERIAL	ALUMINUM 6061	FINISH STANDARD

TITLE

PROSTHETIC FOOT
BOWDEN CABLE GROUND PLATE

SIZE	DWG NO.	REV.
A	COBRA005	0
SCALE 5:6	WEIGHT	SHEET 1 of 1

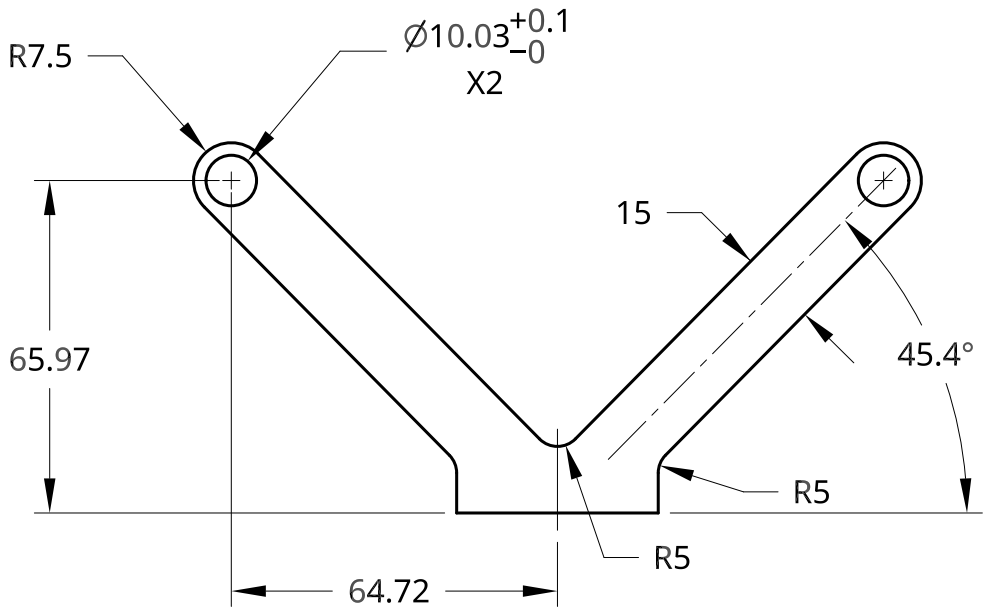

FRONT VIEW

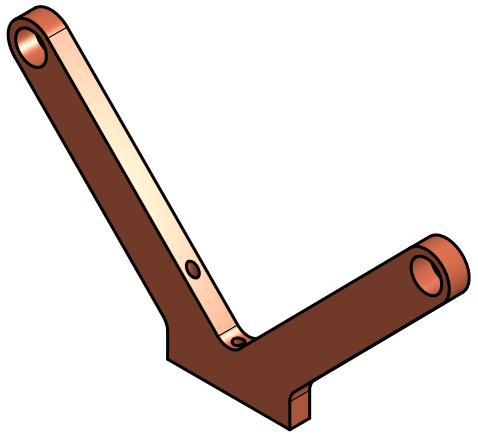

SCALE 4:7

ISO VIEW

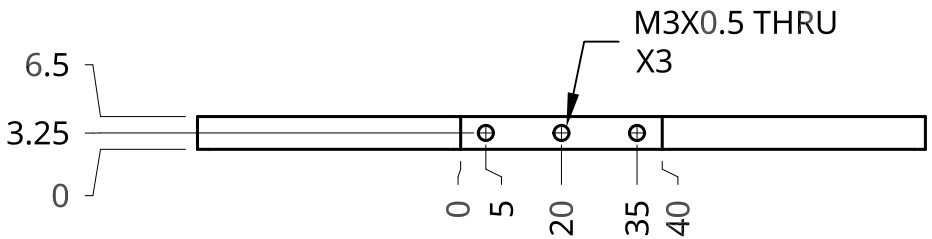

BOTTOM VIEW

UNLESS OTHERWISE SPECIFIED, DIMENSIONS ARE IN MILLIMETERS		NAME	DATE
TOLERANCES ±0.1 UNLESS SPECIFIED	DRAWN	ANTHONY ANDERSON	08/16/2018
	CHECKED	CHRIS RICHBURG	8/16/2018
	APPROVED	--	--
DO NOT SCALE DRAWING			
BREAK ALL SHARP EDGES AND REMOVE BURRS			
THIRD ANGLE PROJECTION	MATERIAL	ALUMINUM 6061	FINISH STANDARD

TITLE: PROSTHETIC FOOT LEVER ARMS

SIZE	DWG NO.	REV.
A	COBRA006	0
SCALE 2:3	WEIGHT	SHEET 1 of 1

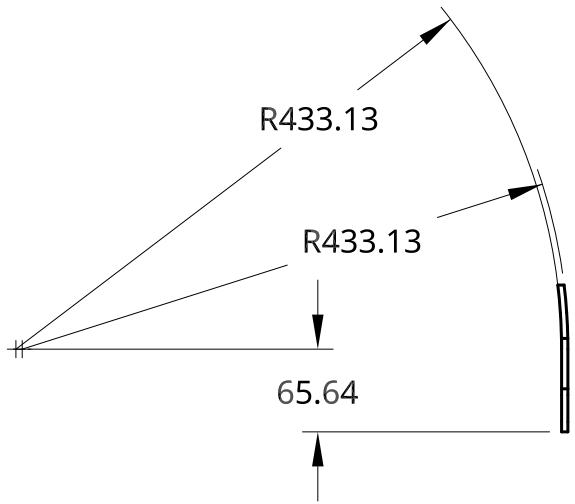

SIDE VIEW
SCALE 1:6

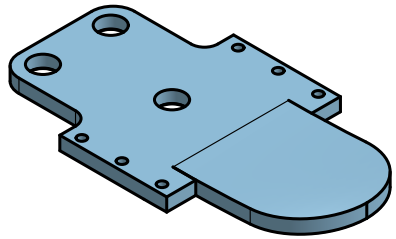

ISO VIEW

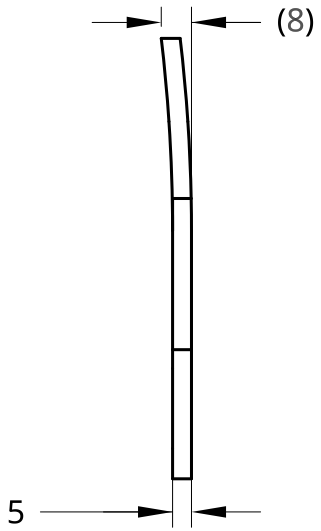

SIDE VIEW

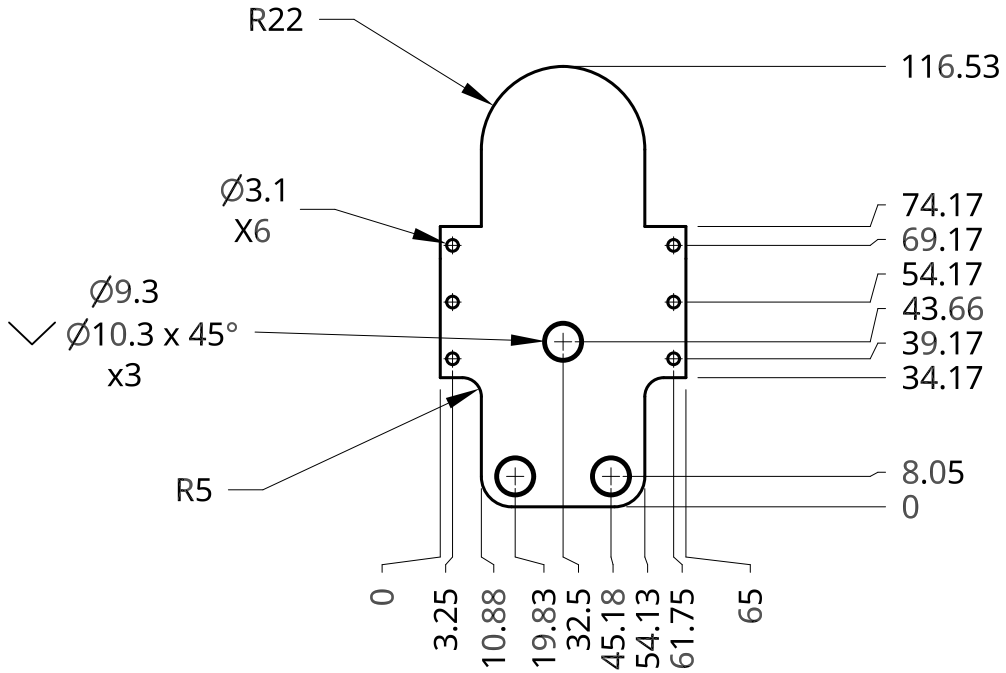

BOTTOM VIEW

UNLESS OTHERWISE SPECIFIED, DIMENSIONS ARE IN MILLIMETERS		NAME	DATE
TOLERANCES ±0.1 UNLESS SPECIFIED	DRAWN	ANTHONY ANDERSON	08/16/2018
	CHECKED	CHRIS RICHBURG	08/16/2018
	APPROVED		
DO NOT SCALE DRAWING			
BREAK ALL SHARP EDGES AND REMOVE BURRS			
THIRD ANGLE PROJECTION	MATERIAL	FINISH	
	ALUMINUM 6061	STANDARD	

TITLE

PROSTHETIC FOOT ATTACHMENT PLATE

SIZE	DWG NO.	REV.
A	COBRA007	0
SCALE 1:2	WEIGHT	SHEET 1 of 1

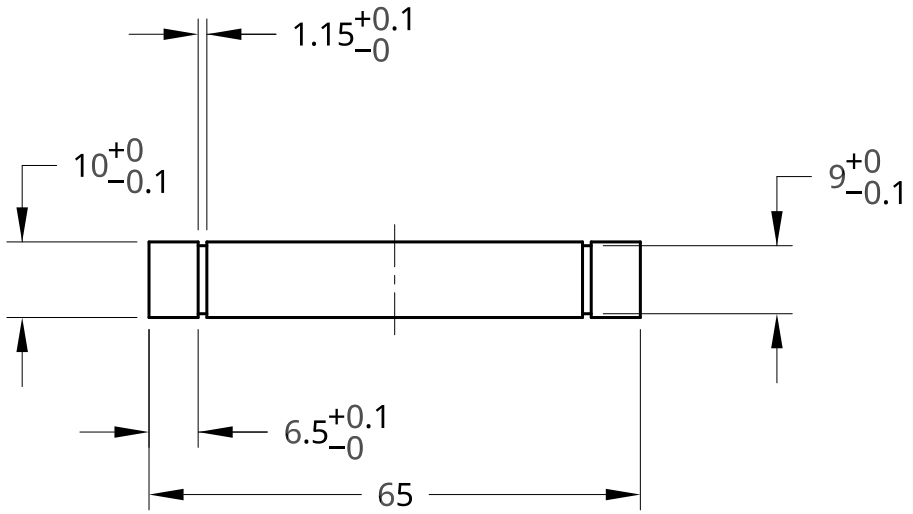

SIDE VIEW

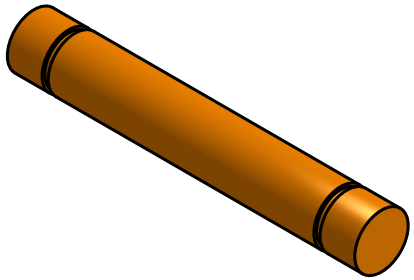

ISO VIEW

UNLESS OTHERWISE SPECIFIED, DIMENSIONS ARE IN MILLIMETERS		NAME	DATE
	DRAWN	ANTHONY ANDERSON	08/17/2018
TOLERANCES ±0.1 UNLESS SPECIFIED	CHECKED		
	APPROVED		
DO NOT SCALE DRAWING			
BREAK ALL SHARP EDGES AND REMOVE BURRS			
THIRD ANGLE PROJECTION	MATERIAL: LOW CARBON STEEL	FINISH: STANDARD	

TITLE: PROSTHETIC FOOT DRIVE SHAFT		
SIZE: A	DWG NO.: COBRA008	REV.: 0
SCALE: 1:1	WEIGHT:	SHEET: 1 of 1

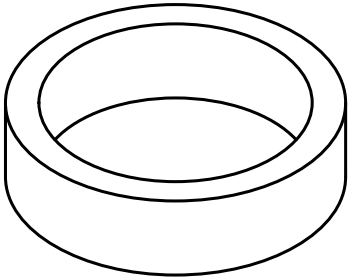

ISO VIEW

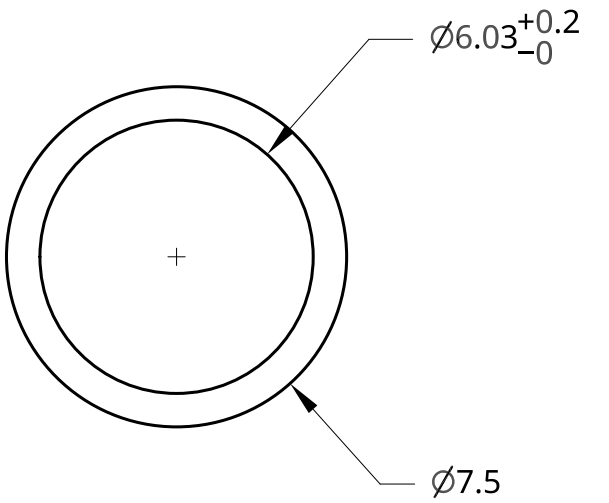

TOP VIEW

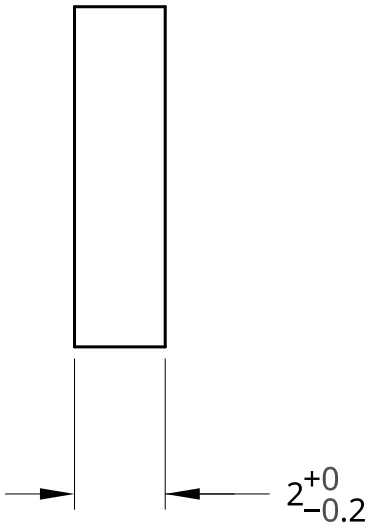

FRONT VIEW

UNLESS OTHERWISE SPECIFIED, DIMENSIONS ARE IN MILLIMETERS		NAME	DATE
	DRAWN	ANTHONY ANDERSON	08/17/2018
TOLERANCES ±0.1 UNLESS SPECIFIED	CHECKED		
	APPROVED	--	--
BREAK ALL SHARP EDGES AND REMOVE BURRS			
THIRD ANGLE PROJECTION	MATERIAL	ALUMINUM 6061	FINISH STANDARD

TITLE: BEARING SPACER

SIZE	DWG NO.	REV.
A	COBRA009	0

SCALE	WEIGHT	SHEET
6:1		1 of 1

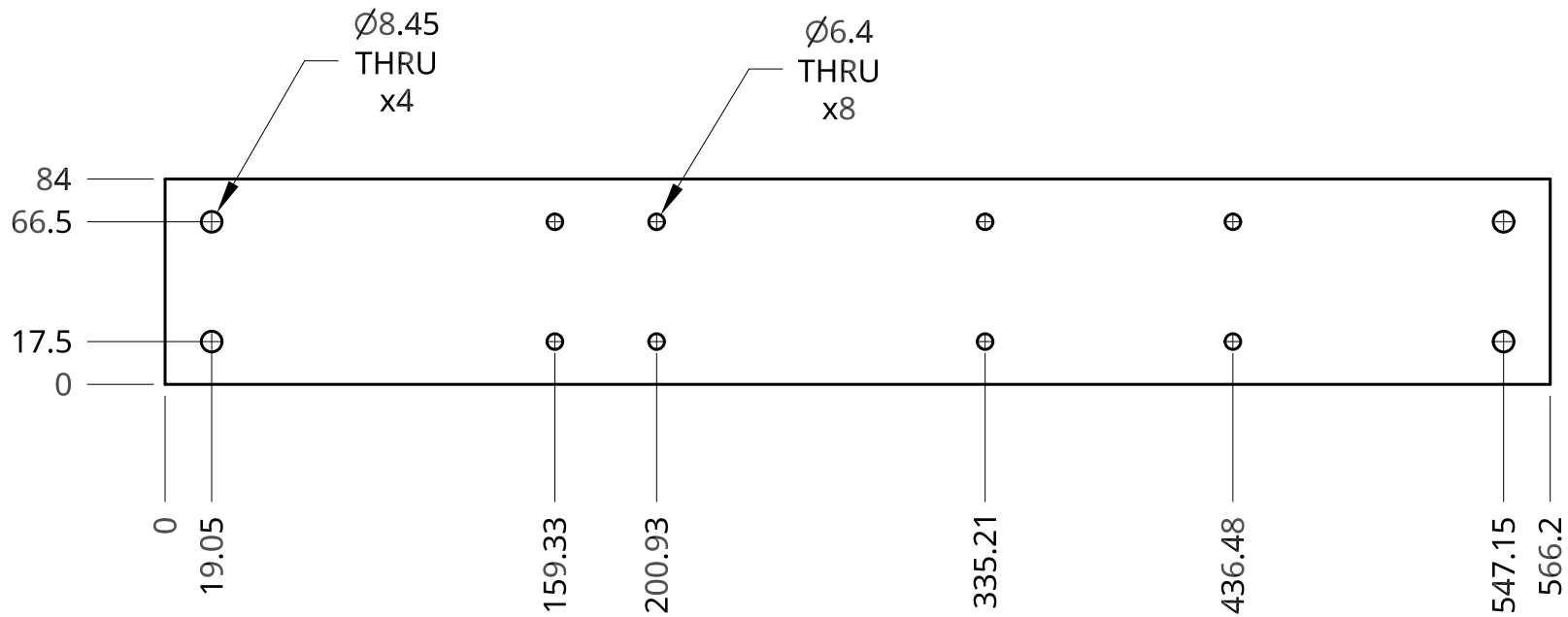

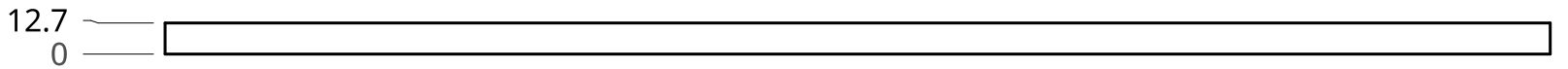

UNLESS OTHERWISE SPECIFIED, DIMENSIONS ARE IN MILLIMETERS		NAME	DATE
	DRAWN	ANTHONY ANDERSON	08/17/2018
	CHECKED		
	APPROVED		
DO NOT SCALE DRAWING			
BREAK ALL SHARP EDGES AND REMOVE BURRS			
THIRD ANGLE PROJECTION	MATERIAL	ALUMINUM	FINISH STANDARD

TITLE: BOWDEN GROUNDING PLATE

SIZE	DWG NO.	REV.
A	COBRA010	0

SCALE	WEIGHT	SHEET
1:3		1 of 1

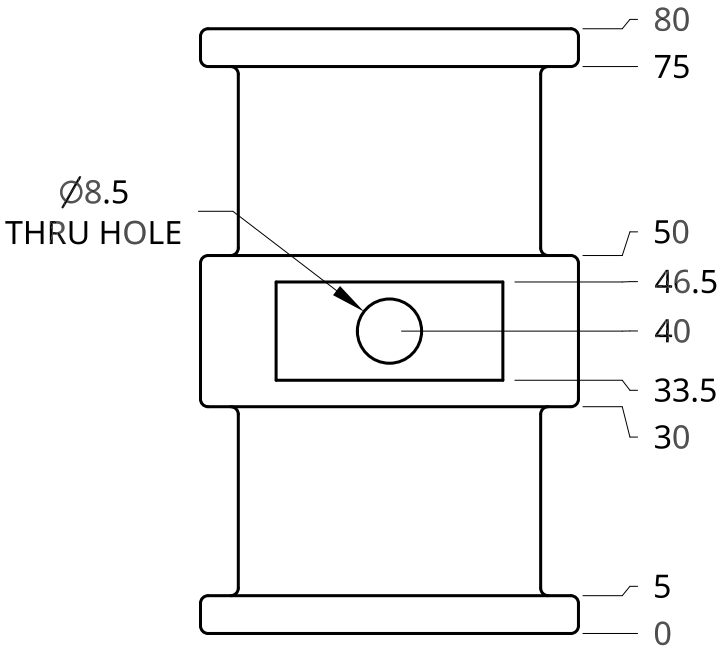

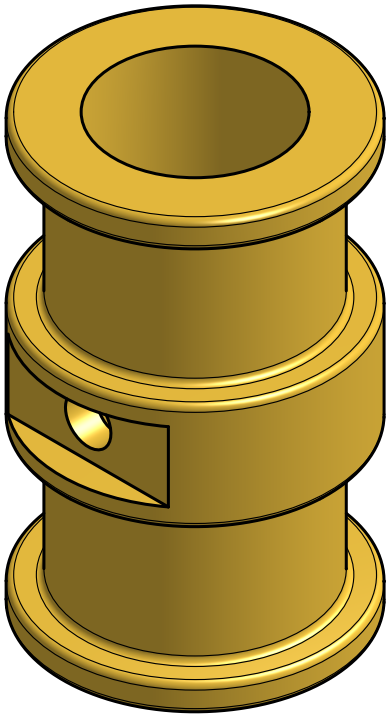

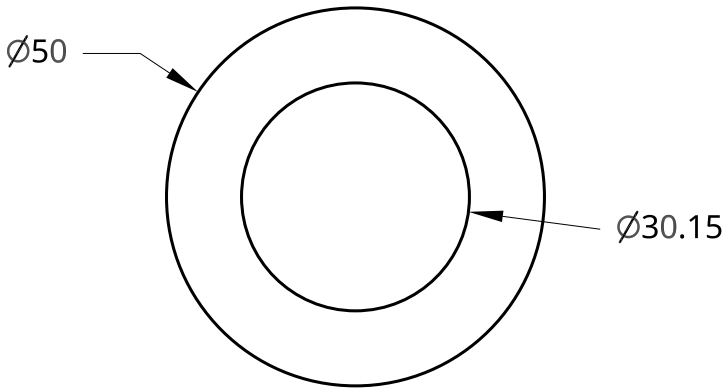

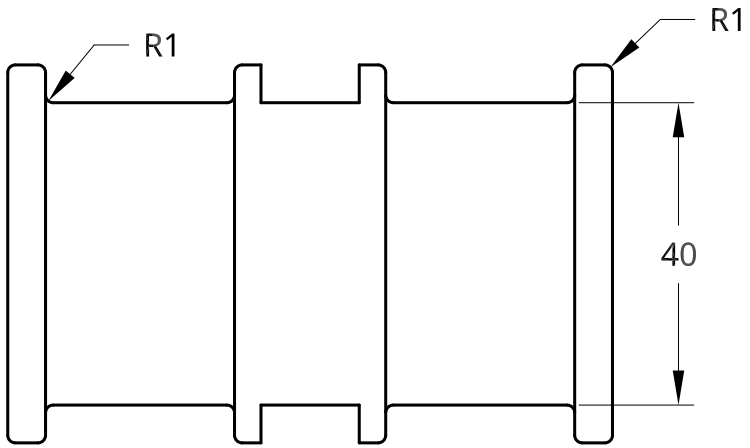

UNLESS OTHERWISE SPECIFIED, DIMENSIONS ARE IN MILLIMETERS		NAME	DATE
TOLERANCES ±0.1	DRAWN	ANTHONY ANDERSON	07/19/2018
	CHECKED		
	APPROVED		
DO NOT SCALE DRAWING			
BREAK ALL SHARP EDGES AND REMOVE BURRS			
THIRD ANGLE PROJECTION	MATERIAL	ALUMINUM	FINISH STANDARD

TITLE: ANKLE PULLEY

SIZE	DWG NO.	REV.
A	COBRA011	-

SCALE	WEIGHT	SHEET
1:1		1 of 1

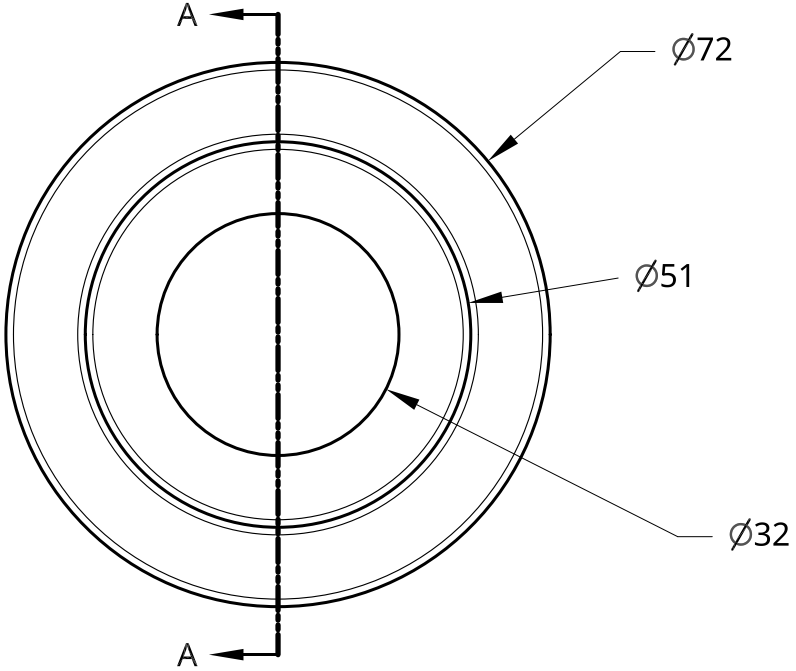

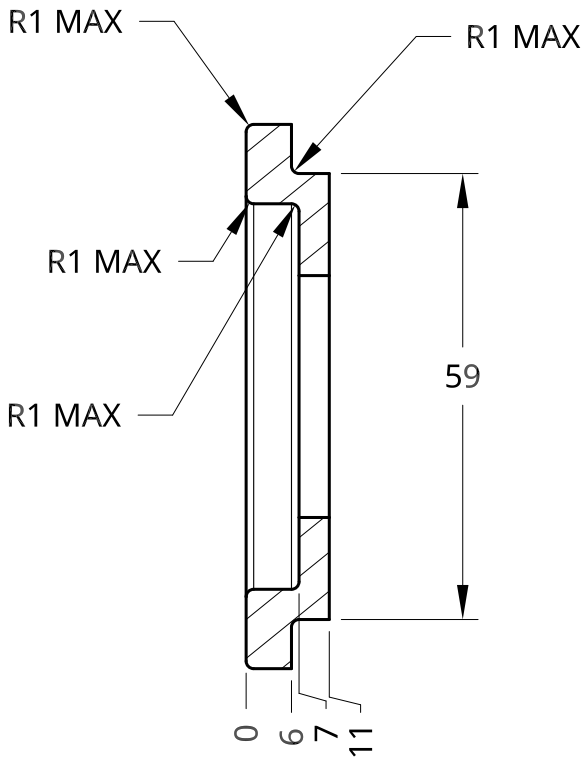

SECTION A - A
SCALE 1:1

UNLESS OTHERWISE SPECIFIED, DIMENSIONS ARE IN MILLIMETERS		NAME	DATE
TOLERANCES = ± 0.1	DRAWN	Anthony Anderson	06/14/2018
SURFACE FINISH	CHECKED		
	APPROVED		
DO NOT SCALE DRAWING			
BREAK ALL SHARP EDGES AND REMOVE BURRS			
THIRD ANGLE PROJECTION	MATERIAL	FINISH	
	Low Carbon Steel	Standard	

TITLE: COBRA SPACER 1

SIZE	DWG NO.	REV.
A	001	0

SCALE	WEIGHT	SHEET
1:1		1 of 1

FUTEK
ADVANCED SENSOR TECHNOLOGY, INC.

MODEL LTH300
Donut/Thru Hole Load Cell

FEATURES

- Fast response time
- Robust strain relief
- Compatible in load washer applications
- Offered in a variety of capacities and inner diameters

Non-loading surface, do not contact

Active End

Fixed End

+ Output (compression)

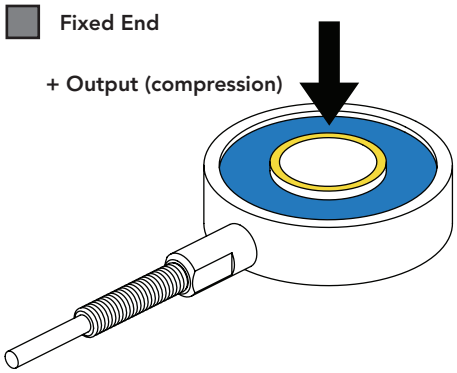

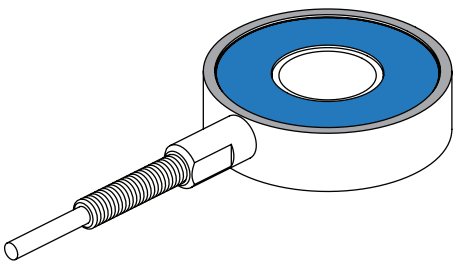

SPECIFICATIONS	
PERFORMANCE	
Nonlinearity	±0.5% of RO
Hysteresis	±0.5% of RO
Nonrepeatability	±0.5% of RO
ELECTRICAL	
Rated Output (RO)	2 mV/V nom
Excitation (VDC or VAC)	18 max
Bridge Resistance	700 Ohm nom
Insulation Resistance	≥500 MOhm @ 50 VDC
Connection	#29 AWG, 4 conductor, spiral shielded Teflon cable, 10 ft [3 m] long
Wiring/Connector Code	WC1
MECHANICAL	
Capacities	50 lb [222 N], 100 lb* [445 N]*, 250 lb [1112 N], 500 lb* [2224 N]*, 1000 lb* [4448 N]*
Weight (approximate)	2 oz [57 g]
Safe Overload	150% of RO
Deflection	0.001 in [0.025 mm] nom
Material	17-4 PH stainless-steel
IP Rating	IP64
TEMPERATURE	
Operating Temperature	-60 to 200°F (-50 to 93°C)
Compensated Temperature	60 to 160°F (15 to 72°C)
Temperature Shift Zero	±0.005% of RO/°F (0.01% of RO/°C)
Temperature Shift Span	±0.005% of Load/°F (0.01% of Load/°C)
CALIBRATION	
Calibration Test Excitation	10 VDC
Calibration (standard)	5-pt Compression
Shunt Calibration Value	100 kOhm
CONFORMITY	
RoHS	2011/65/EU
CE	EN55011:2009; EN61326-1:2006

*Commonly stocked capacities

DIMENSIONS inches [mm]

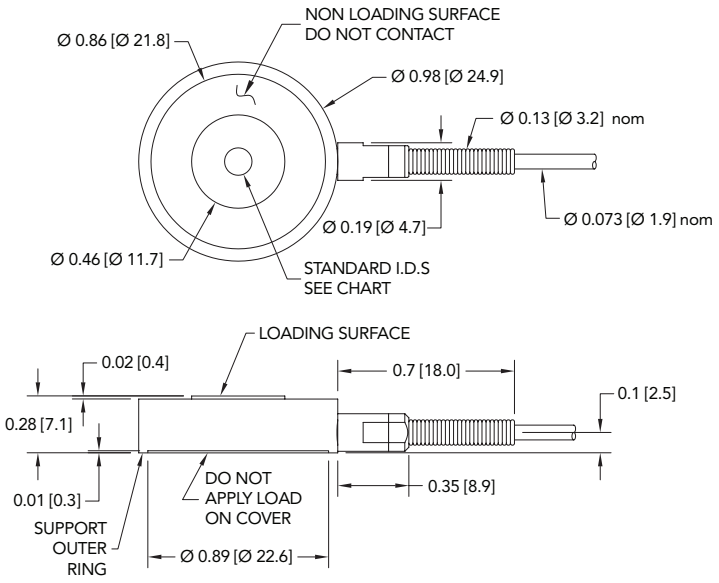

INNER DIAMETER

ID	Dimension $^{+0.01}_{-0.00}$ [$^{+0.25}_{-0.00}$]
3/16	0.197 [5.01]
1/4*	0.259 [6.58]
5/16	0.322 [8.18]
3/8*	0.384 [9.75]

*Commonly stocked capacities and inner diameters

WIRING CODE (WC1 WITH SHIELD)

RED	+ EXCITATION
BLACK	– EXCITATION
GREEN	+ SIGNAL
WHITE	– SIGNAL
SHIELD	FLOATING

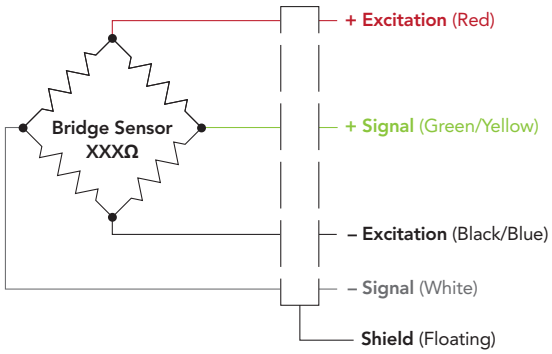

Note: While torquing bolts, high tension forces will occur during installation, which could result in overloading the sensor. FUTEK recommends connecting the sensor to a system in order to monitor the applied forces. FUTEK is not liable or responsible for the mishandling of the sensor during installation.

Drawing Number: FI1425-A

10 Thomas, Irvine, CA 92618 USA
Tel: (949) 465-0900
Fax: (949) 465-0905

www.futek.com

CE RoHS ANSI Z540-1 ISO 17025 ISO 9001 ISO 13485 U.S. Manufacturer

Data sheet
RM08D01_11
Issue 11, 16th February 2017

RM08 super small non-contact rotary encoder

The RM08 is a compact, sealed, super small, high speed rotary magnetic encoder designed for use in space limited applications. The non-contact two part design removes the need for seals or bearings ensuring long-term reliability and simple installation.

The encoder consists of a magnet and a separate sensor board. Rotation of the magnetic actuator is sensed by a custom encoder chip within the body, and processed to give analogue, incremental, SSI or linear voltage outputs.

The encoder chip processes the signals received to provide resolutions up to 12 bit (4,096 counts per revolution) with high operational speeds.

The compact encoder body is just 8 mm in diameter and provides degree of protection to IP68.

The RM08 encoder has been designed for direct integration into high volume OEM applications and can be used in a wide range of applications including motor control and industrial automation.

The RM08 encoders use the sensor AM4096, for details refer to AM4096 data sheet.

Product range

RM08A
Analogue sine/cosine, one period/ revolution.

RM08I
Incremental with 8 to 1,024 pulses per revolution (32 to 4,096 counts per revolution).

RM08S
Synchro serial with 5 to 12 bit resolution (32 to 4,096 positions per revolution).

RM08V
Linear voltage with ramp from 0 V to 5 V.

- **Super small size – 8 mm diameter body**
- **Non-contact, frictionless design**
- **3.3 V or 5 V power supply versions**
- **High speed operation up to 30,000 rpm**
- **Industry standard analogue sinusoidal, incremental, SSI and linear voltage output formats**
- **Accuracy up to ±0.3°**
- **RoHS compliant (lead free) - see Declaration of conformity**

RM08 dimensions

Dimensions and tolerance in mm.

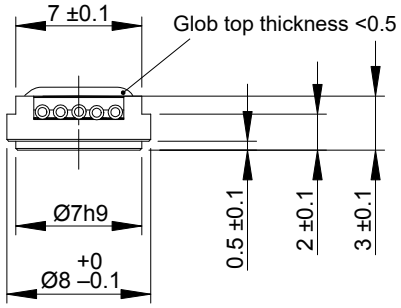

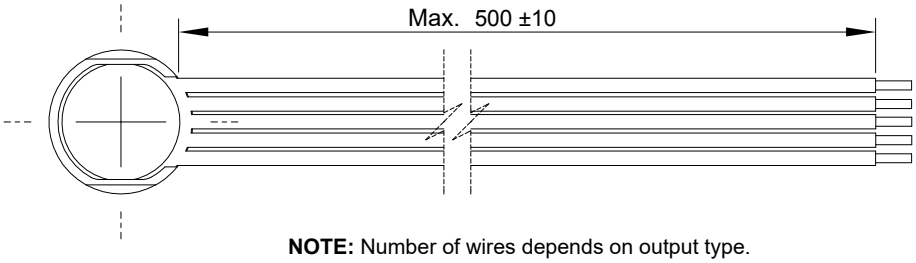

NOTE: Number of wires depends on output type.

Mounting instructions

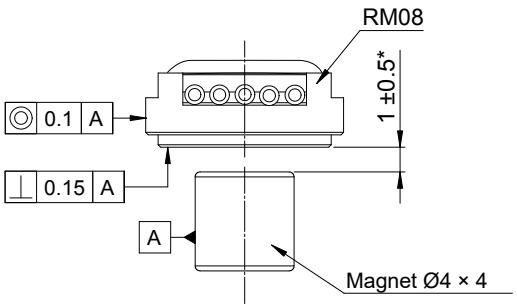

* 0.5 ±0.2 mm for Ø3 × 1 mm magnet
(more info: see part numbering on page 8).

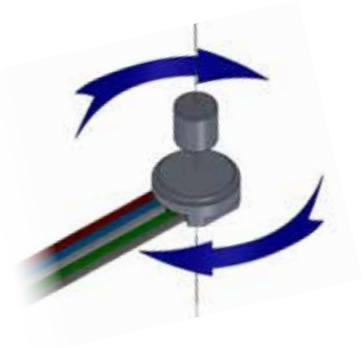

Clockwise rotation of magnet.

RM08 technical specifications

Mechanical data	
Encoder housing material	Aluminium
Encoder mass	< 2 g (with 200 mm long wires)
Wire thickness	AWG30
Magnet material	SmCo (Sm_2Co_{17}), NiCuNi coated
Magnet mass	0.4 g
Shock	Half-sine 100 g, according to IEC 60068-2-27, Ed. 4
Steady-state acceleration	700 g, according to IEC 60068-2-27, Ed. 2
Environmental data	
Operating and storage temperature	–40 °C to +85 °C

RM08A - Analogue sinusoidal

Two sinusoidal output signals (90° phase shifted, single ended)

Power supply	V_{dd} = 5 V or 3.3 V ± 5 %
Power consumption	Typ. 26 mA
Sinusoidal outputs	
Signal amplitude (A)	0.8 ± 0.2 V
Signal offset (Agnd)	1.55 ± 5 mV
Phase difference	90° ± 0.2°
Max. speed	30,000 rpm
Temperature	–40 °C to +85 °C

* Valid for Ø4 × 4 mm magnets only.

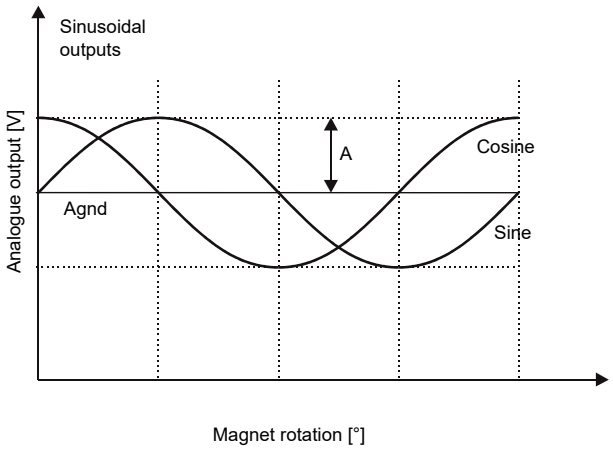

Fig. 1: Timing diagram for clockwise rotation of magnet

Connections

Signal	Colour
V_{dd}	Red
GND	Blue
Sin	White
Cos	Grey